Plasma enhanced pulsed laser deposition

Sudha Rajendiran

Doctor of Philosophy

University of York

Physics

November 2017

I would like to dedicate this thesis to my Mum and Dad

Abstract

This thesis introduces a novel deposition technique, Plasma-Enhanced Pulsed Laser Deposition (PE-PLD) that attempts to overcome limitations in traditional PLD by combining it with a background oxygen RF plasma instead of a neutral gas. Advantages of this novel technique for the deposition of metal-oxide films include, the use of simple, pure metal targets instead of metal-oxide composite targets and the lack of the necessity for substrate heating and post-annealing to obtain high-quality films. The feasibility of this method was studied both numerically and experimentally. Numerical simulations of the laser ablation process and an Inductively Coupled Plasma (ICP), i.e. the oxygen RF plasma, using different 2D hydrodynamic codes, found that the densities of the Cu plume and ICP were similar in front of the substrate, allowing the necessary interaction between them to oxidise the Cu and deposit a CuO film.

Time-resolved optical emission spectroscopy provided electron temperatures and densities that were used to benchmark the modelling results as well as provide some insight into the process of slowing down of the plume due to the background gas. Also, the assumption of Local Thermodynamic Equilibrium (LTE), commonly used in these diagnostic techniques, was investigated and found to not be strictly fulfilled for most of the ablation process, meaning that further investigations are needed to confirm the validity of these diagnostics.

Finally, copper oxide thin films were deposited using PE-PLD. Analysis of the composition showed that high-quality films could be formed and that at a low oxygen pressure stoichiometric, polycrystalline CuO was formed, while at a higher pressure stoichiometric, polycrystalline Cu_2O was deposited.

Contents

List of Tables

List of Figures

Acknowledgments

Firstly, I would like to express my heartfelt thanks to my supervisor Dr Erik Wagenaars for being very supportive, patient and continuously encouraging me to learn science by sharing his valuable knowledge. I would definitely say, without you, whom I'm now might be a daydream. Thank you so much for giving me such an opportunity to study at university of york.

My sincere thanks to Prof Timo Gans, Dr Deborah O'Connell and Dr James Dedrick for their support in my research. I would also like to thank Dr Kari Niemi and Richard Armitage for their support during my lab days.

Besides of all, A special thanks to Martin Blake and David Meehan for being very supportive and helpful in submitting my thesis. Dr Jüri Raud you are always special to me, Even you are near or far, you helped me so much and thanks for everything you did for me. Sarah Wilson, you, your muffins and your support was one of the reason for many days to come out of thesis writing stress so quickly. I would also like to thank Jonathan Brodrick, Frederik Riedel, Hannah Willet and David Shaw for being a wonderful office mate. I would also like to thank Andrew Gibson, Sandra Schroter, Layla Alelyani, Arpiwat Wijiakhum and other members of LTP for their advice and support. A special thanks to Andy West for the consistent support all times.

Special thanks to my Mother Parimala and father Rajendiran, without you I'm nothing and I don't want to end your support and love just by saying thanks because you are more

than anything in my life, Love you so much. Special thanks to my sister Shanthi, brother in law Gopal and my friends for their continuous moral support. Finally, I would like to thank Balaji for being there with me in tough times and supporting me throughout this journey and I'll definitely be there for you forever in your life.

Declaration

This thesis has not previously been accepted for any degree and is not being concurrently submitted in candidature for any degree other than Doctor of Philosophy of the University of York. This thesis is the result of my own investigations, except where otherwise stated. All other sources are acknowledged by explicit references.

Chapter 1

Introduction

1.1 Motivation

Plasma and its applications have made our modern life more sophisticated. However, understanding the properties of plasmas will not only help with improving our modern technology, it also connects directly with nature for a better understanding of our solar system and universe. One common way to classify plasmas is into thermal and non-thermal plasmas.

In the case of thermal plasma, electrons, neutrals and ions in the plasma can be described using a single temperature. This is the most common type of plasma that can be found in nature (eg: sun, lightning etc). On the other hand, in the case of non-thermal plasmas, species in the plasmas are not in thermodynamical equilibrium. The electrons in such plasmas are hotter than ions and these hotter electrons can effectively dissociates neutral chemical species. These types of plasma play a major role in industrial applications, e.g. in surface modification of plastics, etching of computer chips, treating biological samples and deposition of thin films. This last application is the focus of this thesis.

In recent years, semiconductor thin films plays a vital role in modern life. They are

essential for the production of micro-electronics and novel energy harvesting and storage devices such as solar cells and super capacitors. For these applications, high-quality thin films are required and researchers have developed various fabrication techniques to produce suitable thin films for various applications like solar cells [2], super capacitors [3], bio-sensors [4] and high-Tc superconductors [5]. A range of deposition techniques like molecular beam epitaxy [6], reactive magnetron sputtering [7], pulsed laser deposition [8], [9], thermal evaporation [10] and e-beam evaporation techniques have been developed in the past and are widely used in research and applications today. However, controlling the stoichiometry and obtaining good quality thin film has been an ongoing challenge.

The work in this is mainly focused on combining a thermal and a non-thermal plasma to deposit a thin film. In particular, we look at adding an Inductively Coupled Plasma (ICP) background plasma to a standard Pulsed Laser Deposition setup, creating our novel technique: Plasma-Enhanced Pulsed Laser Deposition (PE-PLD). This novel method introduces more reactive species during the deposition process. Therefore depending on the properties of the non-thermal ICP plasma in the chamber, the stoichiometry of the thin film can be controlled. Moreover, conventional deposition techniques use elevated substrate temperatures and post-annealing to obtain the required degree of oxidation. In our new technique, there is no substrate heating or post-annealing needed to deposit stoichiometric thin films. In the upcoming chapters, I will discuss the details of this technique as well as the results and discussion of our investigations. In this thesis I investigate the feasibility of the new PE-PLD technique by looking at the deposition of copper oxide thin films.

1.2 Thesis Outline

Chapter 2. Copper oxide thin films: This chapter is focused on a literature view of copper oxide thin films; their applications as well as the available deposition techniques. In particular, the two different crystal structures, CuO and Cu_2O, and their crystal

properties are introduced.

Chapter 3. Pulsed Laser Deposition: This chapter contains the physics behind laser plasma interaction for different materials and discusses the different stages of laser ablation: plasma formation and plasma expansion in vacuum and background gas. Finally, it discusses the different growth modes of thin films and the experimental parameters that influence the deposition process.

Chapter 4. Plasma-Enhanced Pulsed Laser Deposition: This chapter describes the pulsed laser deposition and plasma enhanced pulsed laser deposition techniques in detail. It includes the detailed experimental design used for our PE-PLD technique.

Chapter 5. Thin film characterisation techniques: This chapter describes the experimental designs and concepts of thin film characterisation techniques relevant for the thesis.

Chapter 6. POLLUX and HPEM simulations: This chapter presents a modelling study to investigate the feasibility of our PE-PLD technique. The laser ablation part is modelled using the code POLLUX while the reactive oxygen ICP is described using the code HPEM.

Chapter 7. Time resolved spectroscopy of a laser produced plasma: In this chapter an experimental investigation of the laser ablation plasma plume is presented. Time-resolved optical emission spectroscopy is used to determine electron temperatures and densities in the plasma. Extra attention is given to the assumptions and limitations of the experimental technique, especially deviations from Local Thermodynamic Equilibrium (LTE), a necessary criterion for the diagnostic method, are investigated in detail.

Chapter 8. Proof-of-concept: Thin film deposition using PE-PLD: This chapter presents the first results of thin film deposition using the PE-PLD technique. Films are deposited under different experimental conditions and are characterised using a range of

surface analysis techniques, giving information about stoichiometry, crystal phase, morphology and film thickness.

Chapter 9. Conclusions: This chapter summarises and discusses the main results of this thesis.

Chapter 2

Copper oxide thin films

2.1 Introduction

Thin film technology has contributed to developments in a wide variety of semiconductor device applications, e.g. transparent conducting electrodes for touch screens, ferromagnetic films for computer memory, ceramic films for piezoelectric sensors and nanostructured solar cells. The physical properties of most films are determined by the material characteristics. This allows the development of a range of deposition techniques for the same types of films. Each deposition technique has its own advantages and limitations.

A class of films that is widely studied are metal oxides. For example SnO_2, ZnO and TiO_2 are n-type transparent semiconductors used as Transparent Conductive Oxide (TCO) [11], in gas sensing applications, solar cells and touch screens. ITO (Indium-Tin oxide), with an optical band gap of >3.4eV [12], is the most commonly used Transparent Conductive Electrode. However, since indium is a rare earth metal and that is scarce, alternatives such as doped-ZnO and SnO_2 are being investigated. These materials have similar band gaps as ITO but are far more commonly available. Similarly CuO is a p-type semiconductor with a band gap of 2.1eV and is mostly used for solar cell applications. When

CuO is doped with yttrium and barium it acts as a superconductor [13]. In the section below, I will discuss CuO and Cu_2O crystal structure, properties and applications, as well as the different deposition techniques for these films.

2.2 CuO and Cu_2O thin films?

Copper **(Cu)** is the 29^{th} element in the periodic table and when it is oxidised it exhibits three different forms of oxide: (i) CuO (tenorite) (ii) Cu_2O (cuprite) and (iii) Cu_4O_3 (paramelaconite). Of these three oxide forms, Cu_4O_3 is an unstable form which means it is found less in applications and is studied less in the literature and its physical properties are not very well-known.

Cu_4O_3 was first discovered in late 1870s [14] **[JCPDS card no: 9000603]** and several techniques have been used to deposit Cu_4O_3 thin films. A. Thober et al [15], deposited Cu_4O_3 thin film on quartz thin film using reactive magnetron sputtering in Ar-O_2 mixtures, where the electrical resistivity and optical band gap could be measured at 6.2x$10^8 \mu\Omega$ cm and 2.47 eV. However, from other studies it is clear that a small rise in the temperature changes Cu_4O_3 to CuO quickly [16] [17]. Therefore, the focus in my work will be on the CuO and Cu_2O phases. Table 2.1 shows the different crystallographic properties of these two different form of copper oxides.

Crystallographic parameters	**CuO**	**Cu_2O**
Lattice constant	a=4.6837$\AA$, b=3.4288 $\AA$, c=5.1297$\AA$	a=b=c=4.2520$\AA$
Space Group	C 1 2/c 1(15)	P n -3 m:1(224)
Bond length		
d_{Cu-O}	1.95$\AA$	1.84$\AA$
d_{O-O}	2.62$\AA$	3.68$\AA$
d_{Cu-Cu}	2.90 $\AA$	3.02 $\AA$
Density	6.515 g/cc	5.749 g/cc

Table 2.1: Crystallographic properties of two different form of copper oxides

Even though CuO and Cu_2O are both oxides of Cu, their structure and physical properties are very different. Depending on bond length, lattice constant and space group, the structure of the crystal systems varies.

2.2.1 Cu_2O structural properties, method of deposition and application

Cuprite (Cu_2O) is a stable oxide p-type semiconductor with a band gap of 2.17 eV [18] [19] in a simple cubic structure as shown in a fig (2.1). From fig (2.1) can be seen that, in a single unit cell, there are six atoms in which four copper atoms are placed in the fcc sub-lattice and each copper (Cu:Blue) atom is linearly attached to the two oxygen (O:Red) atoms which are in the tetrahedral sites of the BCC lattice with respect to the Cu atoms [20].

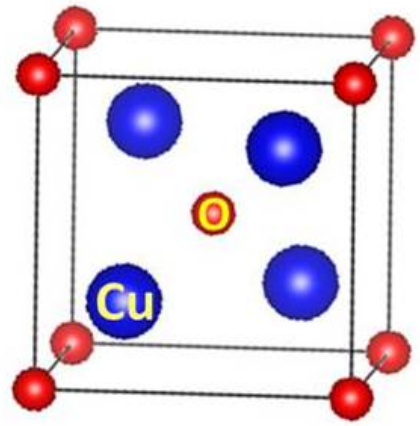

Figure 2.1: Crystal structure of Cu_2O (Cuprite) drawn using VESTA (visualization for electronic and structural analysis) software.

Cu_2O is non-toxic, abundant and is used for photovoltaic conversion [2], thin film hetro-junction solar cells [21], catalytic properties and thin film transistors [22] The bulk form of Cu_2O can be prepared by oxidising copper sheets [18], by hydrothermal processes, or by a seed growth (float-zone) process. However, for many applications, a thin film of Cu_2O is required. These films can be deposited using a range of techniques, e.g. evaporation [16], sputtering [17] [23], electro-deposition and chemical deposition [24]. Depending on the different deposition techniques and the substrate, the growth orientation of the film varies, altering the physical properties of the thin film.

A.A. Ogwu et al., [25] deposited CuO, Cu_2O and mixed phase of CuO + Cu_2O thin films using a copper target in an rf magnetron sputtering set-up. By varying the oxygen and argon gas ratio they could change the sheet resistance of the films. Films deposited at 200 W show $4.5x10^5$ Ω /square whereas increasing the power to 800 W decreases the sheet resistance to around 20 Ω/square.

Similarly, Valladares et al., [26] deposited Cu_2O and CuO thin film using a thermal oxidation method, They noticed CuO, Cu_2O and a mixed Cu oxide phase depending on their experimental conditions. Deposited films showed a sheet resistance that increased for

increasing annealing temperatures; from 0.06 - 1.3x10^{14} Ω/square.

Muslem F.Jawad et al., [27] deposited Cu_2O thin films by pulsed laser deposition on glass substrates using a 532nm Nd:YAG laser at 300°C and 500°C substrate temperature. In their studies, at 300°C the major plain orientation in the film is $\overline{(111)}$ and (200) where increasing the substrate temperature changes the major plain orientation to (111) and (020). The measured optical band gaps for Cu_2O and CuO thin films are 2.04 and 1.35 eV.

2.2.2 CuO structural properties, applications and method of deposition

CuO is a p-type semiconductor with a band gap of 1.2eV [20] [28] belonging to the monoclinic structure. CuO is naturally available in the form of a mineral called tenorite [18]. CuO has a unit cell, where a single Cu atom is attached with four oxygen atoms in a square planar configuration [28] as shown in the figure (2.2).

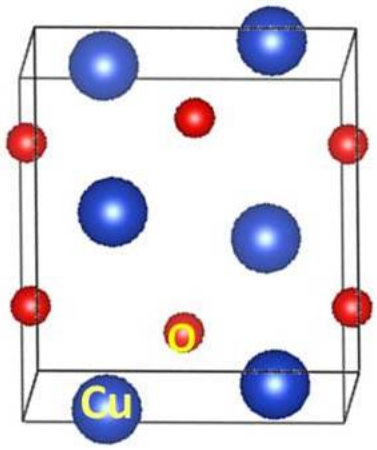

Figure 2.2: Crystal structure of CuO (tenorite)

It can be deposited using a range of deposition techniques; Yil-Hwan et al., [29] deposited CuO thin film using rf magnetron sputtering on Si wafers. At low pressure, the electrical resistivity as found to be very low (6.73x10^{-2} Ω cm) while increasing the pressure showed high resistivity (698 Ω cm).

M.A. Awad et al., [30] also deposited CuO thin films using dc magnetron sputtering. Their films were subjected to thermal treatment at 350°C, 450°C and 500°C for 3 hours. They show that at 450°C there is a mixed phase of CuO and the electrical resistivity is 2.92 x 10^1 Ωcm. The sample at 500°C shows higher resistivity (8.16 x 10^2 Ωcm) than thermally treated samples at low temperatures.

Forming different shapes during materials synthesis can also enhance the physical properties. E.g. Ahmad Umar et al., [31] synthesised CuO nano sheets by chemical methods which shows potential for gas sensing applications due to the (110) lattice plane growth.

In the section below, different thin-film deposition techniques will be discussed.

2.3 Classification of deposition techniques

Over the last century, many different thin film deposition techniques have been developed. These can be broadly classified as shown in Figure 2.3:

- Physical Vapor Deposition (PVD)
- Chemical Vapor Deposition (CVD)
- Electrochemical Deposition (ECD)

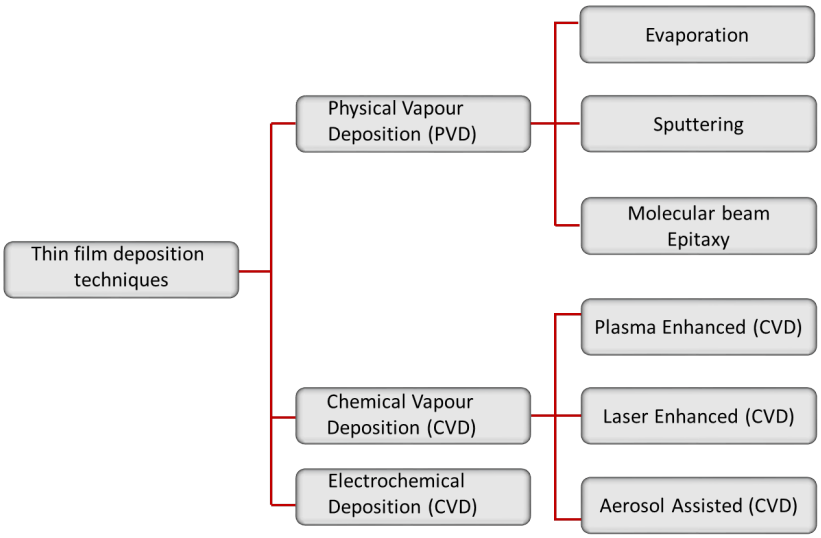

Figure 2.3: Classification of thin film deposition techniques

Independent of what type of deposition technique is used, they all need to satisfy certain requirements such as, uniformity, a very good control over film thickness, good adhesion between coating and substrate, so that the coating does not peel off from the substrate and most importantly the crystal structure of the film deposited must be pure because it will affect the properties of the film.

2.3.1 Physical vapour deposition

In physical vapor deposition techniques, the material which is to be deposited is taken in solid state and deposited as atoms on the substrate without any chemical reaction. The physical processes used in these PVD techniques can be classified as athermal and thermal processes. During athermal processes, externally ionised gas is fed into the chamber, where these ionised gas atoms strike the target material which is vaporised and then deposits as thin film [32]. Thermal PVD processes involve thermal heating of the target material For example: laser irradiation of targets. The common types of PVD techniques are evaporation, sputtering and molecular beam epitaxy, which will be discussed briefly below.

2.3.1.1 Evaporation

Evaporation is one of the most straightforward physical vapour deposition techniques. In this method, an evaporation source (eg: thermal, e-beam or both) is used to evaporate the target material, which then deposits as a thin film on the substrate. The whole process is carried out in a vacuum chamber to avoid contamination of the thin film. The schematic set-up is shown in fig 2.4. Based on the source used for evaporating the material, types of evaporation can be classified into

- Thermal evaporation
- Electron beam evaporation
- Pulsed laser ablation

A description of PLD and experimental set-up relevant for the thesis will be discussed in the chapter 4.

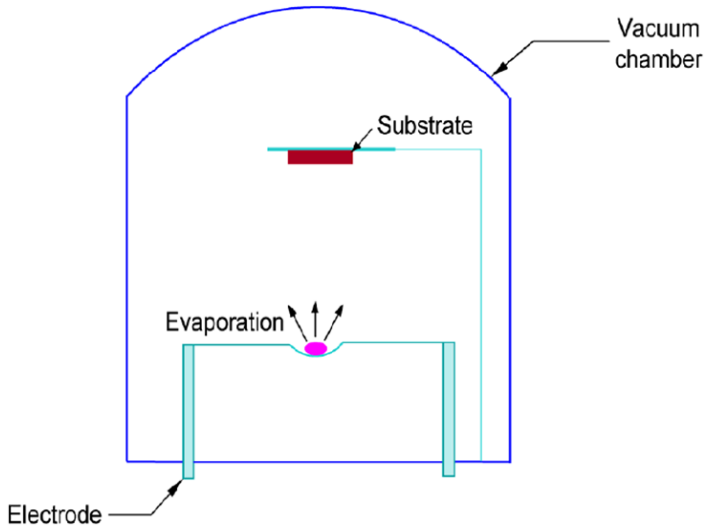

Figure 2.4: Schematic of standard evaporation techniques

The desired material for deposition is placed on a stage and heated by means of electrodes. The pressure inside the chamber is maintained in the range 1×10^{-8} – 0.1 Pa.

Upon heating, the target material goes through a liquid phase to a vapour phase.

This vapour gets deposited on the substrate, which is placed parallel to the target. Depending on pressure, the mean free path of the vapour material varies and hence the stoichiometry and thickness of the film varies. A limitation of the evaporation technique is problems achieving conformal coatings, because the vapour atoms/molecules are transported in a straight line from target to substrate. In order to overcome this, various strategies such as usage of multiple sources, revolving substrates, and utilizing laser beams have been developed http://nptel.ac.in. Y.H.Navalea [33] deposited CuO thin films on glass substrates using a thermal evaporation technique. Deposited without annealing, these films showed poor response for gas sensing applications. However, annealing the film up to 700^{o}C improved the response considerably.

2.3.1.2 Sputtering

Sputtering is one of the most utilized PVD techniques. It involves dislodgement and ejection of source material from a solid surface and deposition on a substrate. Fig 2.5 illustrates the sputtering process schematically.

Generally, the sputtering process takes place in an inert atmosphere, where inert gases like Ar or He are used at a low pressure of around 15 Pa. Upon applying a high electric field of typically 10 kV/cm, free electrons are accelerated and the Ar/He atoms can be ionized. The generated Ar^{+} or He^{+} ions strike the source electrode and ejects the target atoms. These ejected target atoms are deposited on the substrate which is kept parallel to the cathode (target). It is to be noted that along with neutral target atoms other charged species will also interact with the substrate surface and the grown film. Such interaction between the grown film and the charged species would lead to simultaneous sputtering of the grown film. In order to prevent such simultaneous sputtering, the target is capacitively coupled to a generator, applying a DC bias to the target, preventing the charged ions from reaching the target.

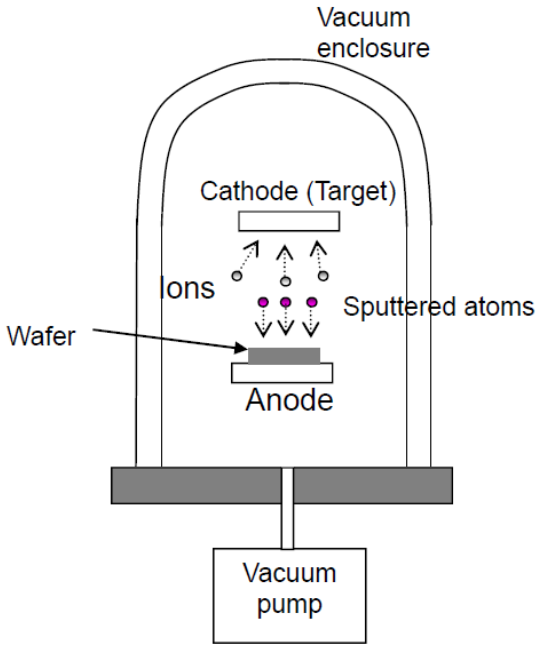

Figure 2.5: Schematic representation of sputtering technique in a vacuum chamber

Advantages of sputtering processes are (i) wider choice of materials, (ii) better adhesion to substrate, (iii) complex stoichiometry can be deposited, (iv) films can be deposited over large surface (process can be scaled), (v) deposition rate is proportional to yield for a given plasma energy. While the disadvantages of sputtering technique are high cost of equipment, substrate heating due to electron (secondary) bombardment and slow deposition rate (1 atomic layer/sec).

2.3.2 Chemical vapour deposition

Chemical vapour deposition (CVD) is the process in which thin films are deposited through chemical reactions during the deposition process. Usually, a chemically reactive volatile compound will be used as feed gas, which subsequently reacts with other gases to produce a non-volatile product that is deposited on the substrate as a film. The main application area of the CVD technique is the electronics industry, where this technique is used for the fabrication of various micro-electro mechanical structures (MEMS).

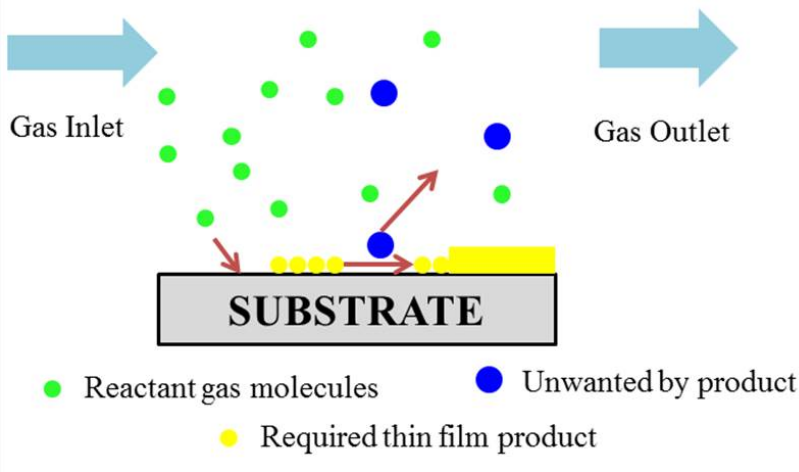

Figure 2.6: Schematic of chemical vapour deposition process

The working principle of the CVD technique can be found in Fig 2.6. Precursor gases are pumped into the reaction chamber. These precursor gases are transported to the substrate surface, were they get adsorbed, react and diffuse to nucleate the thin film growth. All by-products other than the required thin film product are pumped out. It should be noted that the CVD process is an intricate combination of both gas phase and surface chemical reactions. Too high concentrations of reactants in the CVD process can make the gas phase reactions dominant, which leads to homogeneous nucleation, which will not provide good quality films. Therefore, careful control of the concentration of precursor gases, temperature and pressure are needed in the CVD technique.

Several variations on the CVD technique have been developed for specific applications. This includes techniques that provide additional energy to activate the reactions (plasma-enhanced CVD, laser-enhanced CVD), and techniques that allow non-volatile precursors (aerosol-assisted CVD).

In plasma enhanced chemical vapour deposition, plasmas operating with frequencies ranging from 100 kHZ to 40 MHz are used as an energy source to instigate reactions. Whereas, in the case of low pressure-CVD techniques, a low pressure of 0.1 kPa is used for depositing thin films, as the low pressure can enhance the mass flux of reactant and products.

Recently, lasers were also used to assist the chemical reactions or deposition by pyrolytic processes, where the laser heats the substrate and induces gas decomposition, which increases the rates of chemical reactions. Finally, the aerosol assisted CVD has been developed for systems without gaseous precursors, low vapour pressures and low solid precursors. In this process, tiny droplets of liquid precursors are diffused in a carrier gas, where the precursor droplets diffuse with the background gas to react and grow as thin films.

2.3.3 Electrochemical deposition

Electrochemical deposition is a versatile technique that involves cations as a growth species during thin film deposition. This technique is mainly used for electrically conductive materials such as metals, alloys, semiconductor and conductive polymers. It is popularly known as electroplating.

During the electrochemical deposition process, an anode and cathode are immersed into an electrolyte solution and these electrodes are connected to an electric circuit. When the current is applied, the positive ions from the electrolyte solution are attracted towards the cathode, whereas, the negative ions move towards the anode. Thereby, the electrodes undergo oxidation and reduction processes, that gradually dissolves the anode into the electrolyte solution and deposits on the cathode (coating). Fig 2.7 shows an example of an electrochemical deposition process. It is the deposition of Ni-Gr by Zhaodi Ren and co workers [34] .

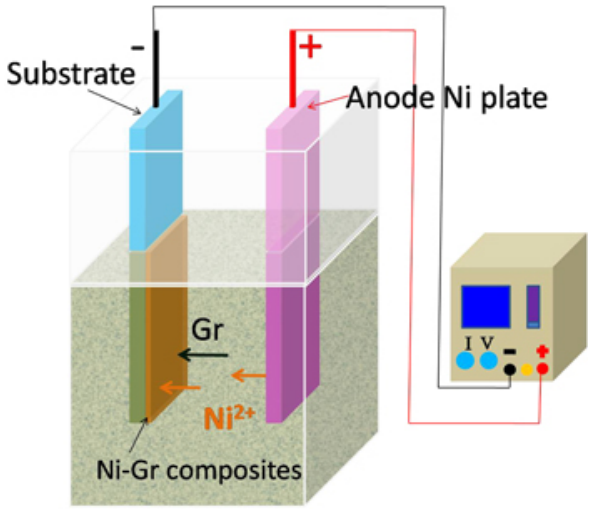

Figure 2.7: Electrochemical deposition Ni-Gr composites [34]

Chapter 3

Pulsed Laser Deposition

3.1 Introduction

Since the discovery of the laser in the 1960's, lasers are widely used in various fields of application. In particular, the development of high-power pulsed laser has impacted the field of thin film deposition. Pulsed Laser deposition (PLD) is a versatile thin film deposition technique that is widely used in semiconductor industry, metallurgy and material science, for instance for the production of solar cell thin film [35], photovoltaics [36] and transparent conducting films [37]. The principle of PLD is straightforward: A high power laser is focussed on a target, ablating solid material, turning it into a plasma. This plasma plume moves away from the target and deposits on a substrate as a thin film with the same stoichiometry as the target material. This process is schematically shown figure (3.1).

The phenomenon of PLD has been reviewed by several authors [38] [39] [40] [41]. In summary, when a high power laser is focused onto a solid target five different stages of interaction take place. First: the solid surface starts to absorb the energy of the laser light. Second, the absorbed energy results in the heating of the target. Once it reaches the melting temperature, the target starts to melt and subsequently vaporise if heating continues.

Next, the gas is turned into a plasma; the ionisation occurring through a combination of multiphoton ionisation and electron impact ionisation. Plasma heating occurs via inverse bremsstrahlung absorption of the laser light by the free electrons and subsequent collisional thermalisation with ions and neutrals [42]. The fourth stage is expansion of the hot plasma away from the target, and the final stage is the deposition on the substrate surface a as thin film. Fig (3.2) gives a schematic overview of laser-target interaction, i.e the first 3 stages of PLD. In the remainder of this chapter, the physics behind the different stages of the PLD process will be discussed in more detail.

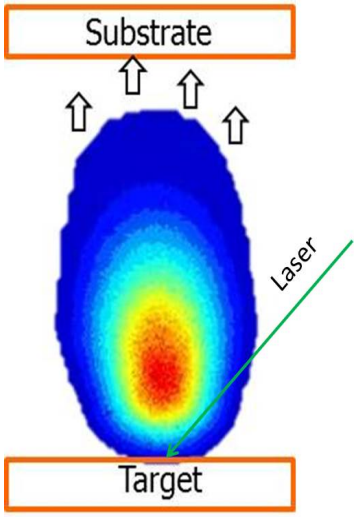

Figure 3.1: The schematic representation of PLD process

3.2 Laser energy absorption in solid materials

The absorption of laser energy in the target strongly depends on the type of material used for ablation. During initial laser-solid target interaction, photon energy is directly coupled with the excited and vibrational states of the material [43]. Based on the freely available electrons and the bandgap materials, and the laser energy absorption, into the material can be classified as metals, semiconductors and insulators.

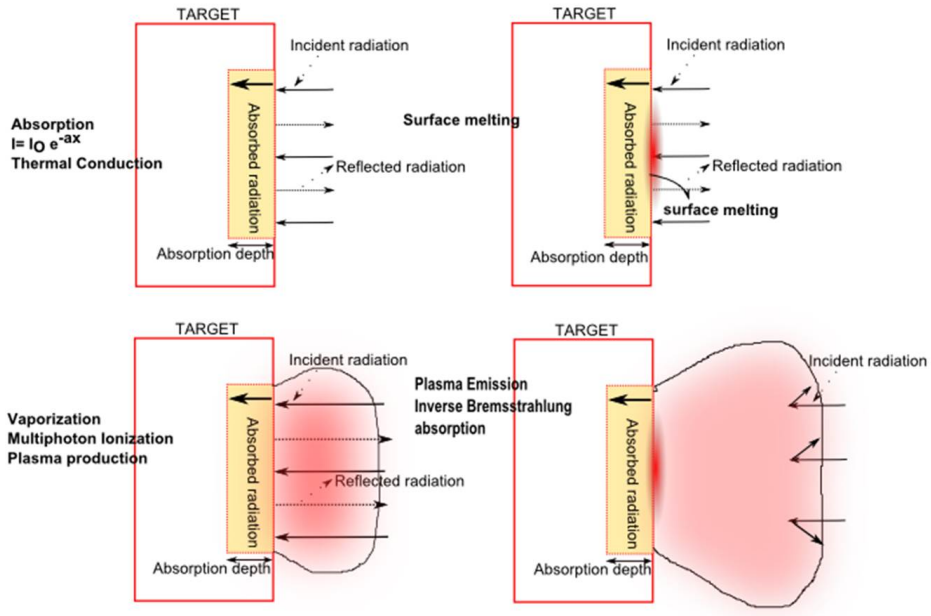

Figure 3.2: Schematic representation of laser target interaction

In metals, the absorption of energy is initiated by the free electrons which involves inverse bremsstrahlung absorption. The absorbed energy is eventually transferred to the conduction electrons in the gas. Subsequently, the electron energy is transferred to the atoms present in the lattice. It can be shown that the thermal diffusivity of to the metal will be of the order of $\sqrt{Dt}$ [44] where t is the laser irradiation time and D is the thermal diffusivity. Typical thermal energy transfer times between hot electrons and lattice phonon is order of $10^{-12} - 10^{-10} s$ [43]. This means that for nanosecond lasers it is possible to explain the details of phase transformation (i.e thermal vaporization from the heated surface to the liquid phase) in a classical way. On the other hand, the energy absorption and relaxation time is different for picosecond and femtosecond lasers. During the short pulse energy absorption, energy distribution among the particles is slow so the heating of the lattice will be different and relatively slow for picosecond lasers.

Another important parameter for energy absorption in a laser-solid interaction is

plasma frequency ω_p [43] [45]

$$\omega_p = \sqrt{N_e e^2 / m_e \varepsilon_0} \tag{3.1}$$

where, N_e, m_e and ε_0 are the electron density, mass of the electron and permittivity of free space.

Only light with a frequency higher than the plasma frequency can pass through a plasma. Since all frequencies lower than the plasma frequency will cause the electrons in the plasma to oscillate and take energy from the light beam, i.e. absorbing it. In case, if the incident light frequency is less than the plasma frequency, electrons in the plasma response to the incident radiation and absorb energy from it. Particularly in metals due to the high conduction electrons and plasma frequency, the absorption of energy will be high.

For example, the solid density Cu, ρ is 8.96 g / cm^3, the density of atoms (and therefore electrons) is of the order of 10^{29} m^{-3}. The corresponding plasma frequency for this density is 100 nm. This means that the light from almost all common lasers is at longer wavelengths than the plasma frequency and therefore will be absorbed very efficiently. For 532 nm, the laser wavelength used in this thesis, the critical density, i.e. the density at which the plasma frequency is equal to the laser frequency, is about 4 x 10^{27} m^{-3}. So, very close to the there will be a layer of high density plasma, falling from solid density toa typical plasma density of say $10^{24} m^{-3}$ in the plume. In that case, the 532 nm laser will not get to the solid surface any more, but the light will be absorbed by the plasma at the critical density, i.e.in the plasma just in front of the target. Still, the actual plume is below critical density and even though it will absorb laser energy via inverse bremsstrahlung, the majority of the laser beam will pass through this part of the plasma.

In metals, due to the overlap of valence and conduction band and therefore the availability of free electrons, the energy absorption is relatively high. Whereas, in semi-conductors, the energy gap between valence band and conduction band is significant. Laser photons will therefore create electron-hole pairs (if the photon energy is sufficient), instead of

heating free electrons through Inverse Bremsstrahlung absorption. The creation of electron-hole pairs leads to the transfer of an electron from the valence band to the conduction band with the electron having a kinetic energy of $h\nu - E_g$ [44].

For insulators, even more photon energy is required to free an electron, In very intense lasers, the multiphoton absorption process can produce a conduction electron. These conduction electrons start to collide with lattice atoms and can knock out an electron from the atom which creates hole.

3.3 Heating, melting and vaporisation of target

The absorption of laser light through the different mechanisms described before, all lead to increased lattice vibrations of the material, i.e. heating of the target.

The details of the heating of the targets strongly depend on the properties of the laser pulse. The heat equation (3.2) [46] is used to calculate the target temperature at various depths where no phase change occurs in the material. When the incident laser intensity is low ($< 10^8$ W/cm^2), no phase change of the target material is encountered, instead the only process to take place is heating.

The next phase is melting of the target, that is if the absorbed energy is high enough that the temperature of the target reaches its melting point. This is one of the important criteria for welding application, where one needs the surface to be melted rather evaporated. However, for the Q-switched, pulsed laser used in this thesis, melting of the target is often no completely achieved due to the short pulse and high flux densities. In this case, change of phase from solid to liquid is small in comparison to the phase change between liquid to vapour.

The next important stage before the plasma formation is vaporization of target.

During the laser target interaction, when the surface of the target reaches it boiling point it starts to vaporize. Therefore, the thermal conductivity and specific heat capacity of latent heat of the material are very important.

$$\frac{\partial T(x,t)}{\partial t} = \frac{\partial}{\partial x}\left[\left(\frac{\kappa}{C_p \rho_s}\right)\frac{\partial T(x,t)}{\partial x}\right] + \frac{\alpha}{C_p \rho_s} I(x,t) \tag{3.2}$$

Material with low thermal conductivity will vaporize more material at low flux density, since the energy absorbed near the focal point can not easily diffuse to nearby areas which significantly raises the temperature of the target and more amount of material is vaporized than for material with high thermal conductivity.

Other than thermal conductivity, another important parameter is heat capacity of the material, since, heat capacity determines the time t_v taken by the surface to reach its boiling point. This can be calculated from a 1-D heat flow equation (3.3) [44]. Where κ is the thermal conductivity of the material, ΔT is temperature required to raise the surface to its boiling point, F is the laser flux density and C_p is the heat capacity per unit mass.

$$t_v = \frac{\pi \kappa \rho C_p}{4F^2} \Delta T \tag{3.3}$$

$$V = \frac{F}{c\Delta T + L_v} \tag{3.4}$$

Once when the material vaporises, the rate of vaporization ($g\ cm^{-2}s^{-1}$) can be approximated by equation (3.4),

3.4 Plasma formation

For nanosecond-duration lasers, the plasma formation is initiated by a combination of multiphoton ionisation and electron impact ionisation. This plasma is further heated by inverse bremsstrahlung.

3.4.1 Multiphoton Ionisation

In the photo-ionisation process, an atoms or molecules absorbs a photon from the laser. If the energy of this photon is above the ionisation potential of the atom/molecule, it will be ionised.

However, in practice, for most materials and lasers used in PLD this photo-ionisation process do not occur. Typical materials e.g Cu, Zn, have ionisation potentials of 5-10eV while the most commonly used lasers have photon energies ranging from 1.1eV(1064nm) to 5.48eV(226nm) or 6.42eV excimer laser ArF (193nm).

However, at high photon fluxes the process of multi-photon ionisation can become significant. In this process more than one photon is absorbed simultaneously by the atom/molecule. If the cumulative energy of these photons is more than the ionisation potential the atom/molecules will be ionised. The cross-section for multi-photon ionisation processes rapidly decreases with increasing number of required photons.

$$M + n(h\nu) \longrightarrow M^+ + e^- \tag{3.5}$$

where, n is the number of photons, $h\nu$ is the energy of the photon. An example relevant to this thesis, is a target of Cu, ablated by a 532 nm Nd:YAG laser. The first ionisation potential of Cu is 7.7268 eV and the laser photon energy is 2.33 eV which means that in order for the multiphoton ionisation mechanism to occur we need 4 photons to initiate the ionisation process. The cross-section for the simultaneous absorption of 4 photons is very small, making the process of multi-photon ionisation for our conditions of minor importance.

3.4.2 Electron impact ionisation

In the electron impact ionization process, an electron collides with a neutral gas particle. If the transferred kinetic energy is above the ionisation potential of the gas particle, it will be ionised:

$$e + M \longrightarrow 2e^{-} + M \tag{3.6}$$

As can be seen from Eq. 3.6, there are two free electrons after the collision which means there is a multiplication of free electrons. If the free electrons can gain energy in between collision processes, e.g. through inverse Bremsstrahlung, then both electrons can cause new electron impact ionisation processes and an electron cascade can form. The initial seed electrons needed for such an electron cascade can come from either naturally available electrons in the atmosphere ($10^2 - 10^3 cm^{-3}$) [42] or from multi-photon ionisation processes.

The relative importance of multi-photon ionisation and electron-impact ionisation depend strongly on the properties of the laser pulse (e.g. wavelength, duration, intensity) and the gas particle density. For short wavelengths and low particle densities, multiphoton ionization dominates. Whereas, for longer wavelengths and higher gas densities, electron impact ionisation and inverse bremsstrahlung are more important.

3.4.3 Plasma heating by Inverse Bremsstrahlung

Inverse bremsstrahlung absorption is a process in which a free electron interacts with the incoming laser light, absorbing energy and increasing its kinetic energy.

In the inverse bremsstrahlung absorption process, for high ion densities, the electron-neutral interaction is relatively small when compared with electron-ion interaction. Therefore, inverse the bremsstrahlung absorption coefficient due to electron-ion interaction is given

by:

$$\alpha_{IB}(cm^{-1}) = \left[\frac{4e^6\lambda^3 Z^2 n_e n_i}{3hc^4 m_e} \times \sqrt{\frac{2\pi}{3m_e k_B T_e}}\right] \times \left[1 - exp\left(-\frac{hc}{\lambda k_B T_e}\right)\right] \tag{3.7}$$

Rearranging equation (3.7) gives:

$$\alpha_{IB}(cm^{-1}) = 3.69 \times 10^8 \frac{Z^2 n_e n_i \lambda^3}{T_e^{1/2}} \left[1 - exp\left(\frac{-hc}{\lambda k_B T_e}\right)\right] \tag{3.8}$$

where, n_e and n_i are densities of electron and ion in cm^{-3}, λ is a laser wavelength used, Z is the average ion charge, c, h and T_e are the speed of light, Planck's constant and electron temperature. If we consider our plasma to be in thermodynamic equilibrium, then $n_e = n_i Z$ and eq (3.8) further simplifies to,

$$\alpha_{IB}(cm^{-1}) = 3.69 \times 10^8 \frac{Z^2 n_e^2 \lambda^3}{T_e^{1/2}} \left[1 - exp\left(\frac{-hc}{\lambda k_B T_e}\right)\right] \tag{3.9}$$

IB absorption results in further ionisation and therefore n_e increase such that n_e goes above the critical density and therefore IB stops for that part of the plasma. Then, because it keeps expanding, the density goes down again (because of the expansion) therefore n_e drops below critical again and IB starts again for that part of the plasma. In this trend, self regulation of the plasma takes place and it expands throughout the entire laser pulse.

3.5 Plasma expansion

The next stage of PLD is plasma expansion. This phase describes the expansion of the plasma that is created by the laser-target interaction. The time scales are of the order of microseconds which is significantly longer than the (sub-) nanosecond duration of the laser pulse and therefore laser-target interaction. *Zeng et.al* [47] shows that the plume shape and expansion velocity depend strongly on the characteristics of the laser pulse forming the plume (e.g. laser duration, wavelength, energy). In the following section, both plasma expansion

in vacuum and background gas will be discussed.

3.5.1 Plasma expansion in vacuum

Plasma expansion in a vacuum is a well-studied problem, both from a fundamental physics point of view as well as for applications, e.g. think film deposition. Recently, there has been a renewed interest in this area for applications in the field of space thrusters [48] and laser produced nanoplasma [49]. During a typical ns laser ablation, the ablation rate is greater than 0.1 monolayer/sec and a density of the order of $(10^{18} - 10^{20} cm^{-3})$ is initiated near the front of the target. Since, the particles are in a vacuum, the expansion of the plasma can be considered to be adiabatic which means that there will be no transfer of heat or mass from the plasma to the environment.

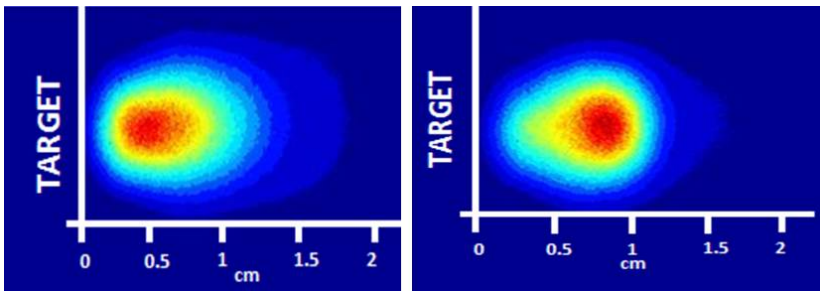

Figure 3.3: Laser produced plasma plume expansion at 13 Pa and 20 Pa at 100ns

The particles close to the target show an anisotropic velocity distribution, but due to a scattering between the plasma particles, the anisotropic velocity distribution will be modified into an isotropic velocity distribution in order to maintain a thermal equilibrium in the plasma. This kind of transition layer is called as **Knudsen layer**. Once the Knudsen layer is formed, due to a limited number of collision in the vacuum, the velocity distribution of the particles can be fitted using a shifted Maxwell-Boltzmann distribution eq (3.10): [50]

$$f(v) = A\left(\frac{m}{2\pi k}\right)^{\frac{3}{2}} exp\left(\frac{-m(v-u)^2}{2kT}\right) dv \tag{3.10}$$

Here, u and v are the expansion velocity and speed along propagation direction, m and k is the mass of the particle and Boltzmann constant [46].

3.5.2 Plasma expansion in background gas

When the plasma plume does not expand into a vacuum but into a gas background, there can be a significant change to the expansion process. Exactly what the differences are depends on the pressure of the background gas. When the pressure is low, ($< 1Pa$), the plasma species behave like the species in a vacuum. Whereas, for pressures in the range ($10Pa - 100Pa$) the dynamics of the plasma plume will be influenced by the gas background in the form of a shock wave and the plasma plume is significantly slowed down due to the compression of the background gas. Fig (3.3) is an ICCD image of a laser produced Cu plasma expansion at 13Pa and 20 Pa; showing a compressed front edge of the expanding plume in the 20 Pa case compared to the 13 Pa case.

The expansion distance D as a function of time t can be calculated using Sedov's blast wave theory equation (3.11),

$$D = \lambda_0 \left(\frac{E_0}{\rho_1} \right)^{1/2+d} t^{2/2+d} \tag{3.11}$$

where d represent the shape of the plasma during expansion, for a spherical shape $d = 3$, for cylindrical $d = 2$ and for planar propagation $d = 1$. E_0 and ρ_1 are the laser energy per area and ambient gas density, λ_0 is a dimensionless constant which depends on the specific heat capacity of material [46]. Fig (3.4) represent the time resolved images of stainless steel laser ablation for femtosecond (fs) and nanosecond laser (ns). From the images we can see that, for fs laser, the expansion of the plume is predominantly perpendicular to the substrate, While for ns laser the lateral expansion is gradually increasing with increasing time. Based on Sedov's blast wave theory, the expansion of plasma plume for fs laser is proportional to

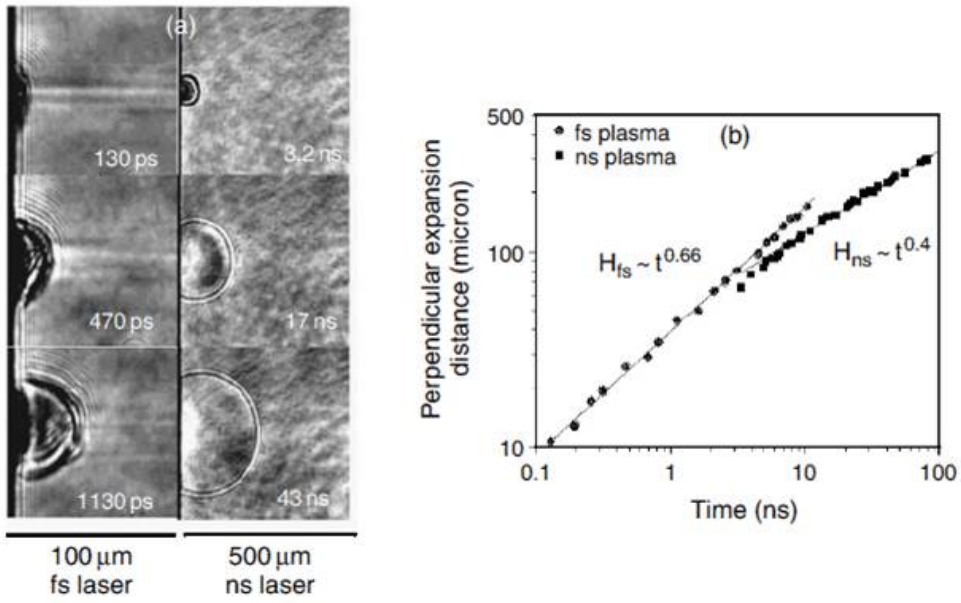

Figure 3.4: (a) Shock wave image for femtosecond and nanosecond laser ablation (b) Perpendicular plume expansion distance for femtosecond and nanosecond laser ablation driven shockwave [46], [47]

$t^{\frac{2}{3}}$ and for ns laser ablation it is proportional to $t^{0.4}$.

3.6 Thin film growth mechanisms

In the final phase of PLD, plasma consisting of target atoms and electrons moves towards the substrate to deposit and grow as thin film. Based on the growth dimension this process can be classified into three modes, 1. Frank-van der Merwer (layer-by-layer growth), 2. Volmer-Weber (island growth), 3. Stranski-Krastinow(combination of layer-by-layer and island growth). These different modes will be discussed in more detail in the next section. Figure(3.5) shows the range of atomic processes that can happen on the substrate during thin film growth. An important one determining the growth mechanism is the diffusion of atoms along the surface.

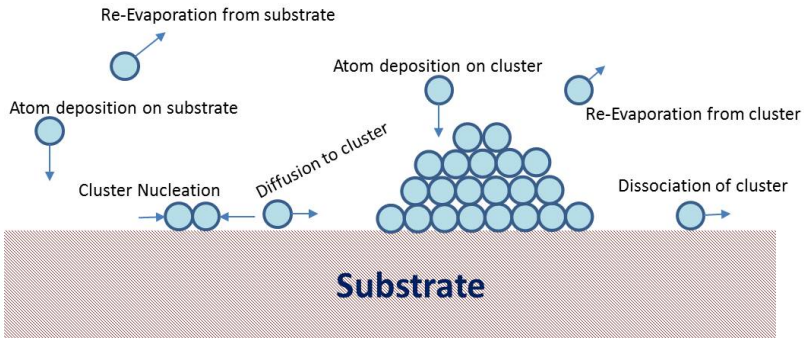

Figure 3.5: Schematic of possible atomic process happen on substrate during thin film deposition [51]

The energy of the atoms arriving at the substrate depends strongly on the experimental conditions. Therefore, atoms arriving and diffusing on the surface can start growing in three different modes. In the section below these three different ways of thin film growth modes will be discussed.

3.6.1 Frank-van der Merwe growth mode

This mode is the preferred growth mode for uniform thin films. A monolayer of atoms is formed on the substrate and followed by single layer of atoms on top of each monolayer as shown in the figure 3.6.

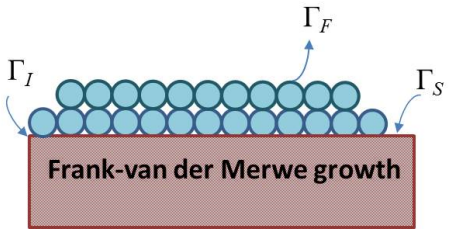

Figure 3.6: Frank-van der merwe: Layer-by layer growth mode

The condition for layer-by-layer growth to occur is expressed in equation (3.12). Here, in the equation (3.12), Γ_F, Γ_S, Γ_I are free energies of film, substrate and interface. In

case, $\Gamma_I = 0$ and $\Gamma_F = \Gamma_S$, i.e plane orientation and free energies of the film and the surface are the same, If the film is deposited on clean surface the conditions for monolayer growth are easily satisfied. Whereas, to achieve a layer-by-layer growth throughout the deposition for different substrate and film plane orientations, the free energies of the substrate should be high compared to the free energy of the film and interface. Under such conditions the bonding between the substrate and the film will be strong, initiating monolayer formation.

$$\Gamma_I + \Gamma_F \leq \Gamma_S \tag{3.12}$$

Layer-by-layer formation does not necessarily mean a single layer of atoms across the whole substrate, followed by another single layer. It is possible to nucleate several islands, which each grow layer-by-layer and eventually fuse with nearby islands into a continuous film. In this way, layer-by-layer formation can be achieved for lattice mismatched substrates and thin films.

3.6.2 Volmer-Weber growth mode

This type of thin film growth mode, also known as island growth, is characterised by the formation of several small islands of several monolayers thickness. It is initiated when the vaporized target atoms start to diffuse onto the substrate or on the pre-existing thin film cluster.

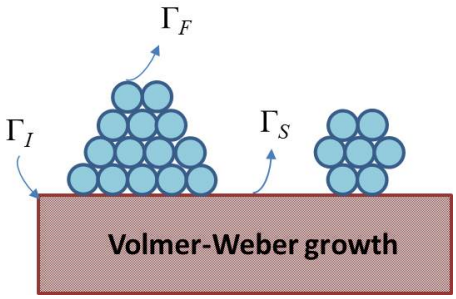

Figure 3.7: Volmer-Weber growth: Island growth mode

As indicated in eq (3.13), this growth mode occurs when the sum of free energies of the film and interface is larger than the free energy of the substrate. This allows the vaporised atoms to start to diffuse onto the substrate surface to form clusters. During the cluster growth, the free energy of the cluster is increased by the addition of small atoms. Once the cluster reaches a critical size, any further addition of atoms results in a decrease of free energy. The result is that a steady state is reached and the cluster growth become small. It is now more favourable to start a new cluster on a free position on the substrate. This process continues until the substrate surface is completely covered.

$$\Gamma_I + \Gamma_F > \Gamma_S \tag{3.13}$$

Hoseok Heo et al., [52] showed the difference between layer-by-layer growth and island growth for Bi_2 Te_3/Sb_2Te_3 thin film on h-BN and SiO2/Si substrates. Due to the lattice mismatch, the stacking of Bi_2 Te_3 and Sb_2Te_3 on two different substrates induces strain on the growth substrate and changes the growth modes and the film properties.

3.6.3 Stranski-Krastinov growth mode

A combination of both monolayer and island growth is known as Stranski-Krastinov growth, as schematically indicated in figure 3.8.

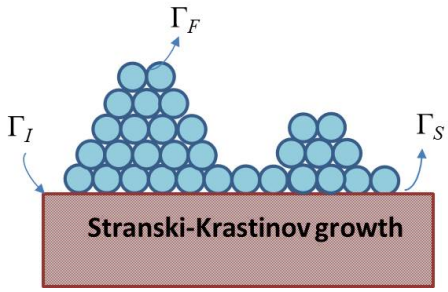

Figure 3.8: Stranski-Krastinov growth: combination of layer-by-layer and island growth

In this mode, typically 1-5 monolayers [51] are formed on the substrate followed by the formation of island growth. This type of growth is initiated due to the increase in the stress between substrate and film. This stress in relieved by forming a monolayer followed by the cluster nucleation and island growth. This kind of growth is mostly seen for lattice mismatch greater than 2%.

Michael A. Fusella et al., [53] grown rubrene thin films on ITO substrates and by varying the growth rate and substrate temperature they saw a clear transition from layer-by-layer to island growth. The first 10nm was observed to be layer-by-layer growth, followed by island growth due to large lattice mismatches.

3.7 Factors influencing deposition process

It is clear that the properties of the deposited thin film depend strongly on the parameters of the deposition process [54], [55]. In this section, I will discuss several important operational PLD parameters and how they affect the ablation and deposition processes.

3.7.1 Laser Irradiance, laser pulse width, pulse shape and laser wavelength

Laser irradiance (laser irradiance = pulse energy/(focal spot area $\times$ pulse width)) is one of the important parameters during thin film deposition process. Mostly during laser interaction, the laser irradiance could be either below or above the ablation threshold of the material. If the laser irradiance is below the ablation threshold, inverse bremsstrahlung becomes significant in the forming plasma. On the other hand, if the incoming laser irradiance is close to the ablation threshold, multiphoton ionisation plays a role in the process of initiating plasma. Equation 3.14 describes the threshold intensity as function of material parameters. It will undergo shock wave formation in two different ways; one for the species travelling normal to the target under background atmosphere and the other will be inside

the target [56] .

$$I_{th} = \frac{T_b}{\alpha}\sqrt{\frac{\kappa\rho c_p}{t_p}} \tag{3.14}$$

where T_b , α, κ, ρ and c_p are material dependent properties which represent the boiling temperature, absorption co-efficient of the material, thermal conductivity, density and specific heat capacity of the material. t_p is the pulse width which is a laser property. Equation (3.14) shows that, in order to evaporate material before the laser pulse ends, the incoming laser irradiance (I) should be greater than the threshold irradiance ($I > I_{th}$). It is also clear that the amount of material leaving target surface depends on threshold, melting point and boiling point of the material. Therefore, for higher incoming laser, the kinetic energy of low ablation threshold will be faster than the high ablation threshold of the material. It is also important to note that for a high irradiance on a low-ablation threshold target, a plasma will be created with a high temperature, i.e. there is a large amount of laser energy available to heat the plasma after ablation. It also means that even though with a higher irradiance you can ablate more material, the plasma that is formed will have a higher temperature, which is known to change the deposition behaviour [57]. In other words, the two effects are couples and not independent, complicating the control of the process.

V.J. Rico et al., [57] carried out an experiment by varying the laser irradiance to control the plasma heating and ablation process efficiently so they were able to achieve uniform Cu_2O / CuO smooth layered thin film.

Furthermore, other laser parameters, e.g. such as pulse duration has a significant impact on the ablation and deposition process. The main point is that the underpinning physics is very different. For ns pulses, there is mainly melting and then evaporation and plasma heating, For fs pulses there is no time for that and there is limited melting and this then has an impact on the average temperature (or kinetic energy) of the plume.

J.Perrie and co-workers [58] carried out experiments growing ZnO thin film using

fs and ns lasers. For ns pulsed laser deposition, they were able to produce good quality single crystalline thin film. The thin films deposited using fs laser showed poor quality thin film due to the high kinetic energy of the plume.

Another important parameter considered to be important during thin film deposition and applications like drilling and welding is the laser wavelength. One of the reasons is that the absorption coefficient of the target is different for different laser wavelengths. Furthermore, the plasma heating by inverse bremsstrahlung is proportional to λ^3 as shown in equation 3.10. Hence, the plasma generated using IR lasers tends to have high temperature compared to UV lasers. Second, the contribution of multiphoton ionisation to the plasma formation depends strongly on the laser wavelength. For high photon energies (UV wavelengths), fewer photons, typically 1-2 for most metals are needed for photo-ionisation, while for IR wavelengths often 4 or more photons are need to bridge the ionisation threshold. The cross section for these processes scales strongly with the number of photons required to ionise an atom.

Chapter 4

Plasma enhanced pulsed laser deposition (PE-PLD)

4.1 Introduction

This chapter first introduces the experimental details of the Pulsed Laser Deposition (PLD) technique, after which our novel Plasma-Enhanced PLD technique is described.

4.1.1 Pulsed laser deposition

Pulsed laser deposition is one of the physical vapour deposition techniques and it was first established by Smith and Turner in 1965 [59]. It has been a popular technique for growing semiconductor thin film [60], ferroelectric materials [61], high temperature superconducting films [13], thin films for studying optical band gaps (CuO) [27], gas sensing [62] applications and as transparent conducting oxide films (ZnO) [63].

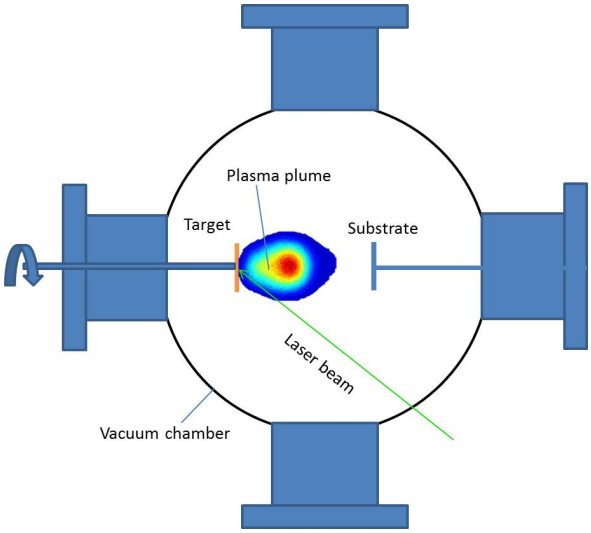

Figure 4.1: Schematic of PLD set-up

A schematic diagram of the standard PLD setup that was used for the work in this thesis is shown in Fig (4.1). It consist of a 6-arm vacuum cross with 200 mm outer diameter conflat flanges (Model: CF160); the front port is used for the diagnostic purpose. The pressure inside the vacuum chamber is maintained using a two-pump system. Initially, an oil-free scroll pump (Edwards nxDS 15i) is used as a backing pump and a turbo pump (Pfeiffer TPU 170) is used to achieve base pressure. If required, a flow of oxygen gas is introduced into the chamber to create a background gas pressure of 4-20 Pa. Then, a Q-switched 532nm Nd-YAG laser (Continuum Minilite II) with 5ns pulse width is focused by a lens through a quartz window on the Cu target (Testbourne, 99.99% purity).

In our experiment, for the standard pulsed laser deposition conditions, the distance between the target to the substrate is kept at 40 mm and the background oxygen gas is varied between 4Pa to 20Pa. Quartz is used as substrate for the thin film growth. This quartz substrate is initially cleaned using acetone and then kept in a 40°C heated ultrasonic ethanol bath for 20 min. Once it is taken from the ultrasonic bath, it is blow dried. This quartz substrate is loaded on to the substrate holder which is kept parallel to the rotatable target holder. During each deposition, a layer of target material is coated on the surface

of the top quartz electrode and this material is removed each time before the deposition by cleaning the window using acetone. Finally, the tightly focused laser from a 500mm lens impinges on to the target material and the subsequent thin film deposition on to the substrate takes place.The laser spot size was estimated to be 492 μm diameter from SEM images (as shown in figure 4.2). This gives a typical irradiance of 1767 MW/cm^2 and a fluence of 9.4 J/cm^2. The results and discussion of thin films deposited with the standard PLD set-up are discussed in chapter 8.

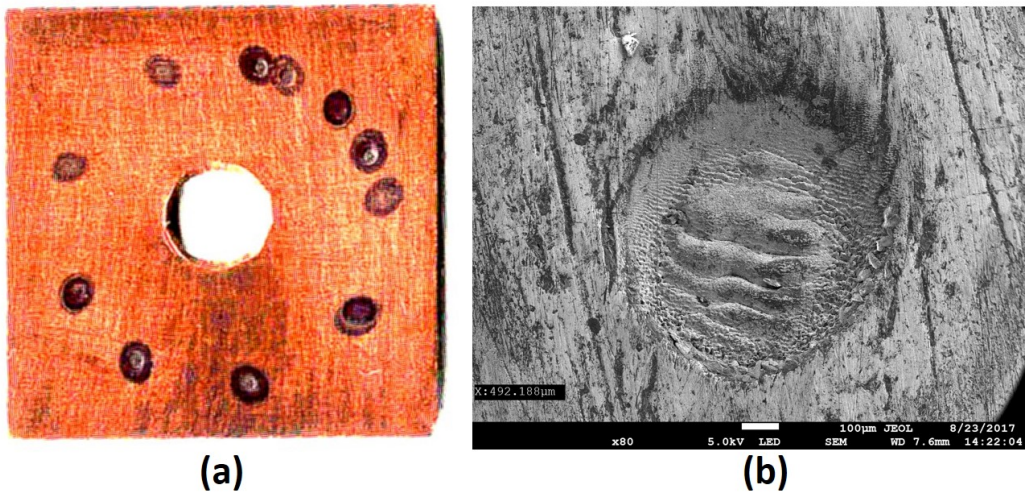

Figure 4.2: (a) Scanned image of Cu target and (b) spot size diameter of the laser shot calculated from scanning electron microscope

4.1.2 Advantages of pulsed laser deposition

Advantages of the PLD technique over other deposition techniques include:

(1) The technique itself is very simple to operate and compared with other sophisticated deposition techniques that need ultra high vacuum to deposit thin film e.g. (MBE)

(2) Deposition rates can be controlled by varying laser energy, laser wavelength, pulse width, pulse shape and target material(i.e the deposition rates are different for oxides and metal

target).

(3) Confinement of the laser-target interaction in the chamber attributes a clean process of deposition. Whereas, in sputtering techniques, plasma interacts with surfaces inside the chamber and this can contaminate the sample.

(4) A laser can be tightly focussed, which means that a small target is sufficient for deposition. This is an advantage when using complex or expensive targets.

4.1.3 Limitations of pulsed laser deposition

On the other hand, standard PLD also suffers from some limitations. Most notably, the two main limiations of PLD are [64]

(i) Material dependant limitations:

(a) Substrate heating and post annealing are often needed for depositing high-quality films.

(b) Difficult to use heat-sensitive substrates, e.g. plastics.

(c) PLD control parameters such as laser energy, wavelength, gas pressure are not independent, i.e. not ideal for controlling the process. For example, making CuO and Cu_2O requires different targets, this variation in stoichiometry cannot be controlled with background gas pressure.

(ii) Particulates:

(a) Creation of particulates in the plasma plume that can end up incorporated in the thin film, leading to low-quality films. During the deposition process, the size of the particulates

ranges from < 0.1 μm to 10 μm, and depends strongly on the laser energy and wavelength used.

(b) Furthermore, it is possible to create asymmetric fragmented particulates from the target that will affect the uniformity of the film.

(c) If the laser energy is too high, there will be heating and melting of the sub-surface, which leads to formation of molten droplets in the sub-surface, which in turn leads to splashing of the target material. These macroscopic droplets will be incorporated in the deposited film, leading to a non-uniform film.

(iii) Angular distribution of laser produced plasma species [64]: The angular distribution of the plume is in a forwarded direction and it is related to the $(cos\ \alpha)^n$ where α is the angle normal to the target (distance between target to the substrate and spot dimension) determines the uniformity of the thin film. It is known that for PLD n 5-25 [64], i.e. the plume is strongly in the forward direction. The need for this high directionality for good films is an issue with mixed targets, where the wider distribution of the plume leads to non-stoichiometric films.

4.2 Plasma enhanced Pulsed laser deposition (PE-PLD)

The main idea of PE-PLD is to produce metal oxide films from a metal target and a background oxygen plasma. I.e. all metal comes from the target, all the oxygen in the film comes from the background plasma, not just a small correction to the stoichiometry as is the case in standard PLD. In other words, the sources of metal and oxygen are separated, allowing independent control over both, enhancing the overall control of the thin films deposition process. In order to achieve this, a standard PLD setup needs to be extended to incorporate

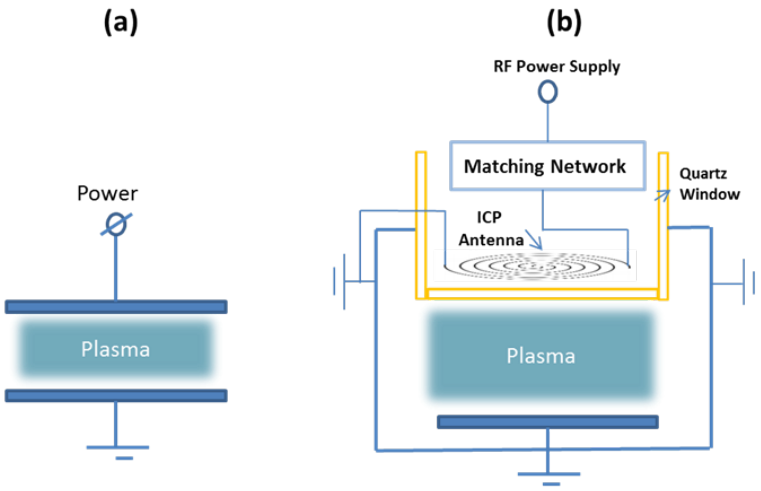

Figure 4.3: Schematic diagram of (a) Capacitively Coupled Plasma and (b) Inductively Coupled Plasma

an additional electrically-produced plasma source for reactive oxygen. The reasons for the choice for an Inductively Coupled Plasma (ICP) are discussed in some detail below.

4.2.1 Low-pressure processing plasmas

Plasma processing, etching and deposition, of large wafers is common practice in the semiconductor industry. Here, plasmas are needed that can generate high densities at low pressures, remain at a low temperature and are extremely uniform across the treated wafer surface. Radio-frequency-driven low-pressure plasmas have been identified as meeting these needs. Depending on the electrode configuration, these RF plasmas can be classified as Capacitively Coupled Plasmas (CCP), with 2 parallel metal electrodes, or Inductively Coupled Plasmas (ICP) where one electrode is replaced by an antenna, external to the plasma volume.

Figure 4.3 shows schematic diagrams of both the CCP and ICP configurations. For the CCP, 13.56 MHz RF generator is connected, via a matching network, to one of the electrodes, while the other electrode is grounded. The RF voltage sets up an (ac) electric field between the electrodes, which causes the electrons to accelerate and ionise feed gas atoms in the chamber via electron impact collisions. The ions are too heavy to respond to

the fast-changing electric field and therefore remain (almost) stationary at low temperatures. Excitation of atoms and molecules by electron impact collisions also results in light emission that can be observed.

In an ICP, the power coupling is inductive, via an external coil. In particular, ICP plasmas with a planar coil gained interest from the microelectronics industry because it can generate higher density plasmas than CCPs and have superior uniformity compared to traditional coil configurations. It is worth noting that depending on the details of the power coupling, ICP plasmas can be operated in a low-power E-mode or a high-power H-mode. This classification of low-pressure RF discharges is schematically shown in Fig 4.4 Further details will be discussed in the next sections.

4.3 Operating modes in Inductively coupled plasma

A typical ICP set-up (GEC reference cell [65]) is shown in the figure 4.3(b). Based on the power supplied to the coil it can be operated in two different modes (E-mode and H-mode).

These two different modes can be identified visually from the brightness of the plasma emission. At low power in E-mode, the visible plasma emission is relatively dim. An increase of RF power results in a sudden transition to the H-mode, which is much brighter. This can be clearly seen in the figure 4.5

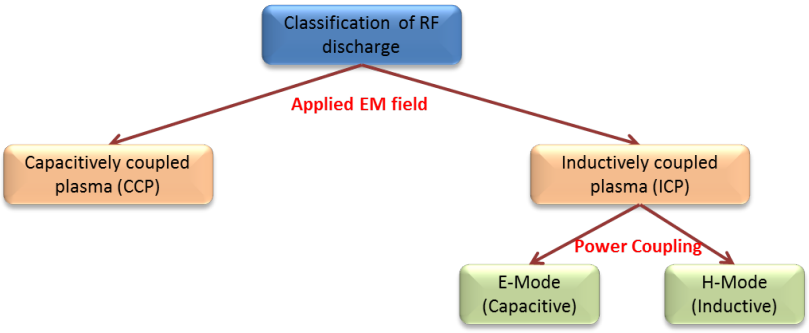

Figure 4.4: Classification of RF discharge

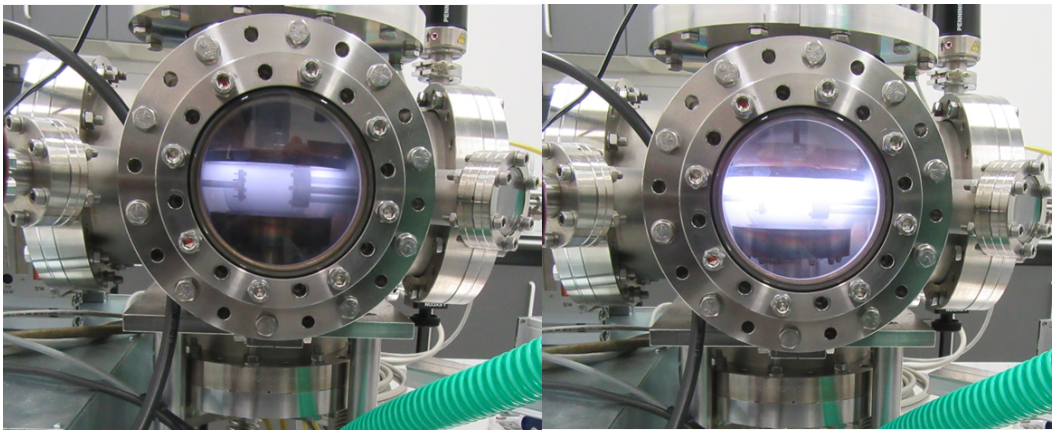

Figure 4.5: Operating ICP in E-mode (left) and H-mode (right)

The reasons behind the two distinct modes that are observed are the following: at low power, the current induced in the plasma by the coil is limited. At the same time, there is a voltage difference, and hence electric field, between the spiral coil and the grounded electrode. This electric field can generate a plasma in exactly the same way as in a CCP. In other words, in E-mode, the coil acts as the powered electrode of a standard CCP. Since this mode can only exist at low powers, the plasma density is low compared to H-mode.

In H-mode, at high power, the capacitive coupling of power is overshadowed by the inductive coupling. In other words, the coil acts as the primary coil of a transformer, with the plasma acting as the secondary coil. I.e. the current through the spiral coil initiates a magnetic field (Faraday's law) which induces and electric field (and current) in the bulk plasma. The coil and plasma are seperated by a dielectric material, typically quartz. Heating of electrons is more effective in H-mode since they respond twice per RF cycle to the field whereas in E-mode heating of electrons happens only once per RF cycle due to the capacitive coupling. Hence the energy transfer to the electrons is more effective for H-mode. Compared to E-mode, H-mode has high plasma density, typically between 10^{11} and 10^{12} cm^{-3}, and hence higher ion and reactive species densities. Also, the ion flux and reactive species densities will be higher in this mode. The energy of the ions bombarding a sample are

generally lower in ICPs than in CCPS, because the sheath voltages in ICPs are lower than in CCPs. For thin film deposition we require a high-density plasma with relatively low ion energies (to avoid sputtering of the newly formed films). Hence, the choice for an ICP as the electrically-produced plasma in our PE-PLD technique was made.

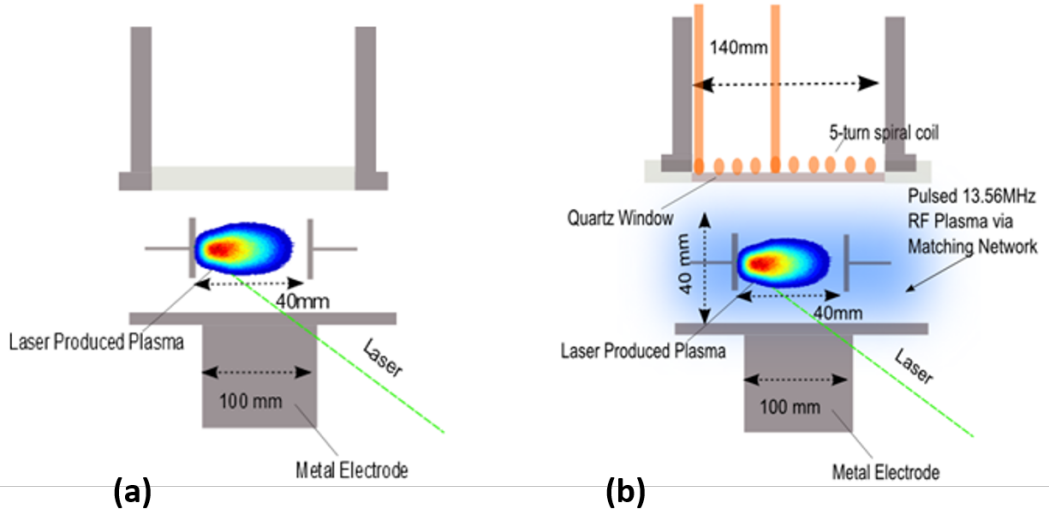

Figure 4.6: Comparison of (a) standard PLD and (b) Plasma enhanced PLD

4.4 Experimental design of PE-PLD

The experimental set-up of PE-PLD is indicated in Fig 4.6. The ICP design chosen is the GEC reference cell [65], a standardized ICP design that is widely used in the plasma processing community. This means it is a plasma that is well characterised and well understood, taking away the need to separately charactise the ICP source before incorporating it in our PE-PLD set-up. Fig 4.6 also shows the differences between the conventional PLD and the GEC-reference-cell-incorporated PE-PLD set-up. In this set-up, a 5-turn copper coil, as shown in figure 4.7, is used as top electrode. The coil is separated from the plasma using a 2.54 cm thick quartz window.

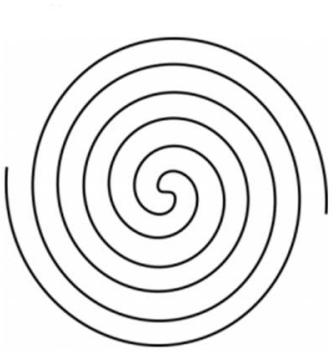

Figure 4.7: Antenna set-up

The bottom electrode and substrate holder were grounded. The distance between bottom electrode and quartz window is 40 mm. The bottom electrode is 165 mm in diameter and made of stainless steel. The RF coil is connected to a 13.56 MHz power supply (Ceasar 1330 RF generator), via an impedance matching network (Meiden made japan). The RF power supply is operated in a pulsed mode (duty cycle of 10% **on** and 90% **off**) to maximise the power input during the plasma on phase, but limit the overall heating of the setup. The RF pulse is synchronised with the laser pulse using a delay generator (Stanford research system DG535).

The target and substrate are kept in the centre of the two electrodes. The rest of the set-up is the same as in the standard PLD setup, described in section 4.1.1. For diagnostic purposes, the light emission from the plasma is focused through a lens which is at a 45^0 angle to the laser beam, onto a 0.6mm diameter optical fibre, connected to a spectrograph (Princeton 320 PI) and ICCD camera (Princeton PI-MAX). This system enables time- and space-resolved optical emission spectroscopy of both the plasma plume and the background ICP. A mass flow controller is used to control the oxygen flow into the chamber. A pressure between 4Pa and 25Pa of oxygen gas used for all PE-PLD experiments as well as for the spectroscopic studies.

4.5 Potential advantages of PE-PLD

The main potential advantages that the PE-PLD technique can offer are:

(1) The target is a pure metal, not a metal oxide target. Not only are these targets cheaper, but they are also much easier to ablate due to a lower melting temperature. This means that a lower laser power is needed, reducing the requirements for the laser used.

(2) Having all the oxygen being delivered by the ICP provides a far greater range of stoichiometry control. I.e. stoichiometry can be varied from CuO all the way to Cu_2O (and beyond) using the same Cu target, but only changing the ICP settings.

(3) Unlike traditional PLD, there is no substrate heating or post-annealing needed. The energy needed for good thin film formation is provided by the ICP instead of external heating.

4.6 Limitations of PE-PLD

Limitations that the PE-PLD technique will have are:

(1) Added complexity, both in experimental hardware (ICP setup) as well as increased operational parameters (ICP settings as well as laser settings).

(2) The ICP will constantly interact with the target, potentially causing target poisoning (as known from magnetron sputtering).

(3) The interaction between the plasma plume and the background ICP is poorly understood, adding complexity to the process.

The PLD plume is indeed expected to influence the ICP discharge during the deposition. That is metal atoms and ions from the PLD plume will interact with the ICP discharge creating metal-oxide molecules. Furthermore, energetic electrons from the ICP can excite the metal atoms/ions, resulting in additional light emission. The exact details of this interaction is difficult to quantify without a detailed study into the plasma chemistry for which a link between the two models, POLLUX and HPEM, is needed. This is beyond the scope of this thesis. However, it is important to note that for the deposition these effects are expected to be of minor importance. I.e. the time between laser pulses is 100 ms, which means that the ICP has some time to "recover", through gas flow, and become a mostly oxygen plasma again, certainly in the path of the new plume

Chapter 5

Thin film characterisation techniques

5.1 Introduction

Thin film characterisation techniques are used to investigate the different properties of thin films. This chapter is mainly focused on the principles and design of the X-Ray Diffraction (XRD), Scanning Electron Microscope (SEM) and four point probe which are used to understand the phase identification, surface image, stoichiometry of the thin film and electrical properties of the thin film.

5.2 X-Ray Diffraction (XRD)

Since the discovery of X-rays by Röntgen in 1895, X-rays have been widely used in medical [66] and material science applications [67]. X-rays are produced when fast moving electrons from a hot cathode hits a heavy target metal. X-rays cover the range of electromagnetic radiation between $\sim$ 0.01-10nm which is shorter than ultraviolet light. Within this range

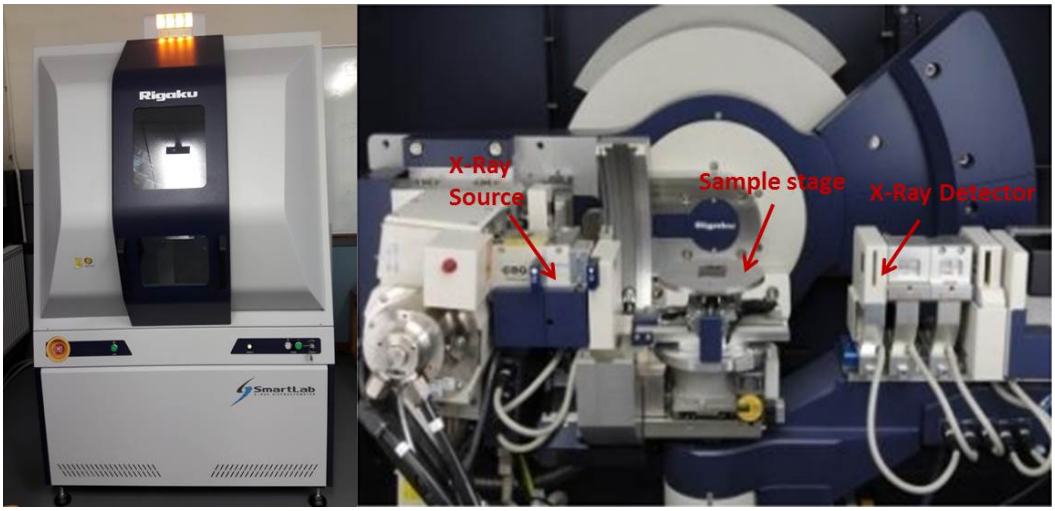

Figure 5.1: Schematic of XRD instrumental set-up

($\sim$ 0.01-10nm) a further classified into soft X-rays (0.6-10nm) and hard X-rays (0.01-0.6nm) can be made. Since soft x-rays are in the range of longer wavelength they have low energy, hence they are mostly used to take image of bones and organs [66]. Whereas, hard x-rays, due its shorter wavelength and high energy, are able to penetrate through small spacings in the unit cell. By combining the physics of x-rays and crystal orientation of the materials von Laue put forward the phenomenon of X-ray diffraction in 1912 [68].

Von Laue attempted his first X-ray diffraction experiment on copper sulfate crystal. and a diffracted x-ray pattern on a photographic plate was evidence for a regular arrangement of atoms in the crystal. Therefore, this idea of diffraction of x-rays in a regular pattern, became a pioneering idea for crystallographers to study and understand the atomic arrangement in the crystal. Figure (5.1) shows photographs of the x-ray diffraction machine used in this thesis.

Later in 1912, Idea of Von Laue's idea of x-ray diffraction gathered interest from W.H.Bragg and his son W.L.Bragg and they further simplified Von Laue mathematical expressions to study the structure of NaCl, KCl, KBr, KI [68]. Furthermore, the simplified mathematical form, now know as Bragg's law, can be used to estimate several crystal parameters. Bragg's law will be discussed in some detail in the next section.

5.2.1 Bragg's law

Figure 5.2 illustrates the general concept of Bragg reflection. W.H.Bragg and W.L.Bragg derived an expression for x-ray diffraction of crystals, based on the wavelength of the x-rays and atoms in the crystal plane. When x-rays pass through a crystal plane where the atoms positions are periodically arranged, they are scattered. x-rays scattered from many atoms can constructively interfere to get a diffracted beam in a particular orientation. In all other directions, there will be destructive interference, meaning there is no diffraction beam in that direction.

The shape of the diffraction pattern can give information about the crystal structure of the the material under study. To understand the link between an observed diffraction pattern and the crystal structure, we consider figure 5.2. Here, we consider n crystal planes parallel to the surface, with a distance d (interplanar spacing) between them.

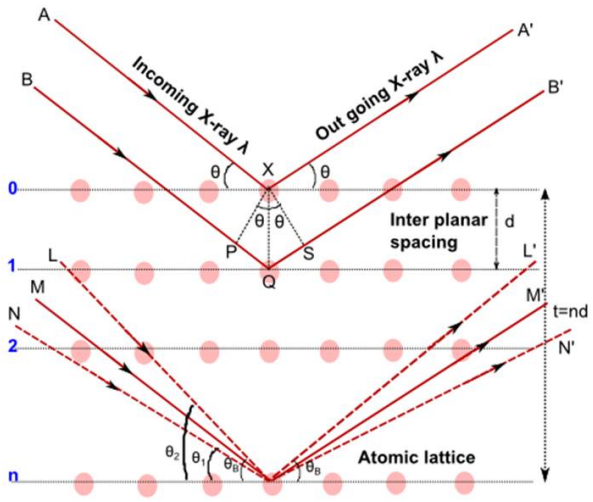

Figure 5.2: Bragg's diffraction on the crystal [68].

A monochromatic X-ray beam with wavelength (λ) is incident on to the crystal. When an X-ray hits an atom in the crystal it is reflected at angle θ. Rays A and B show two examples of reflections. The reflected rays A' and B' have a path difference of PQ + QS

constructive interference occurs. Figure (5.2), shows that rays A and B are scattered by the X and Q atoms and the path difference for the 0 and 1 plane is given as,

$$PQ + QS = dsin\theta + dsin\theta \tag{5.1}$$

Constructive interference occurs when the path difference is an integer number of wavelength, nλ. Rearranging the equation (5.1), results in

$$\boxed{n\lambda = 2dsin\theta} \tag{5.2}$$

The equation 5.2 is known as Bragg's law which is the necessary criteria for diffraction to occur. By changing the angle θ, it is possible to determine d for an unknown crystal (as long as λ of the x-rays is known). In practice, rather than moving x-ray source and detector the

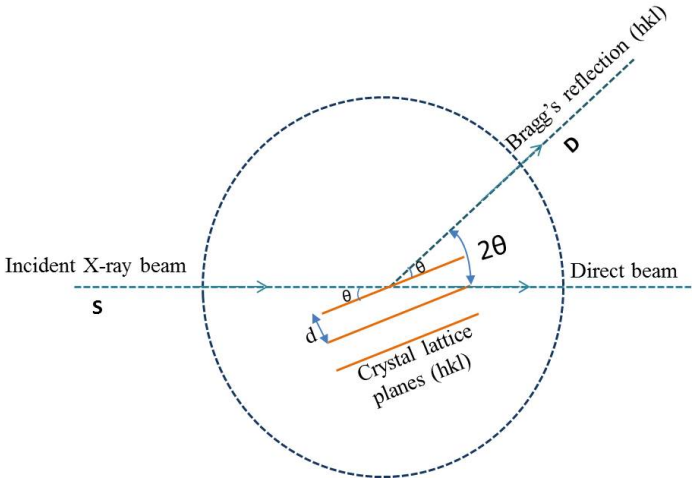

Figure 5.3: Sample stage in X-ray spectrometer

sample is rotated to achieve the necessary angle of scanning and we use Bragg's law in XRD to determine an unknown crystal structure. E.g. by measuring angles θ for which there is a maximum diffraction, d can be determined.

Based on the atoms present in the unit cell the diffraction angle for a set of planes will be different. In order to determine the diffraction angle for any crystal system having a set

of planes, we use Bragg's law (equation 5.2), In equation 5.2, d is an interplanar distance and it is different for different crystal system. consider a cubic crystal,

$$d^2 = \frac{a^2}{(h^2 + k^2 + l^2)} \tag{5.3}$$

Here, (h,k,l) are the miller indices and it represents planes in the lattice which means it does not represent one particular plane instead it a represents set of parallel planes which corresponds to the crystal plane direction. Substituting equation 7.3 in Bragg's law (equation 7.2) we get,

$$sin^2\theta = \frac{\lambda^2}{4a^2}(h^2 + k^2 + l^2) \tag{5.4}$$

Therefore for Miller indices of e.g. (1,1,1) the diffraction angle of a cubic system of Cu_2O is,

$$sin^2\theta = \frac{3\lambda^2}{4a^2} \tag{5.5}$$

The lattice parameter for Cu_2O is a= 4.2520$\mathring{A}$, therefore d is 2.454$\mathring{A}$ and $\sin\theta_{111} = 1.54\mathring{A}/2(2.454\mathring{A})$= 0.3137, θ_{111}= $\sin^{-1}(0.3137)$=18.287 and $2\theta_{111}$=36.573. This means that a peak at 36.573 degrees will be observed as a result of the (111) phase of Cu_2O.

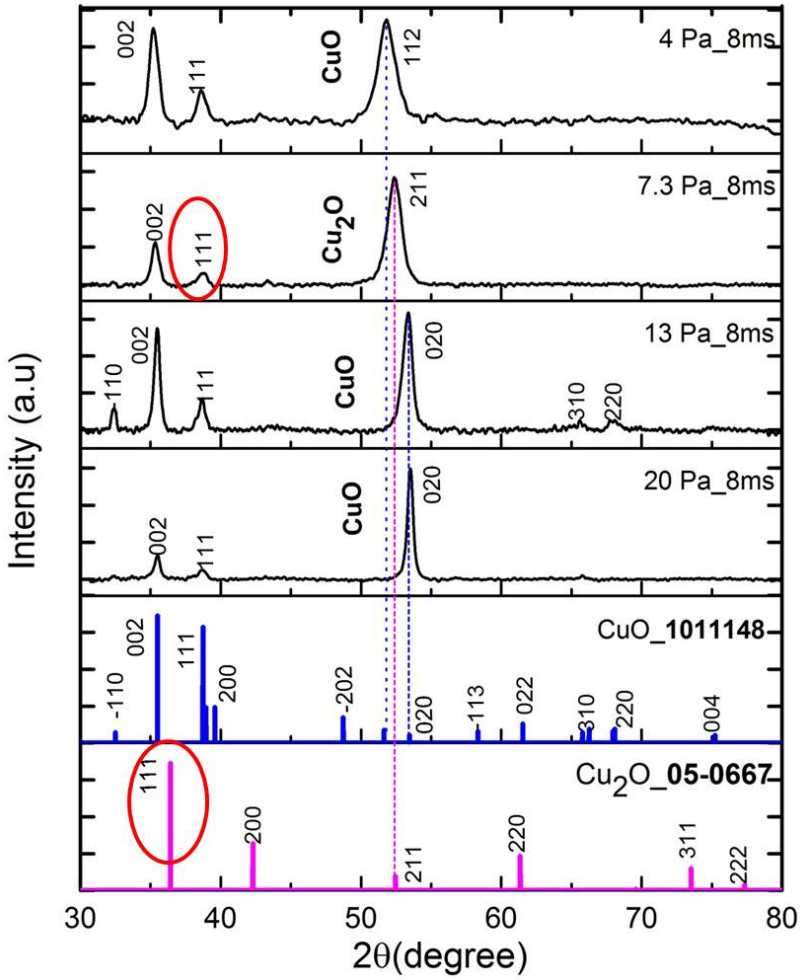

Figure 5.4: Cu_2O showing (111) plane in both JCPDS and experimental results. The calculation for 2θ value is shown above

Similarly for orthorhombic system,

$$sin^2\theta = \frac{\lambda^2(h^2+k^2+l^2)}{4(a^2+b^2+c^2)} \tag{5.6}$$

As mentioned earlier (h,k,l) are miller indices, λ is the wavelength of X-ray ($\mathring{A}$), (a,b,c) are the lattice constant.

5.2.2 Crystal size calculation

Another important parameter we can get from XRD is crystal size. If the material is amorphous we get a broadened peak due to the missing long range order in the material. Figure 7.5 schematically shows this effect. The first image is a broadened peak with a FWHM of ($2\theta_1$ - $2\theta_2$) as a result of a decrease in crystal size compared to a perfectly crystalline sample in the second image.

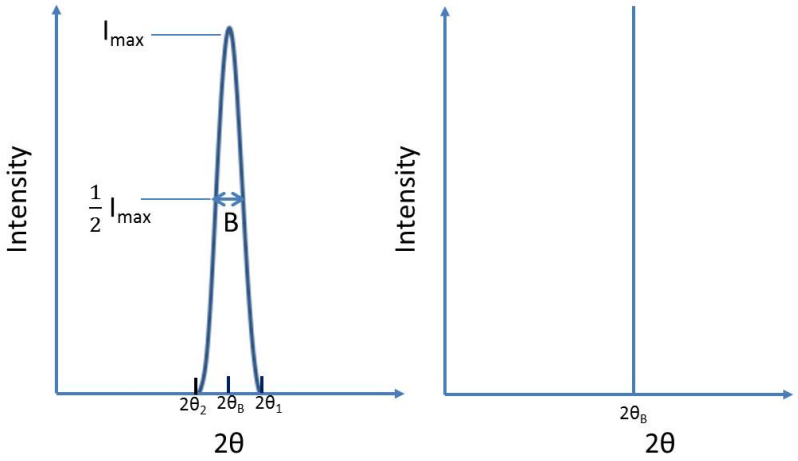

Figure 5.5: Diffraction pattern for change in crystal size

Therefore to derive the crystal size formula, let us consider a crystal system having thickness ˜t″and ˜n″planes for the atoms in the crystal and θ the Bragg's angle. The crystal size will be considered to have a spherical in shape. For example, in the figure (5.2), let us consider the n^{th} plane, where the x-rays arrive from two different diffraction angles θ_1 and θ_2 (which are named as ray L and ray N) for which the obtained reflected angles are either higher($(n+1)\lambda$ or lower($(n-1)\lambda$ than the n^{th} plane.

$$\beta_t = \frac{1}{2}(2\theta_1 - 2\theta_2) \tag{5.7}$$

In the equation (5.7), β is the FWHM of the diffraction peak where at $2\theta_1$ and $2\theta_2$ are the broadening angles. Rewriting Bragg's law equation (5.2) for two different angle and t=nd,

let us consider n=1 and therefore d=t. Substituting this in equation (5.2) we get,

$$(n+1)\lambda = 2t\ sin\theta_1 \tag{5.8}$$

$$(n-1)\lambda = 2t\ sin\theta_2 \tag{5.9}$$

and the difference in the two equation gives,

$$t(sin\theta_1 - sin\theta_2) = \lambda \tag{5.10}$$

$$sin\theta_1 - sin\theta_2 = 2cos\left(\frac{\theta_1+\theta_2}{2}\right)sin\left(\frac{\theta_1-\theta_2}{2}\right) \tag{5.11}$$

substituting equation (5.11) in equation (5.10) gives,

$$2t\ cos\left(\frac{\theta_1+\theta_2}{2}\right)sin\left(\frac{\theta_1-\theta_2}{2}\right) = \lambda \tag{5.12}$$

For most cases θ_1 and θ_2 are close to θ_B,

$$\theta_1 + \theta_2 \approx 2\theta_B \tag{5.13}$$

Similarly, making the approximations $sin\theta \approx \theta$,

$$sin\left(\frac{\theta_1-\theta_2}{2}\right) \approx \left(\frac{\theta_1-\theta_2}{2}\right) \tag{5.14}$$

gives,

$$2t\left(\frac{\theta_1-\theta_2}{2}\right)cos\theta_B = \lambda \tag{5.15}$$

$$t = \frac{\lambda}{\beta_t\ cos\theta_B} \tag{5.16}$$

where the (equation5.17) is the simple Scherrer equation, which gives the crystal size assuming there are no other sources of broadening. To take account of the geometry of the crystal,

(equation5.17) is multiplied by a factor K. This factor varies between 1.0 and 0.89, where 0.89 is for a perfectly spherical crystal. This leads to the following equation for crystal size:

$$\boxed{t = \frac{K\lambda}{\beta_t \ cos\theta_B}} \tag{5.17}$$

5.3 Scanning electron microscope (SEM)

Scanning electron microscope (SEM) is an imaging technique where a beam of electrons acts as a probe that is scanned along the sample. The incident electron release secondary electrons from the sample which are collected by the secondary electron detector and are further transformed into an image.

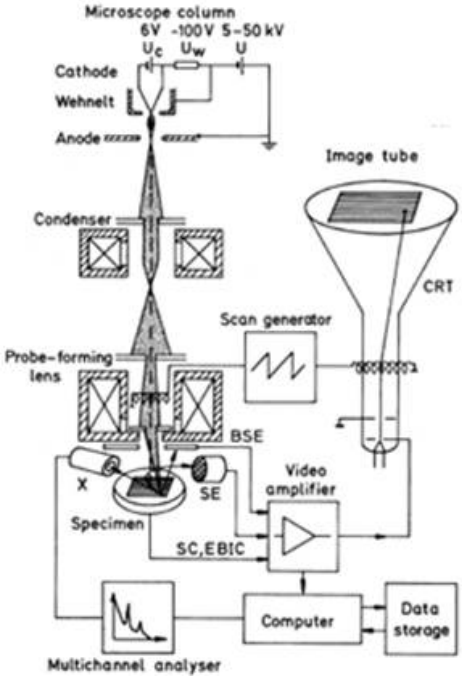

Figure 5.6: Construction of SEM [69]

The first SEM was built by Knoll in 1935. Because no magnifying lens was used in this design, the magnification was limited to 100 μm. This has been improved over time and modern SEMs can get down to a resolution of about 0.5 nm.

Fig (5.6) a schematic of the components of an SEM. Electrons from a cathode (electron gun: thermionic, Schottky or field emission) are generated and move towards an anode by applying a voltage difference of 1-30 kV depending on sample condition. The electrons from the electron gun are focused using electrodes which are placed between the cathode and anode. The electron beam is further focused using a condenser lens and an objective lens which are right below the electron gun. These lenses play a major role in narrowing the diameter of the electron beam to 1-10nm. The electron current that is focussed onto the sample is in the order of $10^{-9} - 10^{-12}$A [69] allowing high resolution image. Generally, voltages below 5 kV is considered as a low beam energy which is mostly used for biological and less conducting sample to avoid charge accumulation and sample damage. High beam energy, coupled with EDX, can be used to quantify the elements present in the sample. In the below section, the principles of the SEM and the different imaging modes will be discussed.

5.3.1 Principles and imaging modes in scanning electron microscopy

When a beam of electrons penetrates into the sample, depending on electron energy, atomic number and density of the atoms in the sample, several elastic and inelastic scattering process take place. The signals collected from these scattering processes are used to form images. Based on the signals collected, the imaging modes of SEM are classified into five modes: 1. Secondary electron (SE), 2. Backscatter electron imaging (BSE), 3. Electron beam induced current (EBIC), 4. Cathodoluminescence (CL), and 5. Auger electron (AE). The incident electron beam penetrates the sample and interacts in a volume determined by the electron energy. Figure (5.7), shows the size of the interaction volumes for different imaging mode. They are pear shaped since the electron beam slowly penetrates side ways due to the scattering effects. Of these techniques, SE and BSE are commonly used.

The SE mode utilises those electrons emitted from the specimen whose energy is less than 50eV. Most of the emitted secondary electrons are produced within the first few nm of

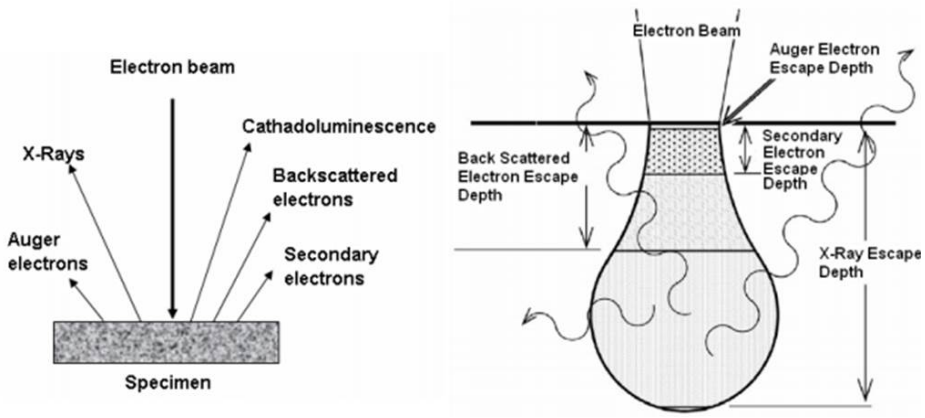

Figure 5.7: SEM depth and information profile (`http://www.jeol.com/`)

the surface, hence this mode can provide high spatial depth resolution images. Usually, this imaging mode is used to get the topographical information of a specimen.

In BSE mode, the incoming electrons that are scattered through a large angle, due to collisions near the nucleus of an atom, are used for imaging purposes. These backscattered electrons typically have energies greater than 50 eV. The higher the atomic number of the sample the more likely it is to get backscattered electrons and therefore a better contrast in the image. Since these backscattered electrons are produced from slightly deeper inside the specimen, the image resolution is lower than it is in SE mode and this clearly seen in the figure (5.8).

Unlike SE and BSE mode, the EBIC imaging mode utilizes the electron-hole pair generated in the specimen for imaging purpose. In this mode, an electric field is applied to separate the electrons and holes before their recombination, forming a p-n junction. The formation of this p-n junction induces a current to flow between anode (electron) and cathode (hole). This current flow depends on the conductivity of the specimen and the lifetime of electrons and holes.

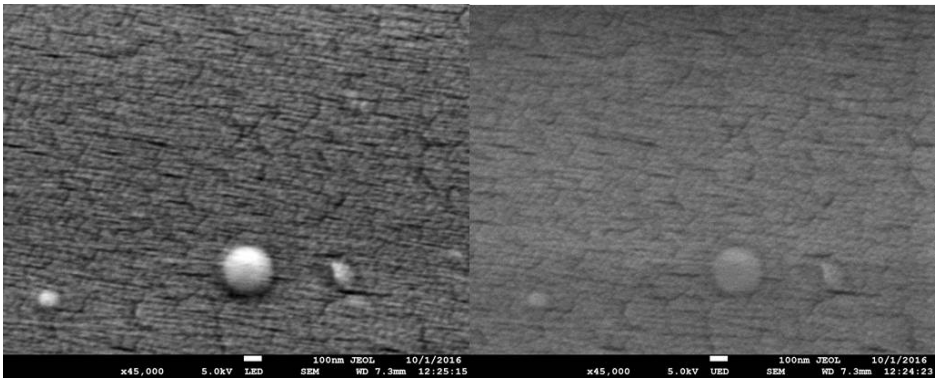

Figure 5.8: SE and BSE modes of image for copper thin film deposited at 13 Pa

Similar to EBIC mode, the CL mode also uses the generated electron-hole pair for imaging purpose. However, in this mode the recombination of electron-hole pair is not prevented by applying an electric field, as applied in the EBIC mode. On the contrary, the electron-hole pair recombination, which emits light is detected, The wavelength of the emitted light due to this recombination depends on the bandgap energy of the specimen. Therefore, this mode reveals the composition of the material along with the information on defects which degrade the radiative properties.

Auger electron imaging is an SEM imaging mode in which Auger electrons are emitted from the few atomic layers closest to surface, Therefore, this mode is used to provide information about surface chemistry. Generally, during imaging only a few Auger electrons are emitted. Since there are only very few Auger electrons are emitted meaning signals are low and detection requires very sensitive instruments.

5.4 Four point probe technique

The resistivity of a material is an important property for applications. It is known to depend on multiple factors such as temperature, defects dopants. Measuring the resistivity of the material is therefore important and the four-point probe is a widely used technique. In 1915,

Wenner [70] [71] was the first person to demonstrate this technique to calculate the earth's resistivity.

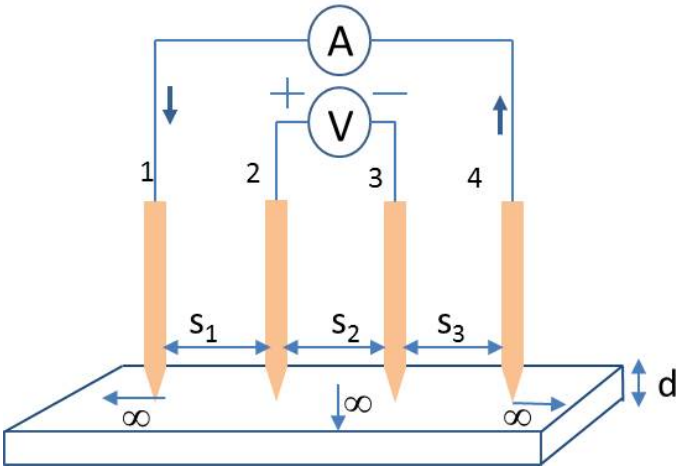

Figure 5.9: Schematic of four point probe used to measure the sheet resistance

Later in 1954, Valdes [72] used the same principle to calculate the sheet resistance of a semiconductor wafer. Advantages of the four point probe over simple voltage (V) and current (I) measurement is the four point probe method not only measures the resistivity but also gives the sheet resistance of thin films. Figure (5.9) shows the schematic of the four point probe technique. In this technique, four thin probes that are equally spaced at s_1, s_2 and s_3 touch the sample surface. A current flows between the two outer probes (1 and 4) and the inner probes 2,3 measure the potential difference as shown in the figure (5.9).

In order to understand the mathematical derivation for the four point probe method consider a single probe interaction on the surface. Figure (5.10) shows the current flow for a single probe. The current I entering the surface is assumed to distribute homogeneously in a semi-sphere from a single point. The current density in the sample in point P is therefore given by J = $\frac{I}{2\pi r^2}$, where r is the distance from P to the point were the probe tip touches. The electric field in the sample is described by E = -$\frac{dV}{dr}$= $J\rho$ where V is the voltage difference between P and the tip of the probe and ρ is the resistivity of the sample, which will be assumed to be homogeneous. The voltage for the point P is given by,

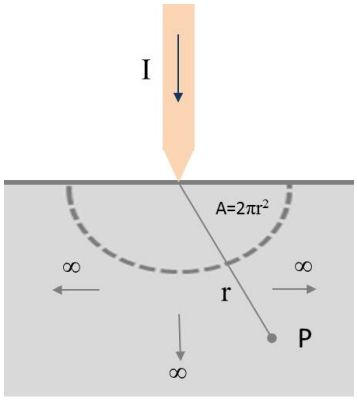

Figure 5.10: current flow for one point probe [71]

$$E = \frac{dV}{dr} = -\rho\left(\frac{I}{2\pi r^2}\right) \tag{5.18}$$

$$V = \int_0^r \left(\frac{dV}{dr}\right) = \rho\left(\frac{I}{2\pi r}\right) \tag{5.19}$$

Considering this in the four point probe, the spacing of the probes (s_1,s_2,s_3) is taken into account, and the voltage at probe 2 (see Fig: 5.9) is:

$$V_2 = \frac{I\rho}{2\pi}\left(\frac{1}{s_1} - \frac{1}{s_2 + s_3}\right) \tag{5.20}$$

Similarly at probe 3,

$$V_3 = \frac{I\rho}{2\pi}\left(\frac{1}{s_1 + s_2} - \frac{1}{s_3}\right) \tag{5.21}$$

Therefore, the potential difference (V) between probe 2 and 3 are,

$$V = \frac{I\rho}{2\pi}\left[\left(\frac{1}{s_1} - \frac{1}{s_2 + s_3}\right) - \left(\frac{1}{s_1 + s_2} - \frac{1}{s_3}\right)\right] \tag{5.22}$$

Since the probes are equally spaced, $s_1 = s_2 = s_3 = \mathrm{s}$, then equation (5.22) becomes,

$$R_s = \left(\frac{V}{I}\right) \times 2\pi s \tag{5.23}$$

The equation (5.23), applies only for the semi-infinite case and does not apply directly for

thin films. However for thin films, one of the dimensions is finite and this is corrected by the factor (F) for finite geometries

$$\rho = 2\pi s \times F\left(\frac{V}{I}\right) \tag{5.24}$$

This correction factor was calculated by Albers and Berkowitz in 1985 [73] for film thicknesses less than the prove spacing:

$$F = \frac{\pi}{ln(2)} \times d \tag{5.25}$$

probe spacing (d≤s/2). For thicknesses greater than probe spacing, the correction factor is not taken into account and the infinite materials are assumed.

Therefore, based on the correction factor for the films equation (5.24) becomes,

$$R_s = 4.532 \times \frac{V}{I} \tag{5.26}$$

Therefore, by measuring the change in voltage across the inner probe and the current applied to the two outer probe, the sheet resistance of the thin film can be calculated. In my case, in order to calculate the electrical resistivity (Q) of the thin film, I measured the sheet resistance from the four point probe and then multiply with the fillm thickness (determined by AFM) to get resistivity of the thin films, as described by:

$$\boxed{\textit{Electrical resistivity (Q)} = R_s \times d} \tag{5.27}$$

Chapter 6

POLLUX and HPEM simulations

6.1 Introduction to the models

In order to investigate the feasibility of the PE-PLD technique, I performed a modelling investigation of both the laser ablation process of a Cu target and the plasma properties of the ICP discharge in oxygen. For the PE-PLD process to work, the plasma plume density at the substrate needs to be roughly similar to the density of relevant species in the ICP. This because we need the plume to interact with the ICP plasma to make sure the Cu oxidises and deposits as copper oxide. If the density of the Cu plume is many orders of magnitude higher, this interaction is unlikely to happen, or at least will be insufficient for full oxidation of the plume, leading to non-stoichiometric copper oxide films.

A full model of the PE-PLD process is challenging and currently not available since it involves many different physical processes and time scales. Developing such a model is beyond the scope of this thesis. In this chapter the laser ablation process and the ICP plasma are modelled separately and the results compared to investigate the feasibility of the PE-PLD deposition process. For the modelling of the laser-target interactions we use the 2D hydrodynamics code POLLUX, a code that has been developed at the University

of York over the last few decades. Full details of the code can be found in [74], a brief description of the main features is presented in section 5.1.1. This code will be used to study the laser-produced copper plasma.

Secondly, we use the 2D Hybrid code HPEM to calculate the plasma properties of the inductively coupled RF oxygen plasma. This code has been developed by Kushner et al and a detailed description of the code can be found in [75]. A brief overview of the main idea of the code is presented in section 5.1.2.

6.1.1 Description of POLLUX

Even though the laser ablation process is conceptually simple, there are many different physical processes that need to be taken into account. The first is that during the ablation process, the solid target absorbs the laser energy and changes from solid to liquid and from liquid to gas state before becoming a plasma. This involves energy transport through conduction and radiation, resulting in phase changes in the target material (at non-ambient pressures) as well as dissociation and ionisation and the formation of shock waves [74].

The code that is used to describe the laser ablation of a copper target by a high-power nanosecond laser is POLLUX [76]. It is a 2D Euler a hydrodynamic code that was written by Pert et al [74] at the University of York. This code solves the three first-order quasilinear partial differential equation of hydrodynamics [1] by utilizing the flux corrected transport (FCT) algorithm developed by Boris and Book [76] [77]. The flux corrected transport algorithm in the code is used for solving the gas dynamics using the continuity equation and it is particularly used for solving the laser plasma interaction, vaporization and heat transport into the solid when shock waves are formed [76].

In order to describe the thermodynamic properties of the target material, a combination of Chart-D Equation-Of-State (EOS) [78] and a Thomas-Fermi ionisation model [79] are

included. The Chart-D EOS (developed by Sandia National Laboratories [78]) is used to calculate the phase changes during the ablation process. Four types of phase boundaries are included in this code, (i.e solid-liquid, liquid-vapour, solid-vapour and solid-solid transitions). Absorption of radiation in the plasma plume is by inverse bremsstrahlung. A Thomas-Fermi model is used to estimate the ionisation of the plasma. This model is particularly applicable for high density states. Whereas, for low density, by excluding the detailed shell structure validates this model [76]. Furthermore, a ray tracing module takes into account the refraction of the laser beam by the plasma that is formed.

The code considers a cylindrically symmetric geometry, where the target surface is aligned perpendicular to the laser direction. The laser pulse is modelled as a Gaussian beam, i.e. a Gaussian spatial and temporal profile where the FWHM of beam diameter and duration can be set by the user.

6.1.2 Description of HPEM

This model calculates the plasma properties in three steps [80]. First, electromagnetic fields within the discharge volume are calculated by solving the Maxwell equation. Next, based on these electromagnetic fields, the electron density, electron temperature, electron energy distribution function, electron impact reaction rates are calculated by a Monte Carlo module. Finally, plasma chemistry reactions in the reactor volume are determined from the reaction rates, the continuity equation and the local electric field strength, determined from Poisson's equation. This gives a map of the densities of the different plasma species. This is compared to the initial densities. When there is a discrepancy, the initial densities are modified and the same loop is repeated until convergence is reached.

An important part of running this model is the plasma chemistry and this chemistry was constructed based on Tinck and Bogaerts [80] and further modified by Gibson et al [81]. In our case we include electrons and seven different oxygen species in this model.

i.e. $O_2(X^3\Sigma_g^-)$, $O_2(a^1\Delta_g)$, $O_2(b^1\Sigma_g^+)$, $O(^3P)$, $O(^1D)$, O_2^+, O^+, O^- represents ground state molecular oxygen, two excited states of molecular oxygen, ground state atomic oxygen, atomic metastable oxygen, molecular positive oxygen ions, atomic positive oxygen ions and atomic negative oxygen ions. The reaction mechanism that are included in this model are taken from [80] [81] and given in the table 6.1. Here in the table 6.1, $O_2^*(1S)$ refers to $O_2(X^3\Sigma_g^-)$, O^* refers to $O(^1D)$, O refers to $O(^3P)$, O_2^* refers to $O_2(a^1\Delta_g)$ and $O_2(b^1\Sigma_g^+)$.

Table 6.1: Reaction mechanism

No	Reaction	Rate Coefficient[a,b]	Reference
R1	$e + O_2(X^3\Sigma_g^-) \rightarrow e + O_2(X^3\Sigma_g^-)$	$f(\epsilon)$	[82] [83]
R2	$e + O_2(a^1\Delta_g) \rightarrow e + O_2(a^1\Delta_g)$	$f(\epsilon)$	[84]
R3	$e + O_2(b^1\Sigma_g^+) \rightarrow e + O_2(b^1\Sigma_g^+)$	$f(\epsilon)$	[84]
R4	$e + O(^3P) \rightarrow e + O(^3P)$	$f(\epsilon)$	[85]
R5	$e + O(^1D) \rightarrow e + O(^1D)$	$f(\epsilon)$	c
R6	$e + O_2(X^3\Sigma_g^-) \rightarrow e + O_2(a^1\Delta_g)$	$f(\epsilon)$	[82] [83]
R7	$e + O_2(X^3\Sigma_g^-) \rightarrow e + O_2(b^1\Sigma_g^+)$	$f(\epsilon)$	[82] [83]
R8	$e + O_2(a^1\Delta_g) \rightarrow e + O_2(b^1\Sigma_g^+)$	$f(\epsilon)$	[86]
R9	$e + O_2(b^1\Sigma_g^+) \rightarrow O_2(a^1\Delta_g) + e$	$f(\epsilon)$	d
R10	$e + O_2(a^1\Delta_g) \rightarrow O_2(X^3\Sigma_g^-) + e$	$f(\epsilon)$	d
R11	$e + O_2(b^1\Sigma_g^+) \rightarrow O_2(X^3\Sigma_g^-) + e$	$f(\epsilon)$	d
R12	$e + O_2(X^3\Sigma_g^-) \rightarrow O_2^+ + e + e$	$f(\epsilon)$	[82] [83]
R13	$e + O_2(a^1\Delta_g) \rightarrow O_2^+ + e + e$	$f(\epsilon)$	e
R14	$e + O_2(b^1\Sigma_g^+) \rightarrow O_2^+ + e + e$	$f(\epsilon)$	e
R15	$e + O_2(X^3\Sigma_g^-) \rightarrow O(^3P) + O^-$	$f(\epsilon)$	[82] [83]
R16	$e + O_2(a^1\Delta_g) \rightarrow O(^3P) + O^-$	$f(\epsilon)$	[87]
R17	$e + O_2(b^1\Sigma_g^+) \rightarrow O(^3P) + O^-$	$f(\epsilon)$	f
R18	$e + O_2(X^3\Sigma_g^-) \rightarrow O(^3P) + O(^3P) + e$	$f(\epsilon)$	[82] [83]
R19	$e + O_2(a^1\Delta_g) \rightarrow O(^3P) + O(^3P) + e$	$f(\epsilon)$	e
R20	$e + O_2(b^1\Sigma_g^+) \rightarrow O(^3P) + O(^3P) + e$	$f(\epsilon)$	e
R21	$e + O_2(X^3\Sigma_g^-) \rightarrow O(^3P) + O(^1D) + e$	$f(\epsilon)$	[82] [83]
R22	$e + O_2(a^1\Delta_g) \rightarrow O(^3P) + O(^1D) + e$	$f(\epsilon)$	e
R23	$e + O_2(b^1\Sigma_g^+) \rightarrow O(^3P) + O(^1D) + e$	$f(\epsilon)$	e
R24	$e + O(^3P) \rightarrow e + O(^1D)$	$f(\epsilon)$	[88]
R25	$e + O(^1D) \rightarrow e + O(^3P)$	$f(\epsilon)$	d
R26	$e + O(^3P) \rightarrow e + O^+ + e + e$	$f(\epsilon)$	[88]
R27	$e + O(^1D) \rightarrow e + O^+ + e + e$	$f(\epsilon)$	e

No	Reaction	Rate Coefficient[a,b]	Reference
R28	$e + O^- \rightarrow O(^3P) + e + e$	$f(\epsilon)$	[89]
R29	$e + O_2^+ \rightarrow O(^3P) + O(^3P)$	$3.72 \times 10^{-9}\ T_e^- 0.7$	[90] [91]
R30	$e + O_2^+ \rightarrow O(^3P) + O(^1D)$	$7.44 \times 10^{-9}\ T_e^- 0.7$	[90] [91]
R31	$e + O_2^+ \rightarrow O(^1D) + O(^1D)$	$7.44 \times 10^{-9}\ T_e^- 0.7$	[90] [91]
R32	$O_2^+ + O^- \rightarrow O_2(X^3\Sigma_g^-) + O(^3P)$	$2.60 \times 10^{-8}\ T_0^- 0.44$	[92]
R33	$O_2^+ + O^- \rightarrow O(^3P) + O(^3P) + O(^3P)$	$2.60 \times 10^{-8}\ T_0^- 0.44$	[92]
R34	$O^+ + O^- \rightarrow O(^3P) + O(^3P)$	$4.00 \times 10^{-8}\ T_0^- 0.43$	[92]
R35	$O(^3P) + O^- \rightarrow O_2(X^3\Sigma_g^-) + e$	$1.50 \times 10^{-10}\ T_0^- 1.30$	[93]
R36	$O_2(a^1\Delta_g) + O^- \rightarrow O_2(X^3\Sigma_g^-) + O(^3P) + e$	1.10×10^{-10}	[94]
R37	$O_2(b^1\Sigma_g^+) + O^- \rightarrow O_2(X^3\Sigma_g^-) + O(^3P) + e$	6.90×10^{-10}	[95]
R38	$O^+ + O_2(X^3\Sigma_g^-) \rightarrow O_2^+ + O(^3P)$	2.30×10^{-11}	[96]
R39	$O^+ + O_2(a^1\Delta_g) \rightarrow O_2^+ + O(^3P)$	1.00×10^{-11}	[96]
R40	$O^+ + O_2(b^1\Sigma_g^+) \rightarrow O_2^+ + O(^3P)$	1.00×10^{-11}	h
R41	$O_2^+ + O_2(X^3\Sigma_g^-) \rightarrow O_2(X^3\Sigma_g^-) + O_2^+$	4.00×10^{-10}	[97]
R42	$O_2^+ + O_2(a^1\Delta_g) \rightarrow O_2(X^3\Sigma_g^-) + O_2^+$	2.00×10^{-10}	i
R43	$O_2^+ + O_2(b^1\Sigma_g^+) \rightarrow O_2(X^3\Sigma_g^-) + O_2^+$	2.00×10^{-10}	i
R44	$O(^3P) + O(^1D) \rightarrow O(^3P) + O(^3P)$	8.00×10^{-12}	[73]
R45	$O_2(X^3\Sigma_g^-) + O(^1D) \rightarrow O_2(X^3\Sigma_g^-) + O(^3P)$	$0.32 \times 10^{-11}\ \exp(67/T_g)$	[98] [99] [100]
R46	$O_2(X^3\Sigma_g^-) + O(^1D) \rightarrow O_2(a^1\Delta_g) + O(^3P)$	$0.32 \times 10^{-11}\ \exp(67/T_g)$	[98] [99] [100]
R47	$O_2(X^3\Sigma_g^-) + O(^1D) \rightarrow O_2(b^1\Sigma_g^+) + O(^3P)$	$2.56 \times 10^{-11}\ \exp(67/T_g)$	[98] [99] [100]

No	Reaction	Rate Coefficient[a,b]	Reference
R48	$O_2(a^1\Delta_g) + O(^3P) \rightarrow O_2(X^3\Sigma_g^-) + O(^3P)$	2.00×10^{-16}	[101] [102]
R49	$O_2(a^1\Delta_g) + O_2(X^3\Sigma_g^-) \rightarrow O_2(X^3\Sigma_g^-) + O_2(X^3\Sigma_g^-)$	3.60×10^{-18} exp (-220/T_g)	[102]
R50	$O_2(a^1\Delta_g) + O_2(a^1\Delta_g) \rightarrow O_2(X^3\Sigma_g^-) + O_2(b^1\Sigma_g^+)$	1.81×10^{-18} $T_0^{0.38}$ exp (-220/T_g)	[103]
R51	$O_2(b^1\Sigma_g^+) + O(^3P) \rightarrow O_2(X^3\Sigma_g^-) + O(^3P)$	8.00×10^{-14}	[103]
R52	$O_2(b^1\Sigma_g^+) + O_2(X^3\Sigma_g^-) \rightarrow O_2(a^1\Delta_g) + O_2(X^3\Sigma_g^-)$	3.90×10^{-17}	[103]

6.2 Results and discussion

6.2.1 Laser ablation model: POLLUX

The laser pulse that is modelled here has a laser wavelength of 532 nm, pulse duration of 5 ns and focal spot radius of 0.5 mm. This leads to a laser fluence of about 3 J/cm^2 and an intensity of 6x10^8 W/cm^2, both are typical values for PLD processes. The axial velocity, electron temperature and densities for 13Pa and 20Pa background gas pressure at different time scales were calculated.

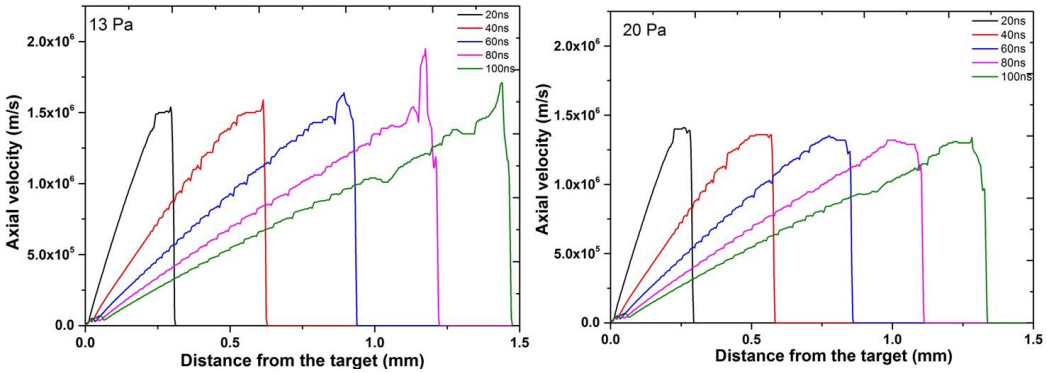

Figure 6.1: Axial velocity along the plume symmetry axis 13Pa and 20Pa from POLLUX at 6×10^8 W/cm^2

Figure 6.1 shows the axial velocity of the ablated Cu material moving away from the target surface at 13Pa and 20Pa background gas pressure between 20ns to 100ns with 20ns time steps. For 13Pa, the peak velocity is about constant around 1.5 x 10^6 m/s for all times between 20 and 100 ns. In addition, for all times, the highest velocities are found near the front of the expanding plume. Increasing the background pressure to 20 Pa leads to a similar temporal pattern, but the peak velocity is slightly lower at about 1.4x10^6 m/s, leading to a maxmium plume size of 1.33 mm at 100 ns, compared to 1.47 mm at 100 ns for 13 Pa.

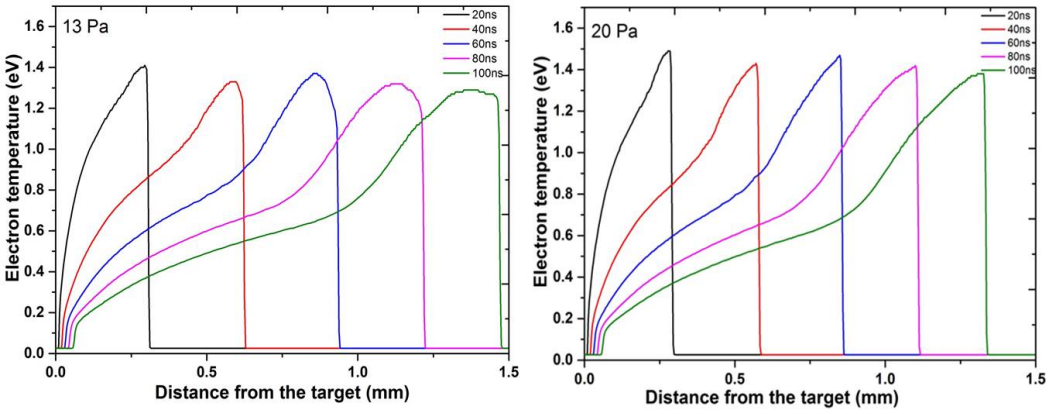

Figure 6.2: Electron temperature at 13Pa and 20Pa from POLLUX at 6×10^8 W/cm^2

Therefore, increasing the pressure, increases the life time of the plasma plume due to the

background gas compressing the plume both radially and axially. This compression effect in the expansion of the plume is similar to what has been seem experimentally by e.g. Atif Hussain et al. [104]. They experimentally showed the expansion of an Al plume between 0.1 mbar to 10 mbar, in which increasing the pressure confines the plasma plume due to the background gas effect.

Figure 6.2, shows the evolution of the electron temperature of the Cu plasma at 13Pa and 20Pa. At 13Pa, the electron temperature slowly decreases from 1.41eV to 1.29eV between 20ns to 100ns. Whereas, at 20Pa, the temperature is slightly higher and varies between 1.49eV to 1.38eV. The slight increase in temperature for 20Pa when compared to 13Pa is mainly due to the background pressure. Increasing the background pressure, compresses the plasma plume, limiting its expansion and therefore cooling, leading to higher temperatures. Compression in the plasma plume increases the particle collisions within the plasma plume which in turn increases the electron density.

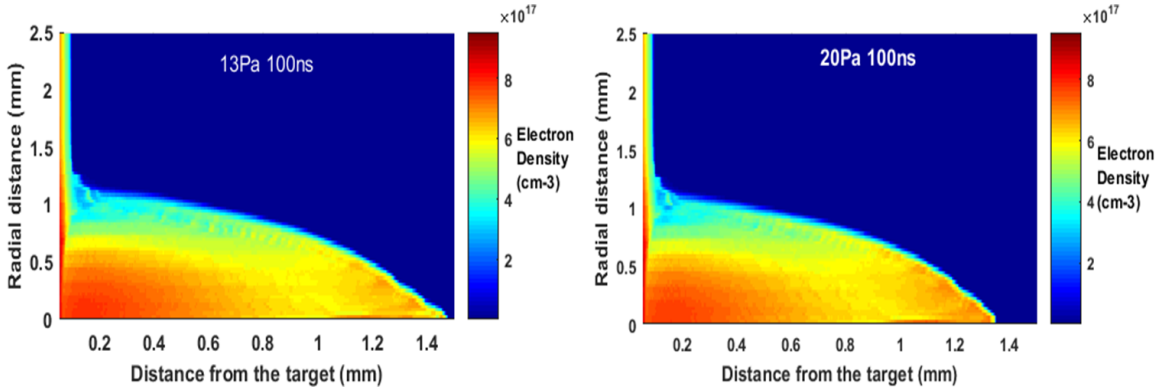

Figure 6.3: Electron density calculated from simulation at 13Pa and 20Pa at 100ns

In both cases for axial velocity and electron temperature, the background pressure influences the expansion and the temperature of the plasma plume. After 100ns, the plasma plume has expanded over at distance of 1.47mm for 13 Pa and 1.33 mm for 20 Pa. At this point, the axial velocity close to the target is close to zero. This shows that no new target

material is ejected from the target surface. In a standard PLD deposition process, the repetition rate of the laser is typically 10-50 Hz, which means that PLD is not a continuous deposition process, but rather a pulsed process. Material is only removed and deposited shortly after the laser shot, after which a relatively long period occurs during which there is no plasma. [1].

Figure 6.3 shows the 2D graph of electron density simulated at 100ns for 13Pa and 20Pa. A density of 9×10^{17} cm^{-3} is found near the front of the plume and densities of order of 2-6 $\times$ 10^{17} cm^{-3} are observed behind the expanding plume. Whereas, the densities near the target are high, however these particles have near-zero velocities which means that this material will re-solidify on the target after the laser pulse and will not take part in the deposition process on the substrate. Our simulations show that in a single laser pulse about 1×10^{17} Cu ions are formed. When this plume expands towards a substrate, about 4 cm away, the typical density at the substrate will be in the order of 10^{14} cm^{-3}. The PE-PLD process relies on an interaction between this expanding Cu plume and the oxygen background plasma. For this we need the densities of the plume, close to the substrate, to be close to the densities of reactive oxygen found in the background plasma. The next section focusses on calculating these densities.

6.2.2 Reactive oxygen plasma

Figure 6.4 shows the schematic of the modelled reactor geometry. It is following the design of the rf GEC reference cell [65]. A reactor geometry that is extensively used geometry to study the plasma properties for both experimental and modelling conditions.

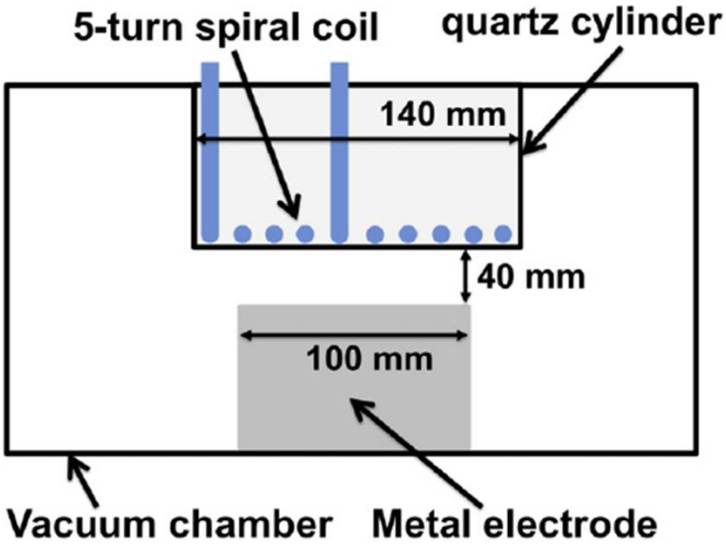

Figure 6.4: Schematic representation of the inductively coupled plasma. The design is following the standardised GEC reference cell [1]

Here in this geometry, the top electrode is made up of a 5-turn copper coil which is separated from the vacuum vessel by a quartz window. The bottom electrode is a metal electrode inside the vacuum vessel. The distance between the quartz window and bottom electrode is 40 mm. Electrical power from the coil is coupled inductively into the plasma. The coil is driven by a 13.56 MHz RF voltage with the power supplied to the coil set at 500 W for this simulation. The oxygen pressure is varied between 4 and 100 Pa.

Figures 6.5 and 6.6 show the results of the HPEM modelling of our plasma geometry for 4 and 100 Pa respectively. The low-pressure case (figure 6.5) shows that the main positive ion is O_2^+ and not O^+. The charged particle densities are on the order of $2x10^{11}$ cm^{-3} with a maximum in middle between the electrode and the quartz window. Notably, the neutral species (O_2^*, O^*, O and $O_2^*(1S)$) have peak densities which are 2-3 order magnitude greater than the charged particles.

It can be seen that the neutral species densities across the top and bottom electrode

are more homogeneous than the charged particle distribution. In the case of PE-PLD, the substrate is placed in or close to this electrode gap which means there will be 2-3 orders of magnitude more neutral species impinging the substrate compared to charged particles. This highlights the importance of reactive neutral species for the deposition process, compared to ionic species which are traditionally mainly considered. It is well known that atomic oxygen (O) and singlet delta oxygen (O_2^*) are chemically highly reactive and play a major role during thin film deposition for O_2 background gas. Therefore, it seems highly likely that these reactive species will interact with the expanding plasma plume, oxidising the copper plume before depositing as a copper oxide thin film. Having a separate control over the reactive neutral densities, provides an additional control parameter for the thin film deposition process.

Figure 6.6 shows the HPEM simulation run for 100Pa pressure at 500W input power. By comparing the 4Pa pressure with 100Pa pressure, We can see that the charged species e and O_2^+ are more confined and look like a doughnut shape in front of the quartz cylinder. Peak densities of the charged species are slightly greater for 100Pa than 4Pa and are in the order of $2.5\times10^{11}\text{cm}^{-3}$. Furthermore, the reactive neutral species are 2-5 order magnitude greater than the charged species densities, however, the O_2^* and O distributions are no longer homogeneous across the electrodes but show a maximum where the charged particle densities peak. Nevertheless, the difference in reactive neutral densities for different pressures can be used as a control parameter to optimise the deposition process.

Figure 6.7 shows the densities of O and O_2^* as a function of pressure between 3 Pa and 100 Pa. Results from fig 6.7 show that, the density of O_2^* increases between 3Pa to 100Pa pressures and the densities ranges from $4\times10^{13}\text{cm}^{-3}$ to $1\times10^{15}\text{cm}^{-3}$. Whereas, the atomic oxygen densities O increases from 3Pa to 10Pa and then gradually decreases until 100Pa. This density trend of O and O_2^* is opposite to each other and this gives a wide range of optimisation of two different reactive species densities interacting with the expanding plume during thin film deposition. The main production mechanism for O_2^* is electron impact excitation. With

increasing pressure, the electron temperature decreases, or more accurately, the number of high-energy electrons decreases and the number of low energy electrons increases. Since the energy needed for the excitation of O_2^* is relatively low, i.e. 0.98 eV, compared to other processes, e.g. dissociation of O_2, requiring 4.5 eV, there is an increase in the O_2^* density and a decrease in O density with decreasing electron temperature.

This change in the type of reactive oxygen species can have an influence on the deposited thin film properties, depending on the exact chemistry of the PLD deposition process. Such an effect would be similar to what Blackwell et al. observed in their molecular dynamics and on-the-fly kinetic Monte Carlo simulations [105]. They found that the O/O_2 ratio influenced the stoichiometry, crystal structure and quality of the deposited ZnO films [105].

6.3 Conclusion

Finally, looking at the feasibility of PE-PLD as a deposition technique, we need to verify that the ICP plasma densities are similar to the Cu plume densities so that an interaction between the two can occur. The Pollux modelling showed that in front of the substrate the Cu density is on the order of 10^{14} cm^{-3}. The oxygen ion density is typically only 10^{11} cm^{-3} , however, the densities at a substrate surface of neutral reactive oxygen species, e.g. O and O_2^*, are in the order of 10^{14} cm^{-3} , like the Cu ions. Therefore, the ratio of reactive Cu to reactive oxygen in front of the substrate will be close to unity. Furthermore, the absolute values of these densities are very comparable to the densities found in other plasma-based CuO deposition techniques, e.g. magnetron plasma sputtering, where operating pressures of 0.1–1.0 Pa are used and ionisation is believed to be close to 100%, leading to particle densities of 10^{13}–10^{14} cm^{-3}. In conclusion, in PE-PLD we can have equal densities of Cu and oxygen arriving at a substrate so we could envisage deposition of a good quality copper oxide film with reasonable stoichiometry. Also, the fact that the absolute value of the particle densities in our PE-PLD technique are similar to those observed in traditional high-quality

CuO deposition methods, is encouraging for the feasibility of our proposed technique. The prospect of depositing metal-oxide films from separate metal and O sources seems feasible based on the modelling investigations presented in this chapter.

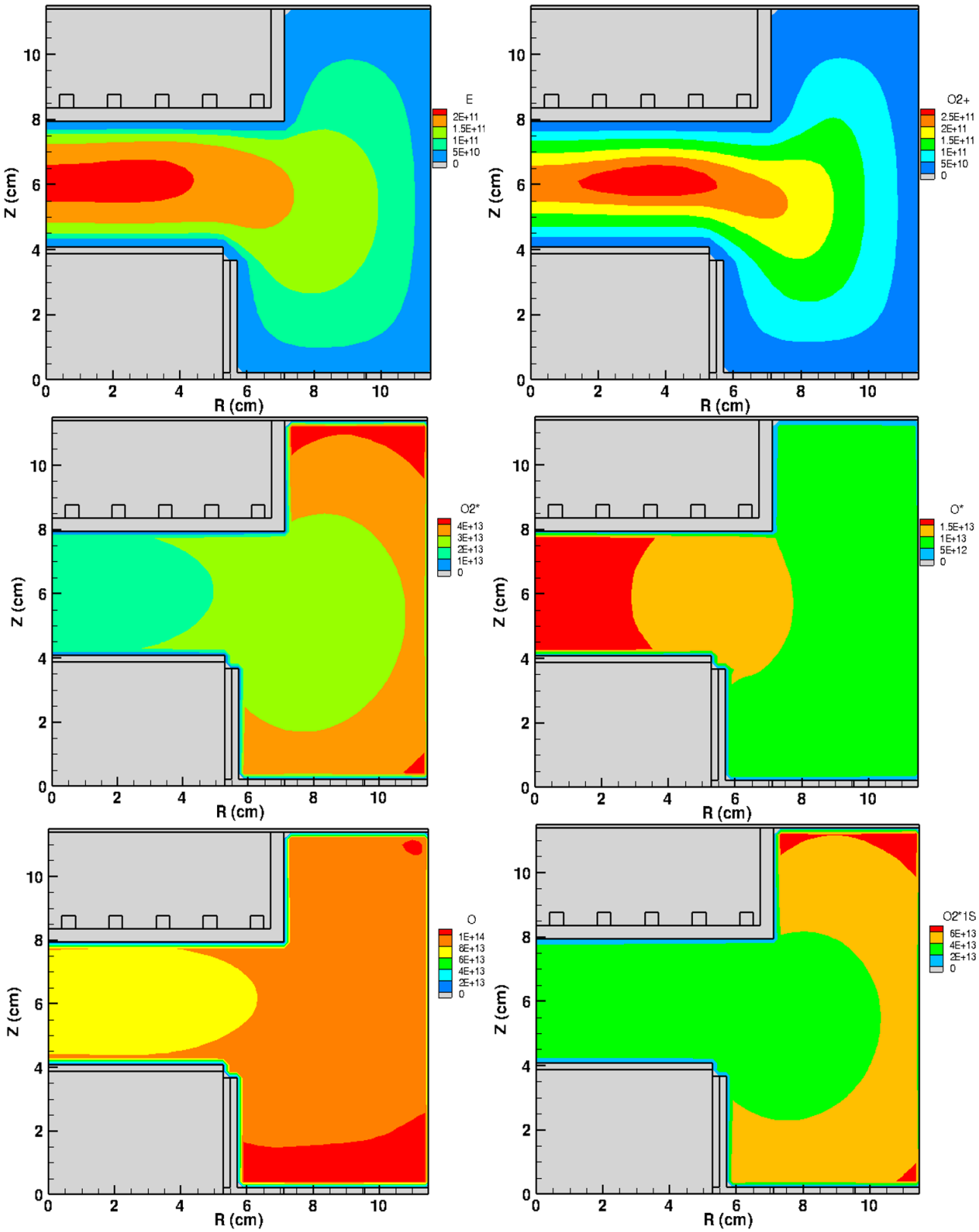

Figure 6.5: HPEM simulation result for 4Pa pressure run at 500W

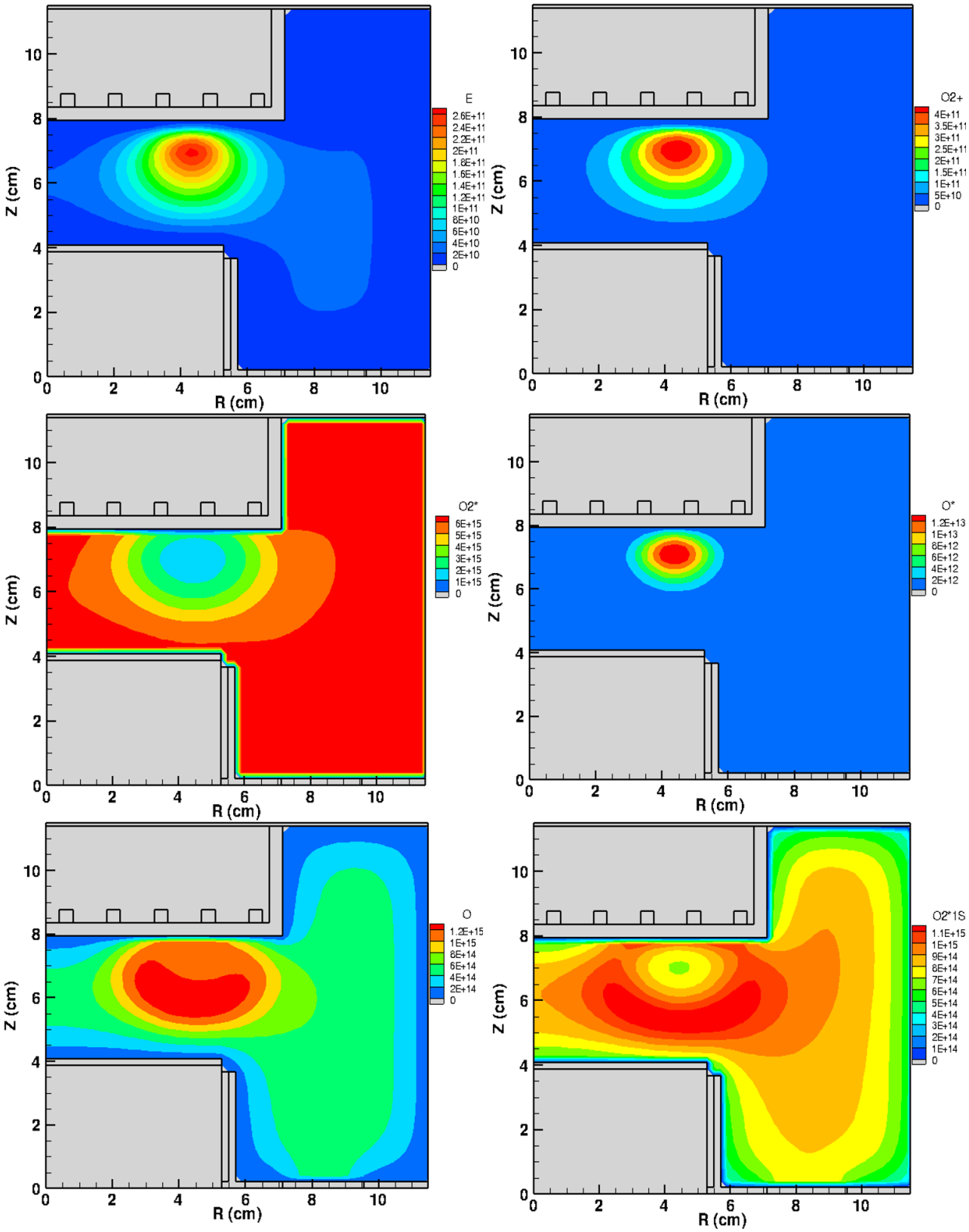

Figure 6.6: HPEM simulation result for 100Pa pressure run at 500W

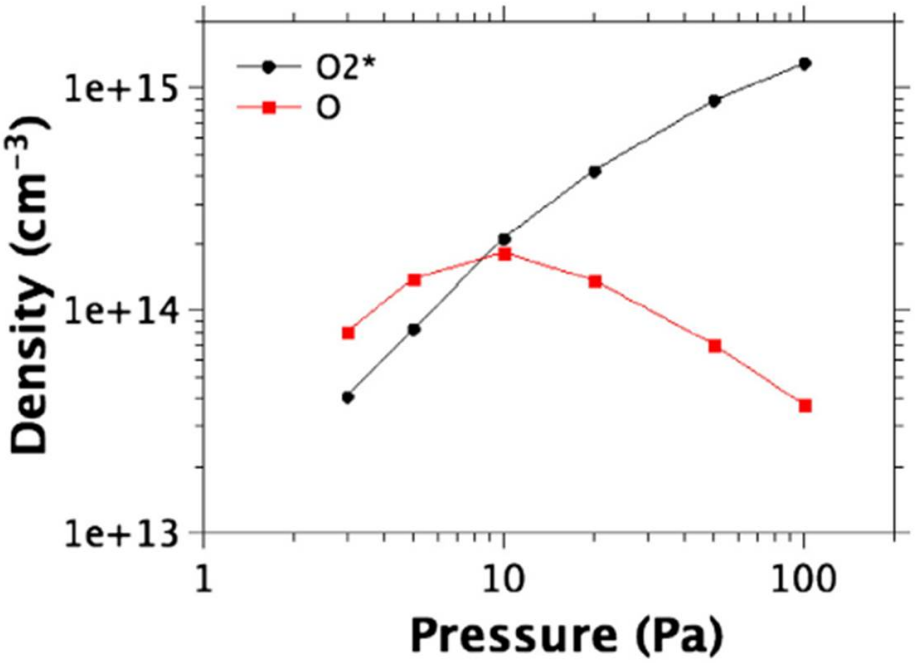

Figure 6.7: Modelled densities of O and O_2^* as a function of pressure in front of the centre metal electrode

Chapter 7

Time-resolved optical emission spectroscopy of laser-produced copper plasmas

7.1 Thermodynamic equilibrium

The laser-produced copper plasma that is used for the proof-of-concept study of PE-PLD is characterised using time-resolved optical emission spectroscopy. This technique allows the derivation of electron temperatures and densities, the assumption of Local Thermodynamic Equilibrium (LTE) can be made. I will first introduce the concept of LTE, and then derive how electron temperature and density can deduced from emission line intensities and widths. Subsequently, this method is applied to monitor the evolution of temperature and density in a laser-produced copper plasma that is expanding in vacuum, a background oxygen gas or a background oxygen plasma. Particular emphasis is placed on the validity of the LTE assumption and therefore the reliability of the measured plasma parameters.

7.1.1 Complete thermodynamic equilibrium (CLTE)

A uniform, homogeneous plasma in a closed system is considered to be CTE, when it obeys the principle of detailed balance for every process (i.e. each forward process is balanced by the reverse process). However, this needs to be valid for both collisional as well as radiative processes. If a plasma is in CTE, it exhibits the following properties: [106],

1. ***Equillibrium in temperature*** **:** All particles in the plasma, electrons, ions, atoms and molecules, have the same temperature, i.e. T_e=T_i=T_a=T_m=T.

2. ***Maxwell − Boltzmann velocity distribution*** **:** The velocity distribution of all particles in the plasma obeys a Maxwell-Boltzmann velocity distribution. [107]

$$f(v) = n\frac{4v^2}{\sqrt{\pi}\left(\frac{2K_BT}{m}\right)^{\frac{3}{2}}}exp\left(\frac{-mv^2}{2K_BT}\right) \tag{7.1}$$

Here, v is the velocity and m is the mass of the species in the plasma, T is the plasma temperature (which is same for all the species in the plasma) for complete thermodynamic equilibrium condition, n is the density of the plasma and K_B is the Boltzmann constant. As can be seen, the velocity distribution for a given species only depends on the temperature T of the plasma. Therefore, if the velocity distribution can be measured, the plasma temperature could be derived. However, in practice, it is not straightforward to measure the velocity distribution of particles in a plasma.

3. ***Boltzmann distribution of excited states*** **:** The density of the excited particles in upper state j compared to the lower state i follows a Boltzmann distribution given by:

$$\frac{n_j}{n_i} = \frac{g_j}{g_i}exp\left(\frac{-\Delta E_{ji}}{K_BT})\right) \tag{7.2}$$

where, n_j, n_i, g_j and g_i are the densities and statistical weights of the species in the upper

level (j) and lower level (i) respectively. ΔE_{ji} is the energy difference between levels j and i. K_B is the Boltzmann constant and T is the plasma temperature. Again, the distribution only depends on the plasma temperature. Therefore, if the density distribution of excited states can be measured, the plasma temperature can be derived.

4. ***Saha − Boltzmann distribution for ionised species*** **:** [42] The ionisation state of a plasma species is described by the Saha-Boltzmann distribution. For a plasma in thermodynamically equilibrium, from the densities of two different ionization stages of same element, the electron density (n_e) can be calculated:,

$$\frac{n_{i+1}n_e}{n_i} = \frac{2}{\lambda^3}\frac{g_{i+1}}{g_i}exp\frac{-E_{i+1}+E_i}{K_BT} \tag{7.3}$$

where, n_{i+1} and n_i are the densities in ionisation stages i+1 and i, respectively. E_{i+1} and E_i are the ionisation energies of ionisation stages i+1 and i respectively. n_e is the electron density, λ is the thermal de Broglie wavelength.

5. ***Planck function : Blackbody radiation*** [108] The emission of radiation follows the Planck distribution:

$$I_v = \frac{2h}{c^2}\frac{\nu^3}{e^{\frac{h\nu}{K_BT}}-1} \tag{7.4}$$

Here, ν, c, h and K_B denotes the frequency, speed of light, Planck's constant. The radiation temperature is the same as the plasma temperature.

Only when all five conditions are met, a plasma can be considered to be in CTE. In practice, in laboratory plasmas there are almost always radiation losses due to the limited size of the plasma which means that condition 5 is not met and the plasma is not in CTE.

7.1.2 Local thermodynamic equilibrium (LTE)

Nevertheless, even if the radiation processes are not in equilibirum, the collisional processes can still be in equilibrium. If this is the case, i.e. conditions 1-4 are satisfied, but not 5, then the plasma can be considered to be in Local Thermodynamic Equilibrium (LTE). For LTE to be valid, we need to consider the following:

1. For all the collisional processes to be in equilibrium, we need a high number of electron collisions and therefore a high electron density. The McWhirter criterion describes the minimum electron density needed to achieve LTE:

$$\boxed{n_e \geq 1.6 \times 10^{12} \sqrt{T_e} (E_j - E_i)^3 cm^{-3}} \tag{7.5}$$

where n_e is in cm^{-3}, T_e, E_i and E_j in eV. The Mc Whirter criterion is based on the assumption that collisional processes are 10 times larger than corresponding radiative processes [109].

2. The equilibrium is only local, i.e. in a specific point in space. It can change with spatial coordinates [106] as long as the variation is sufficiently small such that the equilibrium is completely determined by the *local* values of temperature, density and composition of the plasma [110]

3. Many LTE models assume that the plasma is optically thin, which means that radiative processes can be excluded from balances in the plasma. This clearly breaks the principle of detailed balancing for radiative processes and CTE is not satisfied..

7.1.3 Partial thermodynamic equilibrium (PLTE)

Partial thermodynamic equilibrium (PLTE) is a situation where the electron density is too low for all energy levels in an atom to be in equilibrium. The McWhirter criterion (eq. 7.5)

shows that the ground state of an atom is most likely to be no longer in equilibrium with excited states since these have the largest energy gaps. For many applications, it is still useful to consider only (part of) the excited states, which do still meet the equilibrium condition set by McWhirter. This is known as Partial Local Thermodynamic Equilibrium (pLTE). Using pLTE models, it is possible to derive information such as the electron temperature for the excited states under consideration. However, the assumption that the electron temperature is equal to the ion temperature is often no longer valid since due to the low electron density, electrons gain more energy per unit time, compared to the ions due to their lower mass. Therefore the electron temperature will be higher than the ion temperature. The PLTE condition between excited energy states can be verified using the McWhirter criterion to find the minimum electron required electron density.

7.1.4 Collisional radiative model

In order to study plasmas that are not in equilibrium (CTE, LTE or pLTE), a model known as a collisional-radiatve model can often be used. These models are widely used for studies of astrophysical plasmas, inertial confinement fusion plasmas, magnetic confinement fusion plasmas [111]. Ionisation and excitation in such plasmas strongly depends on radiative process as well as collisional processes. Therefore by considering the electron collision processes for excited states and also considering radiation processes in the plasma interior with appropriate conditions (i.e escape of radiation without trapping inside the plasma) [110], densities of different species can be calculated if the following assumptions are made:

1. Free electrons still follow a Maxwellian velocity distribution as given in the equation (7.1), provided the plasma is optically thin [110].

2. Radiation emitted between bound states should spontaneously decay, i.e. excluding the photoexcitation process(reverse process).

Provided a set of rate-coefficients is known, the population of atomic states can be calculated based on the above conditions, using the following equation (taken from [108]):

$$0 = \sum_{j \neq i} [n_i A_{ij} - n_j A_{ji} + (n_i B_{ij} - n_j B_{ji})\rho(\nu_{ij}) + n_e n_i \langle \sigma_{ijv} \rangle - n_e n_j \langle \sigma_{ijv} \rangle] \qquad (7.6)$$

$(n_i A_{ij} - n_j A_{ji})$, $(n_i B_{ij} - n_j B_{ji})\rho(\nu_{ij})$ terms in the above equation represents the radiative processes of transitions between bound states and free-bound transitions due to the recombination / photo-ionisation processes. Whereas, the term, $n_e n_i \langle \sigma_{ijv} \rangle - n_e n_j \langle \sigma_{ijv} \rangle$ represents the collisional processes. Equation 7.6 gives the steady-state solution of the atomic state distribution i, based on the assumptions described. The full set of equations for every level i needs to be solved simultaneously to find the atomic state distribution in the plasma. In this thesis I will focus on plasmas that are in LTE or pLTE, which means that full CR models are not needed.

7.2 Deriving plasma temperature from line intensities in an LTE plasma

As described in section 6.1, if a plasma is in LTE, one can derive the plasma temperature from the distribution of excited states in an atom. If the plasma is also optically thin, then the excited state distributions can be assumed to be related to the optical emission of lines which have this state as their upper level. In other words, intensities of emission lines from different upper levels can be used to derive the temperature of the plasma. In the next section I will derive the equation linking line intensities to plasma temperature. Then I will present measurements of plasma temperature using this technique on a laser-produced copper plasma. Similarly, from the line width of the emission line, densities are calculated and this will be discussed in the section below.

7.2.1 Theory linking line intensities to plasma temperatures

As described before, using peak intensity of emission lines originating from bound-bound transitions, the temperature T of the plasma can be calculated using the Boltzmann distribution by assuming the LTE condition is valid. The intensity of an emission line is given by,

$$I_i = n_{E_i} g_i A_i \tag{7.7}$$

In the equation (7.7) the intensity of the emitted line, I_i, is directly proportional to the population density of the excited state (n_{E_i}) , transition probability (A_i) and statistical weight (g_i), According to the Boltzmann distribution, for a plasma in LTE, the population density of excited state i, n_{E_i}, is given by,

$$n_{E_i} = n_0 \exp\left(\frac{-E_i}{KT}\right) \tag{7.8}$$

where n_0 is the ground-state density of the atom, K is the Boltzmann constant, E_i the excitation energy of the level i. Substituting equation (7.8) in (7.7) we get,

$$I_i = n_0 \exp\left(\frac{-E_i}{KT}\right) g_i A_i \tag{7.9}$$

Re-writing the equation (7.9) we get,

$$\frac{I_i}{g_i A_i} = n_0 \exp\left(\frac{-E_i}{KT}\right) \tag{7.10}$$

Taking the natural logarithm on both sides in order to cancel the exponential term on the right hand side.

$$\ln\left(\frac{I_i}{g_i A_i}\right) = \left(\frac{-E_i}{KT}\right) + \ln(n_0) \tag{7.11}$$

The electron temperature can be derived by plotting the left hand side equation against the excitation energy of the levels E_i which gives a slope of (-1/KT). From the slope we can

calculate the plasma temperature T.

A simplified form of this method is known as the line ratio method in which you only look at two emission lines. Using equation (7.9) we can see that the intensity ratio of these two lines, I_i and I_j is given by:

$$\frac{I_i}{I_j} = \frac{g_i A_i}{g_i A_i} \exp\left(\frac{E_j - E_i}{K T_e}\right) \tag{7.12}$$

However, the line ratio method is based on only two emission intensity values, i.e. effectively a Boltzmann plot with only two values, and this does not show any non-LTE effects. An electron temperature calculation using the Boltzmann plot with more than two points can show non-LTE effects by deviations from a straight line in the plot. This allows a better understanding of the LTE condition.

Spectroscopic constants g_i and A_i used for calculating the electron temperature are taken from the NIST database (http://www.nist.gov/pml/data/asd.cfm).

7.2.2 Electron temperature measurement

In the present work, time resolved spectra of laser produced copper plasmas in vacuum; background gas and background ICP plasma were studied to derive electron temperature and densities. Both for background gas and ICP plasma, 13Pa and 20Pa oxygen background pressures were used. Using equation 7.11 for selected neutral copper lines a Boltzmann plot is plotted and the electron temperature is calculated at different times as given in the table (6.1)

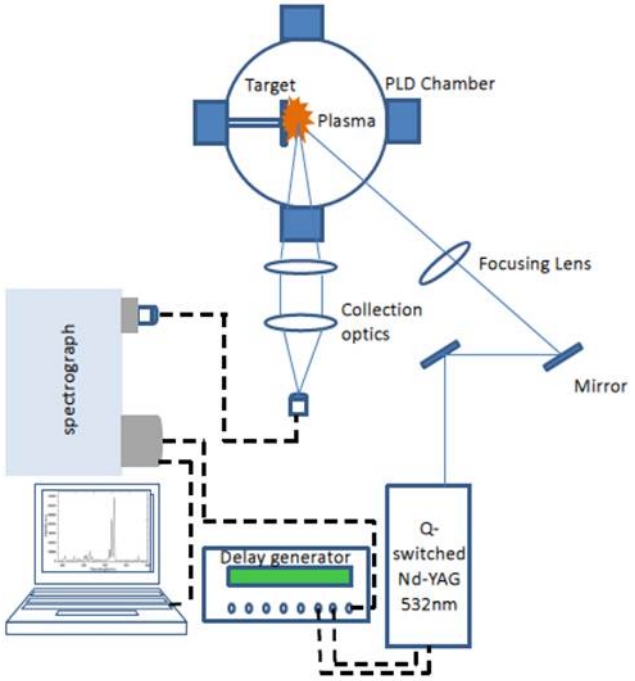

Figure 7.1: schematic representation of standard PLD for spectroscopy studies

The schematic representation of the set-up used for the spectroscopic studies is shown in figure 7.1. The plasma plume from the target is imaged onto an optical fibre (0.6mm diameter) using a 500mm lens. This optical fibre is attached to a Princeton 320PI spectrograph with an ICCD camera (Princeton PI-MAX).

A programmable timing generator (PTG) is used to set the delay time between the laser and the gating pulse of the ICCD. Software (Winspec/32) controls both the ICCD camera and spectrometer. The spectrometer covers the wavelength range between 300nm and 900nm with the grating line density of 150 lines/mm and the blaze wavelength is 300nm.

In order to obtain the original intensity of the emission line from the measured emission line intensity, left hand denominator of the equation (6.11) was multiplied by the Quantum emission (QE) of the spectrometer and grating efficiency (GE) (I.e) $\ln(I_i/(g_i A_i \times \%QE \times \%GE))$ Which is plotted against the left side of the Boltzmann plot against excitation

energy Ei to obtain electron temperature.

Gate delay(t_d)	**Gate width(t_s)**
50 -100 ns	10ns
100 -1000 ns	100ns
0 -100 μs	20 μs

Table 7.1: Gate widths and gate delays used in the experiment

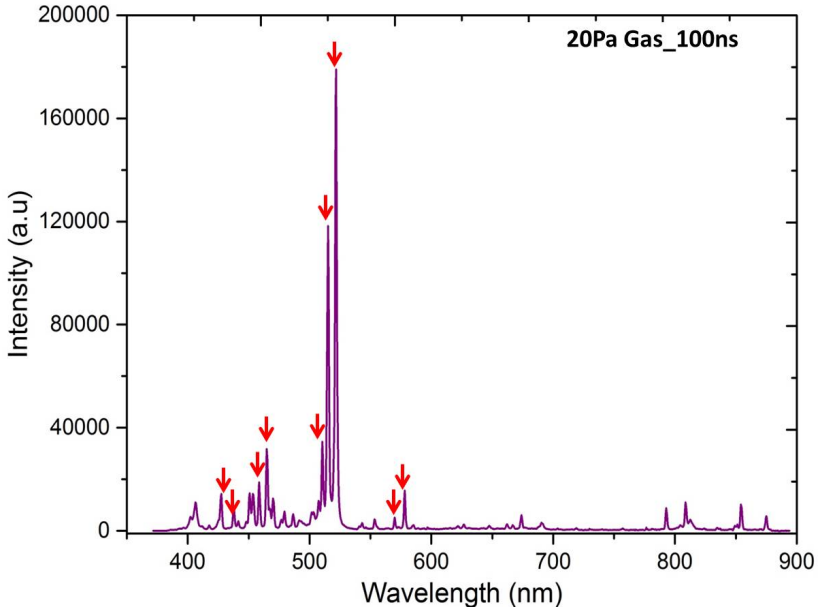

Figure 7.2: The copper emission spectrum for 20 Pa gas at 100ns gate width and 100ns gate delay(Red arrows indicate the lines used for this study)

Figure (7.2) shows an example of a measured emission spectrum at 100 ns delay for 20 Pa oxygen gas background. The emission lines used for the Boltzmann plot are 437.37nm, 450.344nm, 453.457nm, 458.123 nm, 510.437 nm, 515.093 nm, 521.301 nm, 569.872 nm and 577.614 nm Further details of the lines used in this study can be found in table 6.2. The electron temperatures derived from the Boltzmann plots (fig 6.3 shows an example) as a function of time for the different background conditions are shown in figures (7.4) (vacuum and gas) and (7.5) (plasma).

In graph (7.4), for the first 100ns, the plasma temperature for the vacuum case is slightly greater than for 13Pa and 20 Pa oxygen background gas cases, but the difference are very small. For vacuum the electron temperature is 1.64eV whereas for 13Pa and 20Pa electron temperature is around 1.51eV The temperature for the plume in the ICP plasma could not be determined for times before 50 ns since there was a large amount of continuum emission, obscuring the lines. However, after 100ns, all measurements show a similar temperature profile. In all cases (vacuum and background pressure), the temperature decays roughly exponentially as a function of time.

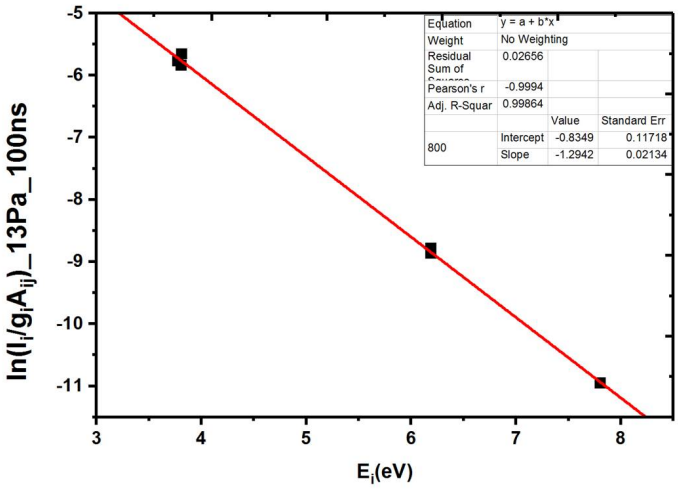

Figure 7.3: Boltzmann plot for 13Pa background gas at 100ns

The temperature calculated for ablation in an ICP plasma at 13Pa and 20Pa (figure 7.5) varies between 2eV to 0.7 eV for 50ns until 1μs. The temperature before 50ns can not be calculated using the Boltzmann method. For the plume in vacuum, plasma temperature exponentially decays between 50ns to 1μs and the temperature ranges between 1.64eV to 0.7eV. Whereas, for background gas, plasma temperature is less than both vacuum and ICP plasma, the temperature varies between 1.5eV to 0.54eV for 50ns until 100μs. In vacuum, the emission line decays quickly and after 1000ns there is no measurable emission, whereas for 13 Pa gas and 20 Pa oxygen gas the emission line exist until 100μ s.

Wavelength(nm)	$E_{lower\ level}$/ eV	$E_{upper\ level}$/ eV	g	A_{ij}
437.37	4.973	7.805	6	1.31e+07
450.34	5.575	8.325	6	2.50e+07
453.45	5.153	7.884	4	2.55e+07
458.12	5.102	7.885	6	2.56e+07
510.43	1.389	3.816	4	1.94e+6
515.09	3.786	6.191	4	1.03e+8
521.30	3.816	6.192	6	1.22e+8
569.87	1.642	3.816	4	2.501e+5
577.61	1.642	3.786	2	1.900e+6

Table 7.2: spectroscopic constant values used for calculating the electron temperature and electron density

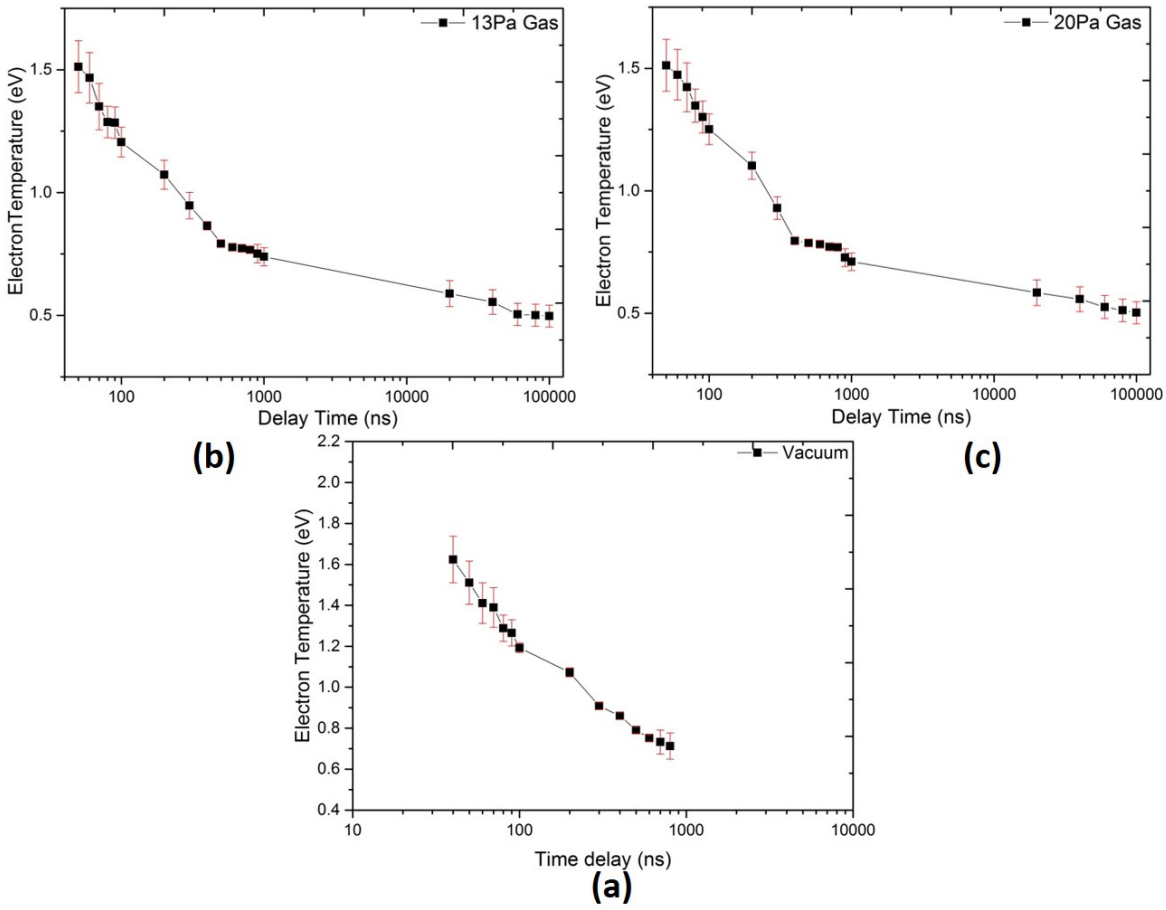

Figure 7.4: Electron Temperature as a function of delay time in (a) vacuum, (b) 13Pa oxygen gas, (c) 20Pa oxygen gas

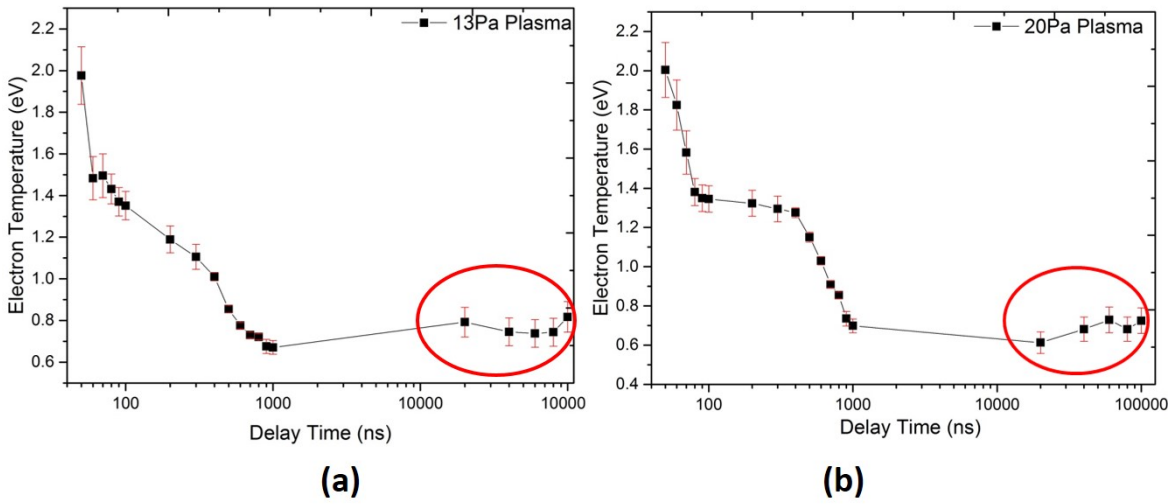

Figure 7.5: Electron Temperature as a function of delay time for (a) 13Pa plasma, (b) 20Pa plasmas (Red circles in the graph are not reliable because of deviations from LTE)

The reason for the fast decay of the plasma emission in the vacuum case compared to the background gas case is that expansion into a vacuum is faster than expansion into a gas environment. Expansion into a vacuum is a free expansion while into a gas initiates shock waves, slowing down the expansion. The faster expansion of the vacuum case means that the observed plume intensity falls quicker than for the case with a gas background.

Similar spectroscopical studies were carried out by [112] Unnikrishnan et al, for ablation with a 355nm Nd:YAG laser in air atmospheric pressure for copper target. Electron temperature calculated in their experiment decays exponentially between 300ns to 2000ns (i.e. 0.78eV-0.69eV). However, the temperature measured from our experimental condition is slightly greater than that. But the electron temperature decays exponentially in a similar way.

By comparing the experimental electron temperature with POLLUX simulation peak temperature, it can be seen that the experimental electron temperature values matches

very well with simulation values for the first 100ns. Temperature values for the first 100ns are 1.41eV-1.29eV at 13Pa and 1.49eV-1.38eV at 20Pa from POLLUX simulation. Whereas, experimental electron temperatures for the first 100ns are 1.51eV-1.20eV and 1.53eV-1.25eV.

Figure (7.5) shows that the electron temperatures measured for background ICP are higher than for background gas, for both 13 and 20 Pa pressures. It can be seen from HPEM simulations that the electron temperature in the ICP set at 500W is about 2.6-2.4 eV. This means that early in the plasma plume expansion, there are additional hot electrons available that can collide with the expanding plume, adding additional energy to the plasma plume, leading to a higher temperature. Since the densities in the early plume are very high, collisions are very frequent and the electrons very rapidly equilibrate to a Maxwellian distribution which leads to a Boltzmann distribution of the excited states in Cu atoms. The electron density in the plume is much higher than in the ICP plasma, explaining the only moderate increase in electron temperature, still well below the value found in the ICP itself. This higher initial temperature leads to an overall higher temperature throughout the expansion phase of the plume.

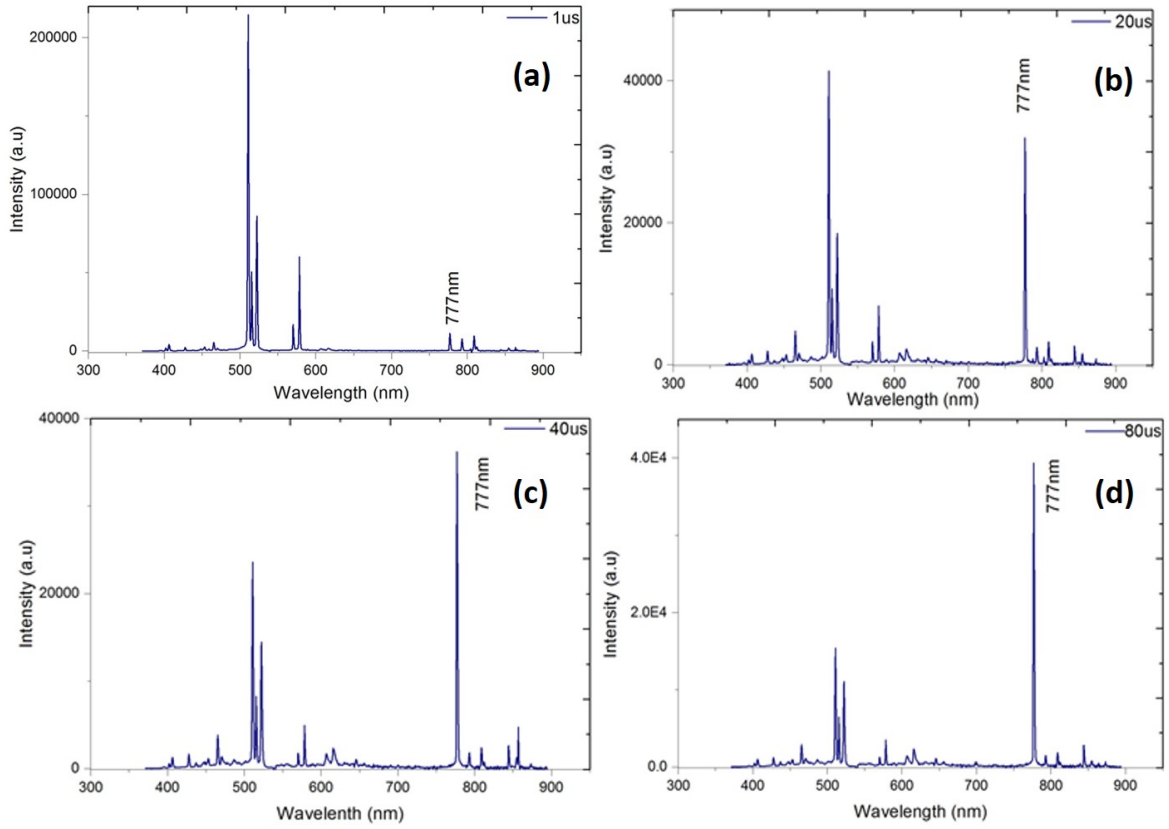

Figure 7.6: Emission spectrum for 10 Pa ICP plasma at (a) 1μs, (b) 20μs, (c) 40μs and (d) 80μs delay time

For the background oxygen gas environment, the Boltzmann plot fits perfectly to a straight line until 100μs therefore making the method reliable up until 100μs. However, in the ICP plasma after 1μs, the 515.093nm and 521.301nm line starts to deviate from the straight line in the Boltzmann plot which can be clearly seen from figure (7.7). This indicates a deviation from LTE for late times, 1-100 us.

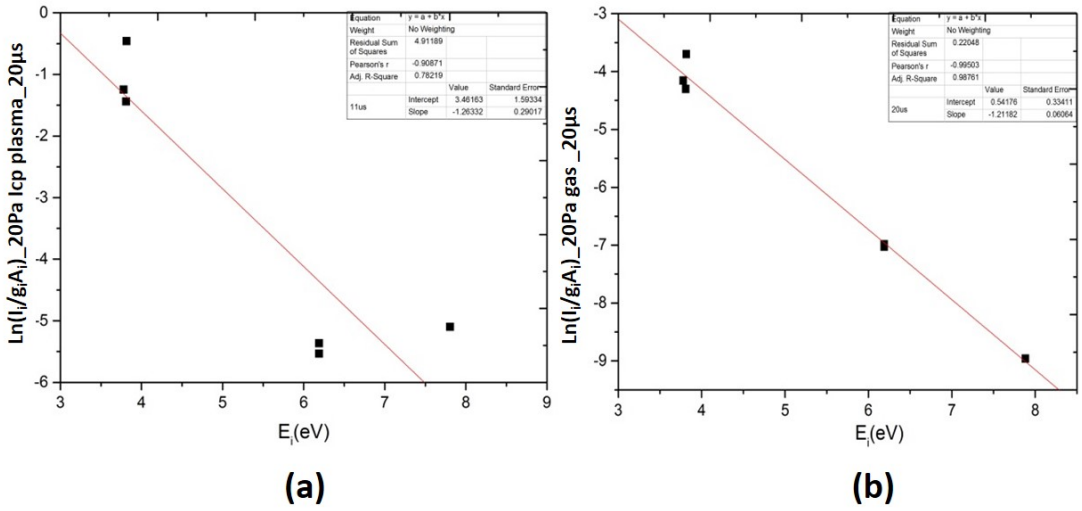

Figure 7.7: Boltzmann plot for (a) 20Pa ICP plasma and (b) 20 Pa gas for time 20 us

Even though the exact reasons for the deviation from LTE are not clear from these measurements, a indication can be found when looking at the 777 and 844 nm oxygen lines. As shown in Fig 6.6, these lines start to increase significantly after 1 us, whereas the neutral copper lines decay over the same time scales. The intensity of the 777 and 844 nm lines rises to a level well above what is observed in the ICP alone, indicating some interaction between the expansing plume and the oxygen ICP. Even though the exact mechanisms are unclear, it seems clear that there is some interaction and even chemistry occurring between the plume (electrons) and the background ICP. With the apparent result of significant increase in oxygen emission lines and a deviation from LTE for the neutral copper atoms. Further investigations are needed to further clarify this process. In particular, direct measurements of the O density via Two-photon Absorption Laser Induced Fluorescence would clarify if there is an increase in O density or only an increase in excited O states. Nevertheless, this is a first indication that there is an interaction between the laser-produced plasma plume and the background ICP, a necessary process for PE-PLD to work as intended.

7.3 Electron densities from line widths

From the the width of the emitted spectral lines, plasma parameters can be derived. This section deals with the different broadening mechanisms that affects the width of a spectral line.

7.3.1 Natural line broadening

Natural broadening in an emission line profile arises due to the effect of Heisenberg uncertainty principle,

$$\Delta E \Delta t \sim \hbar \tag{7.13}$$

In quantum mechanics, an excited state of an atom will have a life time after which it decays spontaneously to a lower state. However, the uncertainty principle states that due to the finite life time of the upper state, there will be an uncertainty in the energy of the state. This in turn leads to a spread of the wavelengths emitted, i.e. a broadening of the emission line observed. The resulting line profile can be fitted using a Lorentzian profile [108],

$$\phi(\nu) = \frac{\gamma}{4\pi^2} \frac{1}{(\nu - \nu_0)^2 (\gamma/4\pi)^2} \tag{7.14}$$

$$\gamma = \sum_j A_{ij} \tag{7.15}$$

In the equation (7.14), γ is the spontaneous decay rate, A_{ij} is the transition probability of upper state (i) and lower state (j). Typically, natural broadening is a small effect in most plasmas, much smaller than other broadening mechanisms.

7.3.2 Doppler broadening

Thermal motion of the radiating particles will have a small variation in the emitted frequency from those of the atoms at rest due to the Doppler shift. The particles moving away from the observer are red shifted (longer wavelength) and moving towards the observer are seen as blue shifted (shorter wavelength). Hence a higher plasma temperature leads to a wider velocity distribution and therefore a wider spectral profile.

The Doppler shift is given by,

$$\nu = \nu_0\big(1 \pm \frac{v_s}{c}\big) \tag{7.16}$$

$$\Delta\nu = \nu - \nu_0 = \nu_0\frac{v_s}{c} \tag{7.17}$$

In Equation (7.16), we calculate the observed frequency (ν) from the unshifted frequency (ν_0) multiplied by the radiating particle velocity (v_s) travelling in a parallel direction to the observer.

At a given temperature, the velocities of the atoms will be distributed based on a Maxwellian velocity distribution. To estimate this broadening effect, in LTE, the line shape of the photon flux ϕ is given by a Gaussian profile [108],

$$\phi(\nu) = \phi(\nu_0)exp\big(\frac{-(\nu-\nu_0)^2}{\nu_0^2}c^2\frac{m_i}{2kT_i}\big) \tag{7.18}$$

Therefore fitting the peak to the Gaussian profile, we get the FWHM of the peak, which is given by,

$$\Delta\lambda_{1/2} = 2\lambda\sqrt{2KT\ln 2/mc^2} \tag{7.19}$$

In the equation (7.19),$\Delta\ \lambda_{1/2}$ is the FWHM; λ is the wavelength of the emission line (nm), k is the Boltzmann constant (JK$^-$1), T(K) is the temperature, m (Kg) is the atomic mass and c is the speed of the light (ms^{-1}). FWHM from equation (7.19) for the Cu I emission line

of 515.093 nm at a temperature of 20000 (K) is 0.00588nm, which is small when compared with the experiments we carried out. Therefore, broadening due to the Doppler effect is negligible for our experimental condition.

7.3.3 Stark broadening

For the laser-produced plasmas under study in this thesis, the dominant line broadening mechanism is Stark broadening. The high density of charged particles in the plasma induces electric fields that disturb the energy levels in atoms and ions via the Stark effect. This perturbation of the energy level structure of an atom/ion results in broadening of emission lines.

For plasma in LTE, the electron density can be calculated from the FWHM of the Stark-broadened emission line using the expression [113] [114],

$$\Delta\lambda_{1/2}(nm) = 2\omega\left(\frac{N_e}{10^{16}}\right) + 3.5A\left(\frac{N_e}{10^{16}}\right)^{5/4}\left[1 - \frac{3}{4}N_D^{-1/3}\right]\omega \tag{7.20}$$

The second term on the right hand side in this expression is due to ion-ion collisions. In our case the ion-ion collision effect is very small so the second term of this expression is negligible. This simplifies equation (7.20) to

$$\Delta\lambda_{1/2}(nm) = 2\omega\left(\frac{N_e}{10^{16}}\right) \tag{7.21}$$

ω is the electron impact parameter, N_e is the electron density, $\Delta\ \lambda_{1/2}$ (nm) is the FWHM of the broadened emission line. By measuring the Stark broadening of emission lines, the electron density can be determined.

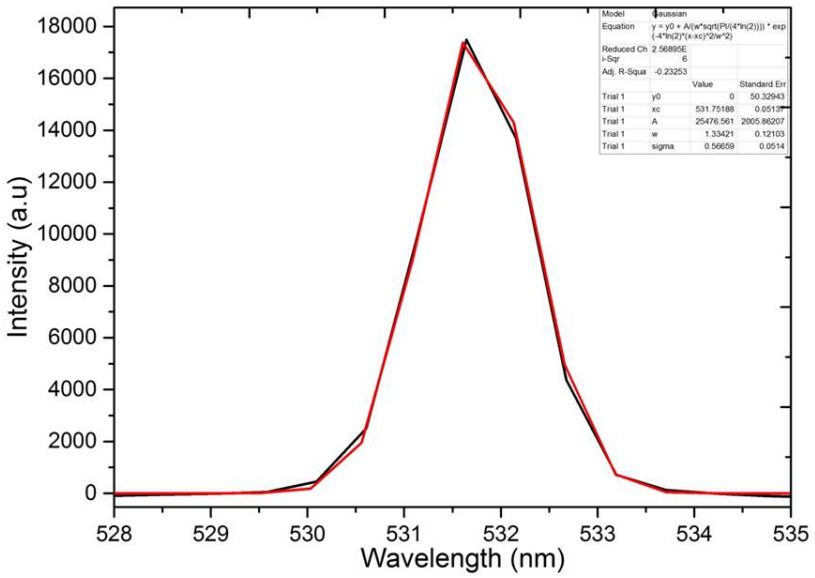

Figure 7.8: Instrumental broadening calculated from Nd:YAG 532nm laser

7.3.4 Electron density measurements in a laser-produced copper plasma

In an experiment, there is also instrumental line broadening to be considered, i.e. the broadening of emission lines due to the measurement instrument used. The instrumental line width in our experiment was determined by measuring the line width of a narrow-band laser line with the same diagnostic setup. This instrumental line width is subtracted from all further measurements to obtain the Stark broadening of emission lines. The line measured from a 532 nm Nd-YAG laser is fitted with a Gaussian peak as shown in the figure (7.8) and the FWHM of the peak in measured to be 1.33nm

Using equation (7.21), the electron density as a function of time was determined from the FWHM of the 521.301nm Cu line. Figures (7.9), (7.10), and (7.11) show the measured electron densities for the laser-produced plasma in different backgrounds: vacuum, gas and plasma. For all cases, we observe a density of a few times 10^{18} cm^{-3} after 50 ns. This density rapidly decreases to below 10^{17} cm^{-3} at 100 ns and below 10^{16} cm^{-3} after 1μs. Between 1 and 100 us, the density remains roughly constant. This is in line with the plume expansion that was already observed in the temperature. The case with a vacuum background shows

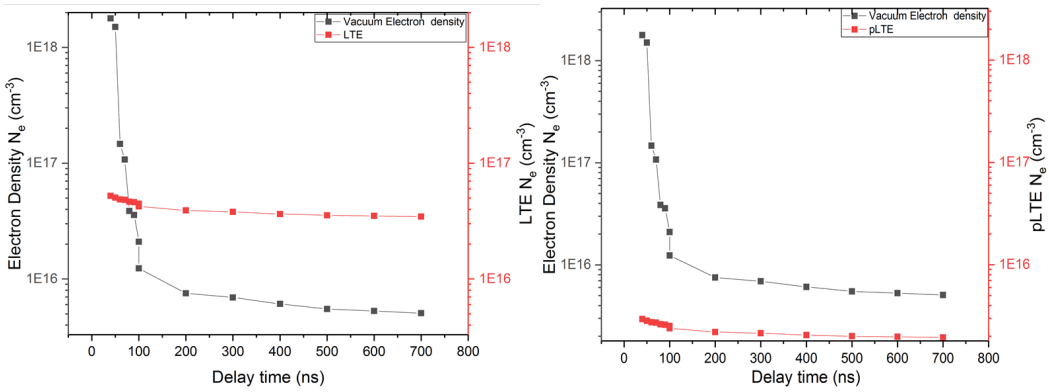

Figure 7.9: Electron density measurements in vacuum and calculations of densities required for LTE and pLTE

a faster expansion, i.e. drop in density than the cases with a background gas or plasma. This can again be explained by the free expansion in vacuum compared to the expansion in a gas / plasma where shock waves will be formed, slowing down the expansion. These observed densities when compared to Unnikrishnan et al [112] experimental condition for Cu target at 355nm Nd:YAG laser is two orders of magnitude less than our experimental condition. However, the electron density decay exponentially between 300 ns to 2000 ns (i.e electron density varies between ($2.0\text{x}10^{14}$ - $4.5\text{x}10^{13}$ cm^{-3}) which is same as our experimental condition.

For the cases with a background gas, the experiments can be compared to the POLLUX modelling from chapter 5. Fig (6.3), (7.10) and 7.11 shows this comparison. It can be seen that observed density from Pollux at 13Pa and 20Pa near the front of the target are of the order of $8\text{x}10^{17}$ cm^{-3} whereas, experimentally observed electron density for 13Pa and 20Pa are order of $3.16\text{x}10^{16}$ cm^{-3} and $4.77\text{x}10^{16}$ cm^{-3} which is a reasonable agreement to the POLLUX simulation.

From the literature [92] and our HPEM modelling in chapter 5, it is shown that the reactive oxygen density of the ICP plasma is in the order of 10^{14} cm^{-3}. The observed densities in the laser produced plasma are several order of magnitude larger during the initial expansion phase. However, after about 1 us, they have decreased to below 10^{16} cm^{-3},

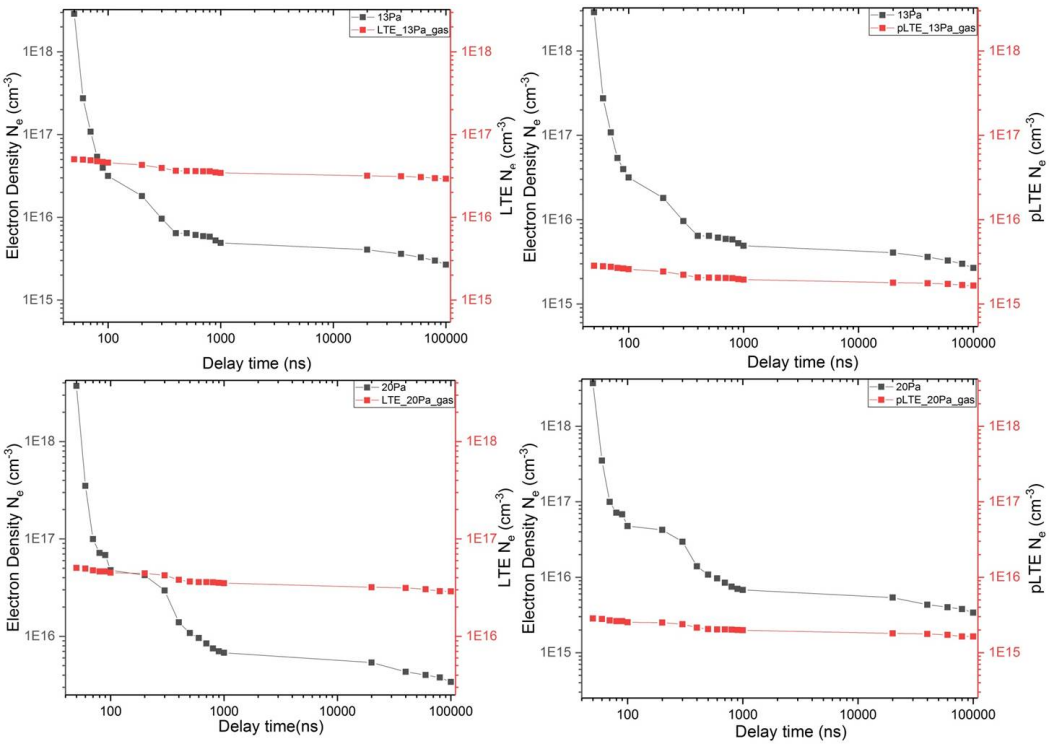

Figure 7.10: Electron density calculation for background gas at 13Pa and 20Pa for pLTE and LTE condition

not too far off what is observed in an ICP, making an interaction between the two plasmas feasible. Moreover, after $1\mu s$ densities of cu plume is decreased and some evidence of this interaction can possibly be found in the observed strong increase in intensity of the 777 nm adn 844 nm OI lines (see fig. 7.6) as well as the deviation from LTE conditions found in the Boltzmann plots (fig. 6.7).

7.4 Validation of LTE condition

Figures 6.8 - 6.10 also show the calculated values for the minimum electron density to satisfy the LTE condition (McWhirter criterion). The left hand figures show the LTE condition, the right hand figures the pLTE condition (between the energy levels of the emission line).

It is clear that the plasma was not in full LTE for most of the ablation process, i.e. ¿70 ns. However, the more relaxed concept of pLTE was met for almost all of the measurements.

This highlights an important point about the LTE assumption in that even though pLTE is observed (e.g. via a Boltzmann plot), this does not necessarily mean the plasma is in full LTE which means that further investigations are needed to verify the accuracy of these widely used techniques in these types of experiments.

Moreover, the observed deviations from a straight line in the Boltzmann plots for ICP background measurements after 1 μs can possibly be evidence of the interaction of a non-LTE ICP plasma with the relatively low-density plume. This interaction transfers energy from the ICP to the plume via collisions and reactions, possibly populating specific levels preferentially.

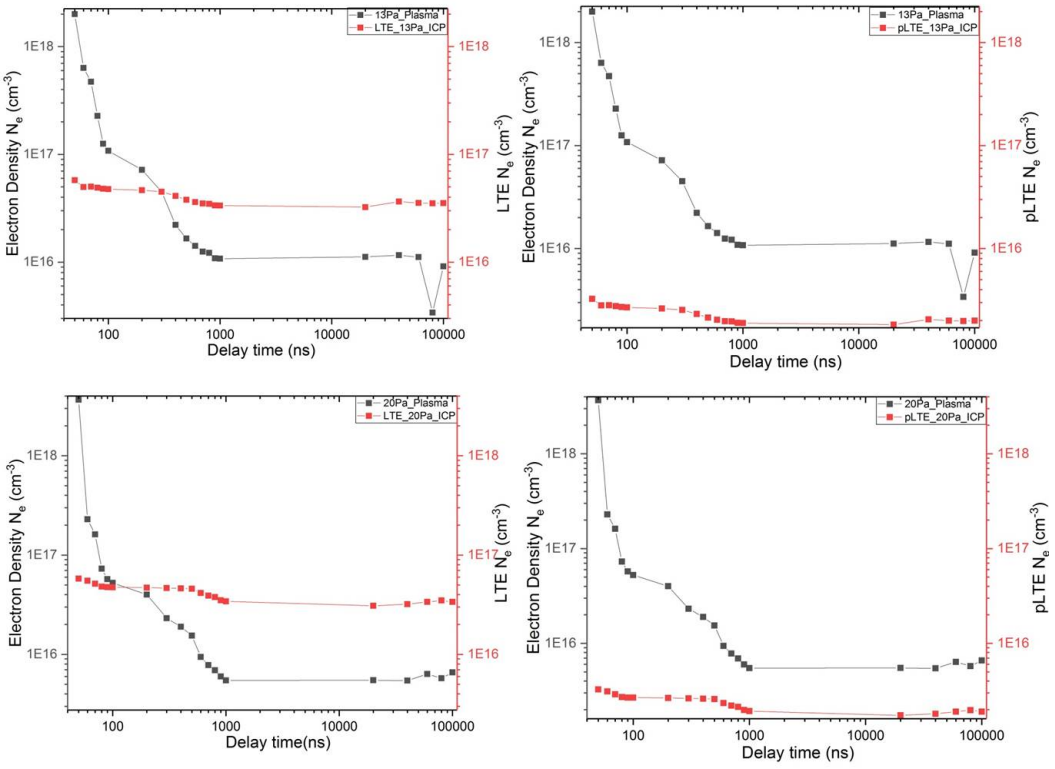

Figure 7.11: Electron density calculation and Mc Whirter criterion for ICP plasma at 13Pa and 20Pa condition for pLTE condition

However, this energy is not equilibrated completely because the electron density is too low at this point (i.e. below the McWhirter criterion). To further quantify this possible

explanation, further measurements are required.

7.5 Conclusion

In conclusion, this chapter results estimate the electron temperature and electron density of the laser produced Cu plasma at different background pressure condition using time resolved optical emission spectroscopy. Plasma emission from Cu plume at vacuum expands faster than background pressure and background ICP plasma condition. In a same way, electron temperature and electron density measured from the experiments are in good agreement with POLLUX simulation. Further, the electron density of the plasma was calculated using stark broadening and the electron temperature of the Cu plasma at different time scale was calculated from the Boltzmann plot. Both electron temperature and density are good in agreement with POLLUX simulation. Furthermore, the measured electron temperature and electron density is verified with MC Whriter criterion (eq 6.5) to check the assumption of LTE. However for the plasma emission $> \sim$ 70ns was not in full LTE. Hence, the concept of pLTE was verified for all measurement.

Chapter 8

Proof of concept - Thin film deposition using PE-PLD

In this chapter a proof-of-concept study of thin-film deposition using our novel PE-PLD techniques is presented. As well as characterizing the properties of the films deposited with PE-PLD, we also compare these films to traditional PLD films as well as perform additional experiments to shed light on the plasma mechanisms underpinning PE-PLD (e.g. E-mode ICP operation and de-synchronised ICP and laser experiments) A schematic description of all the different experiments is shown in figure 8.1 The proof-of-concept experiments

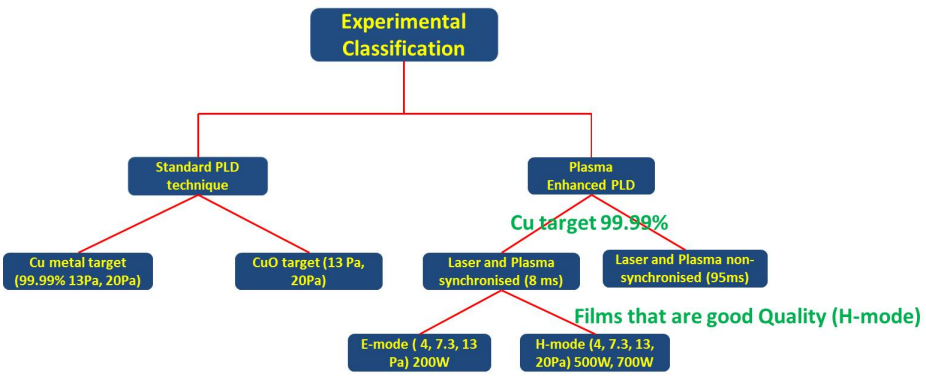

Figure 8.1: Experimental classification based on two different approach

are for PE-PLD with a synchronised set up and with a H-mode ICP. The others, non-synchronised and E-mode are to better understand the underpinning processes and both standard PLD experiments are for benchmarking the PE-PLD films. A detailed description of the experimental set-up, as well as a discussion on E-mode and H-mode in ICPs can be found in chapter 4. The films deposited will be characterised using the following techniques: XRD, SEM-EDX, AFM and four-point-probe under different experimental conditions More details on these surface analysis techniques can be found in chapter 7.

8.1 Crystal size calculation and phase identification using X-ray diffraction

First, a standard PLD technique was used to provide a benchmark for the new PE-PLD experiments. Next, the results of the PE-PLD experiments will be presented. It should be noted that in neither of the experiments there was any substrate heating or post-annealing of the films (as is common in standard PLD techniques).

8.1.1 Standard PLD experiment

Standard PLD experiments were carried out using Cu metal targets with 99.99% purity (Testbourne Ltd) and CuO targets (99.9%, Mi-Net Technology Ltd) to deposit thin films in a background oxygen pressure of 4Pa to 20Pa. The films were deposited on quartz substrates and analysed using X-ray diffraction to determine the phase of the films. The distance between target and substrate were kept at 4 cm. The laser usedwas a Continuum Minilite II, frequency-doubled (532 nm), Q-switched Nd:YAG laser. The pulse length was 5 ns, pulse energy was 35 mJ and focal spot 0.5 mm. Further, the experimental details are discussed in chapter 4. The gas pressures used in these experiments were 4Pa to 20 Pa. The deposition time was 1hr 30 min.

Figure (8.2) shows the X-ray diffraction patterns of CuO thin films deposited using a Cu target at two different background gas pressures of 13Pa and 20Pa, respectively. A $\theta/2\theta$ scan was carried out between 20-80 degrees where the step size was 0.05 degree for all films. The diffraction patterns of both these thin films showed prominent peaks at 32.4°, 35.5°, 38.8°, 53.6°, 65.9°, 68.2°, which corresponds to the $< -110 >$, $< 002 >$, $< 111 >$, $< 020 >$, $< 310 >$, and $< 220 >$ planes of monoclinic CuO according to JCPDS card no.**045_0955** (`http://www.crystallography.net/cod/`).

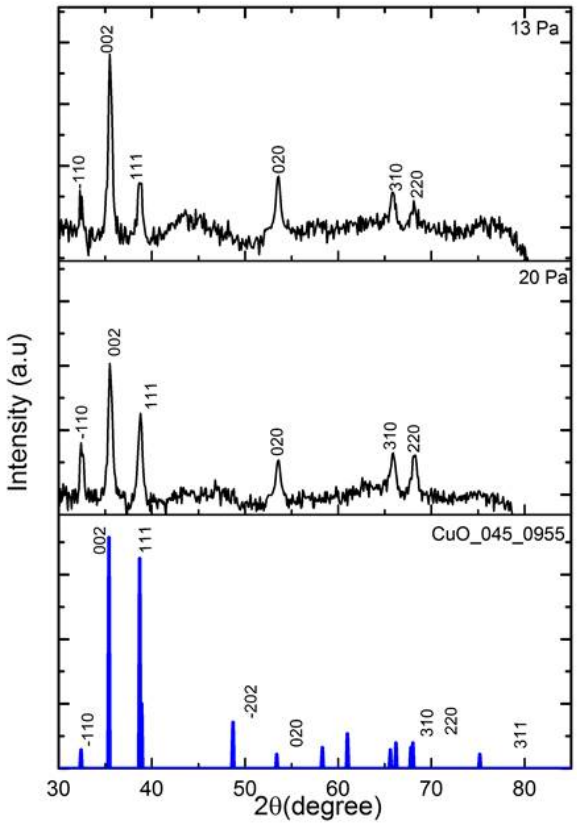

Figure 8.2: CuO thin film at background gas pressures 13 Pa (top), and 20 Pa (middle) Cu target

The intensities of all these peaks are found to be higher at 13Pa background gas pressure compared to 20Pa background gas pressure, indicating a higher degree of crystallinity for the 13 Pa case. Nevertheless, at both pressures it is clear that some CuO forms. It is known that neutral O_2 does not interact with a pure copper film, hence these experiments are evidence

that the Cu plume interacts with the O_2 gas and dissociates some of the gas to form O which subsequently reacts with the plume and/or film to form some CuO.

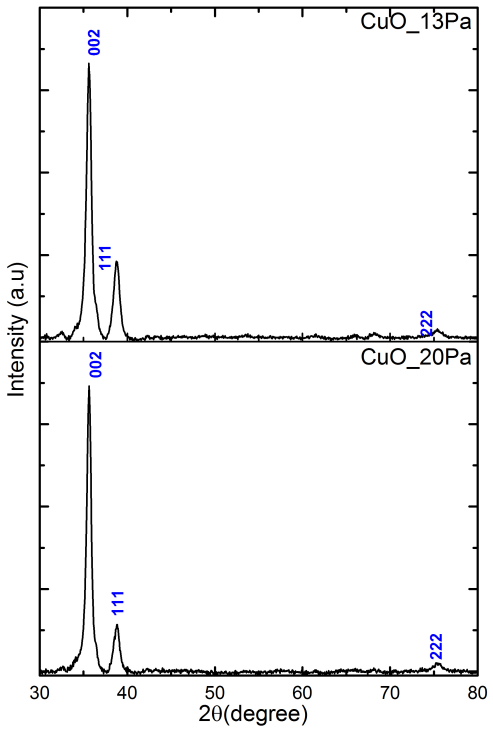

Figure 8.3: CuO thin film deposited using CuO target at two different pressure 13Pa and 20Pa

Next, similar PLD experiments were carried out for a CuO target and Fig (8.3) shows the XRD pattern of CuO thin film deposited at 13Pa and 20Pa. The XRD peaks from these two experiments matches with CuO thin film standard JCPDS card no 045-0955 and the major orientation of the crystals are $< 002 >$ and $< 111 >$. The particle growth along $< 002 >$ is not surprising since this has the lowest surface energy [115]. When comparing films grown from CuO targets to the ones grown from Cu targets, we see low index facets $< 002 >$, $< 111 >$ and $< 222 >$. This can be explained by the fact that the metal target has a lower melting point when compared to the oxide target. Hence, the thermal properties of

the target material affect the orientation of the thin film that is grown.

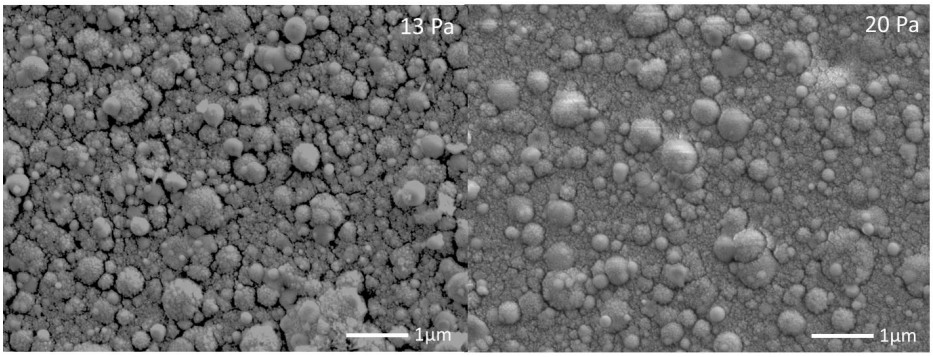

Figure 8.4: CuO thin film deposition using CuO target at 13 and 20 Pa

Fig 8.4 is an SEM image of the CuO thin films deposited using CuO targets. It is clear that there are no particular defined crystal orientations and the film shows bigger blobs of particles formed on the surface. Furthermore, the four point probe tests show a high resistivity of the the film (out of range), indicating a poor quality of the film. This is likely due to the absence of substrate heating and post-annealing in our set-up. As mentioned in chapters 2-4, it is known that this is a critical step in traditional PLD.

8.1.2 Plasma enhanced PLD

The PE-PLD experimental setup is described in detail in chapter 4. Here, we perform proof-of-concept experiments for the PE-PLD technnique using an H-mode ICP (see chapter 4 for details) and a synchronisation between laser and ICP . In addition, experiments using an E-mode ICP and experiments with a non-synchronised laser and ICP were performed in order to gain a better understanding of the relevant physics processes of PE-PLD.

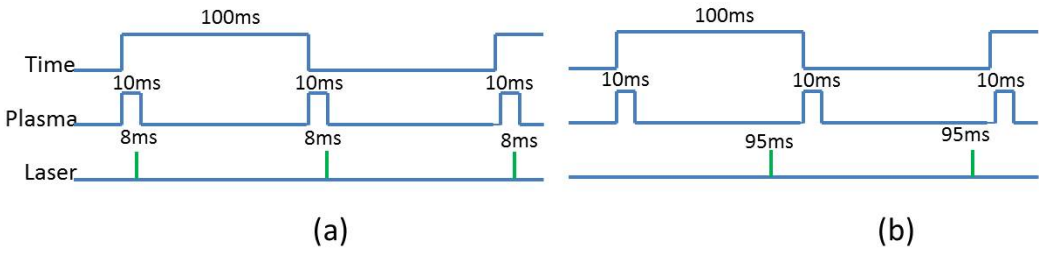

Figure 8.5: Laser and Plasma pulsing time (a) Synchronised: Plasma is ON for 10ms and off for 90ms and the laser is fired at 8ms (b) Non-Synchronised: Plasma ON for 10ms and OFF for 90ms and the laser is fired at 95ms (i.e) 5ms before the plasma is ON

More details about the synchronised and non-synchronised experiments can be found in figure 8.5. The overall repetition rate of the set-up is 10 Hz. Within 1 cycle of this, the ICP is on for 10 ms (i.e. 10% duty cycle). In the synchronised experiments, the laser is fired during the plasma on phase, more specifically at 8 ms after the start of the ICP pulse, leaving 2 ms of ICP plasma after the laser pulse. In the non-synchronised case, the laser is fired when the plasma is off. I.e. 95 ms after the ICP pulse, which is 5 ms before the next ICP pulse. This allows the study of thin film oxidation by the ICP plasma after a Cu plume passes through a neutral gas background. As mentioned before, there is no direct heating of the substrate in these experiments. However, the ICP plasma will provide some heat to the substrate. To monitor this heating by the ICP, a thermocouple was inserted in the middle of the substrate holder.

At the highest ICP power of 700 W the temperature measured was 30°C ±4°C. For all other experiments, the temperature did not rise above room temperature. This means that the heating by the ICP is a very limited effect, compared to typical substrate heating temperatures of several hundreds of degrees. CuO thin films were deposited at 4Pa, 7.3Pa, 13Pa and 20Pa pressures. In H-mode, the power used to operate the ICP at 4Pa, 7.3Pa and 13Pa was 500W and for 20Pa it was 700W, since a higher power was needed at that pressure to achieve H-mode. In E-mode the power was 200 W for pressures of 4, 7.3 and 13 Pa.

8.2 Inductively coupled plasma in H-mode

Fig (8.6) shows the XRD analysis of films deposited with PE-PLD with an inductively coupled plasma operated at H-mode at 4Pa, 7.3Pa, 13Pa and 20Pa. The thin films produced with the PE-PLD method show two different oxide forms of copper as identified by a standard JCPDS cards no CuO: 1011148, Cu_2O: 05-0667. The relatively good peak heigths compared to the background indicate that there is a significant amount of crystalline material in the films compared to amorphous.

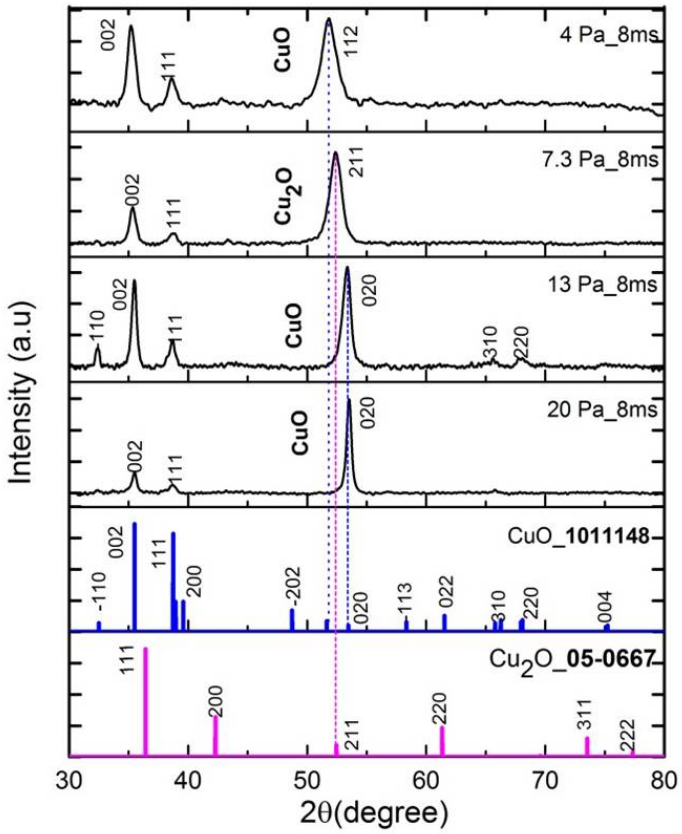

Figure 8.6: XRD pattern for Inductively coupled plasma (H-mode) at different pressures

The first observation is that; we no longer exclusively see CuO phases, but now we see Cu_2O peaks in the XRD spectrum, most notably, the $< 211 >$ plane in the 7.3 Pa case. Furthermore, in contrast to the films deposited with standard PLD, i.e. in a gas background,

these films do not show a dominant $< 002 >$ plane, but a $< 112 >$ plane CuO at low pressure, changing to $< 211 >$ in Cu_2O for 7.3 Pa, changing to $< 020 >$ in CuO for pressures 13 and 20 Pa. The $< 020 >$ plane requires more energy to grow than the $< 002 >$ plane that is observed in normal PLD, however, it is more desirable for most of the semiconductor applications. In our case this is mainly because, increasing the oxygen pressure in H-mode increases the atomic oxygen due to electron impact dissociation [80] and the reactive oxygen and atomic oxygen provides energy to grow the high index plane $< 020 >$. Similarly, Jean-Pierre [6] showed activated deposition with an RF plasma oxygen source leads to the growth of the $< 020 >$ plane, which is considered more active for catalytic applications due to its low packing density.

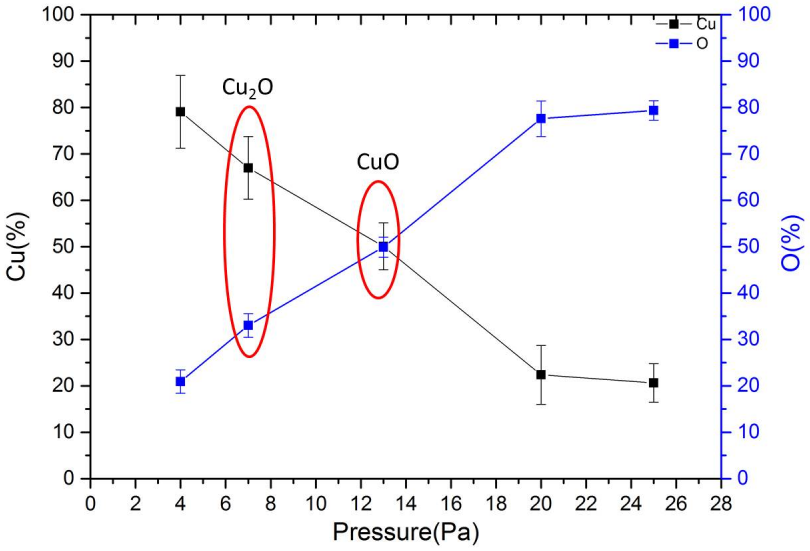

Figure 8.7: Stoichiometry of the thin film using SEM-EDX

8.2.1 Stoichiometry of the thin film SEM-EDX

Figure 8.7 shows the SEM-EDX analysis of the PE-PLD thin films produced at different pressures. As can be expected, an increase in ICP pressure leads to an increase in O content in the films, increasing from 20% at 4 Pa to 80% at 20 Pa. However, at 4Pa, 80% of the film is Cu, nevertheless, the XRD results show a CuO peak. This indicates that there are

small areas of crystalline CuO in the film, which are surrounded by very Cu-rich, or pure Cu areas. At 7.3 Pa, the ratio Cu:O is 2:1, indicating stoichiometric Cu_2O and at 13 Pa the ratio Cu:O is 1:1, indicating stoichiometric CuO. This is in line with the XRD findings which shows a major Cu_2O peak $< 211 >$ for 7.3 Pa and a CuO peak $< 020 >$ for 13 Pa.

At 13Pa we see stoichiometric CuO which is predominantly in the (020) phase, however, there are also well defined extra peaks, indicating $< 110 >$, $< 111 >$, $< 310 >$, $< 220 >$ phases. The transition from Cu_2O films to CuO films has been observed before in the literature, Z H Gan and co workers [116] deposited CuO thin film by filtered cathodic vacuum arc method and from this technique they found that extra oxygen with high substrate bias leads to the formation of CuO from Cu_2O and the reaction process is given as $Cu_2O + O \rightarrow 2CuO$.

Also, the growth of the high index $< 020 >$ plane of CuO has been seen before. By e.g. Jean-Pierre et al [6] when they used an oxygen RF plasma the CuO$< 020 >$ plane was seen in their result. Finally, further increasing the pressure to 20Pa did not make any change in the plane orientation from $< 020 >$, however the EDX results show 22.36% of Cu and 77.60% O content , indicating a not stoichiometric film. Similarly, O. Daoudi et al., [117] deposited CuO thin film by modified SILAR method, EDX results of the thin film confirms the existence of copper and oxygen. Samples deposited for different cycles shows different atomic concentration (%) of Cu and O from the thin film deposited. Sample deposited at 30 cycles confirms the atomic concentration (%) is similar to my experiments (i.e) (Cu(25.78%); O(74.22%). Likewise, K.P.Muthe et al., [118] showed that in reactive oxygen conditions, formation of Cu_2O phase is much faster when compared with CuO phase and this is clearly seen in our experimental conditions as well.

8.3 Inductively coupled plasma in E-mode

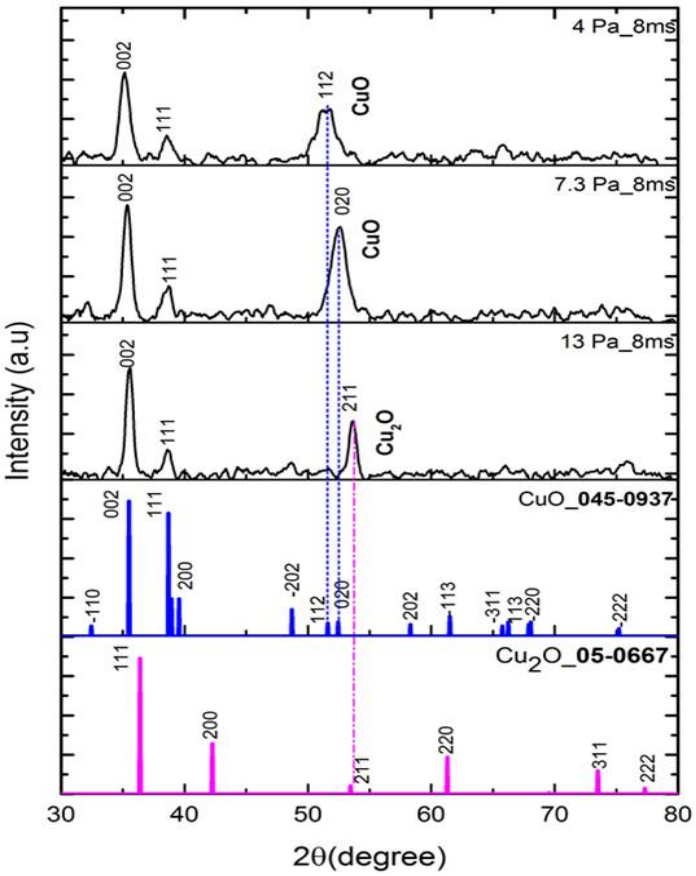

Figure 8.8: XRD pattern for Inductively coupled RF plasma (E-mode) at different pressures

Next, another set of experiments was carried out with the ICP at low power, in E-mode. As described in chapter 4, the plasma density as well as the density of reactive oxygen species is much lower in E-mode than it is in H-mode. Figure 8.8 shows that these films show a peak shift from $< 112 > \rightarrow < 020 >$ in CuO to $< 211 >$ in Cu_2O at 4Pa, 7.3Pa and 13Pa. However, the main peak in the spectrum is from $< 020 >$ in CuO for all pressures.

Again, at 7.3 Pa we see the high index (020) plane of CuO being deposited. The additional energy provided by the background ICP can explain why this phase can be grown in the PE-PLD case, but not in the standard PLD case (without substrate heating). Nevertheless, the quality of these films is not very good since they are not stoichiometric. EDX results

show that for all pressures the films are Cu-rich. This can be understood from the fact that an E-mode plasma has a lowe density of reactive oxygen species compared to the H-mode. In other words, it is the reactive oxygen that is active in the deposition process, simply having O_2 molecules (i.e. the same pressure) is not enough to incorporate enough O in the films; a high density of reactive oxygen, e.g. O and O_{2^*} is essential.

8.4 Thin film depositied at non-synchronised plasma condition

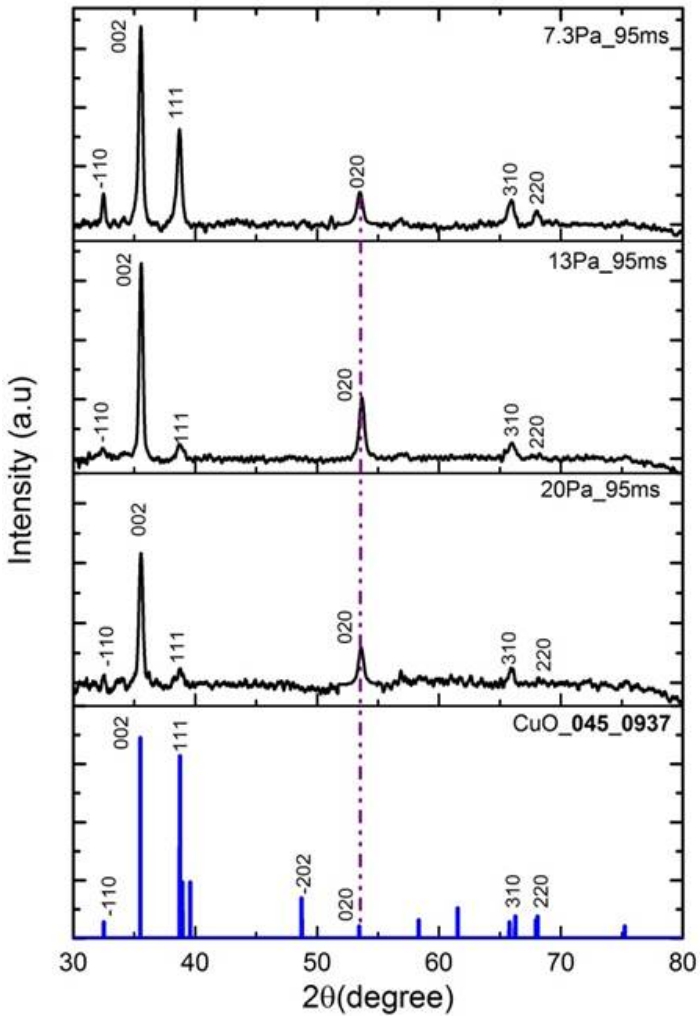

Figure 8.9: CuO thin film deposited at 7.3Pa, 13Pa and 20Pa with a de-synchronised PE-PLD set-up

In order to investigate the underpinning physics of the PE-PLD process, experiments were performed where the laser and ICP plasma were intentionally de-synchronised. These experiments will show whether in normal, synchronised PE-PLD there is an interaction between the Cu plume and the oxygen ICP, depositing CuO, or that there is a normal Cu deposition, which is subsequently oxidised by the ICP plasma. In these non-synchronised experiments,

only the latter process will happen. Details of the de-synchronisation timings can be found in figure 8.5.

The primary XRD peaks that can be observed for all pressures in Fig 8.9 are the $< 002 >$, $< 111 >$ and $< 020 >$ peaks of CuO, with the $< 002 >$ peak having the maximum intensity. These XRD patterns are very similar to what is found in the standard PLD case (fig 8.2) and distinctly different from the synchronised PE-PLD case (fig 8.6). This implies that there is very little (if any) oxidation of the already deposited films by the ICP plasma. The oxidation of the Cu happens when the Cu plume interacts with the ICP background plasma/gas. In the case of synchronised PE-PLD this is the background ICP, in the case of standard PLD and non-synchronised PE-PLD, this is neutral background gas.

8.5 Crystal size and surface morphology of the thin film

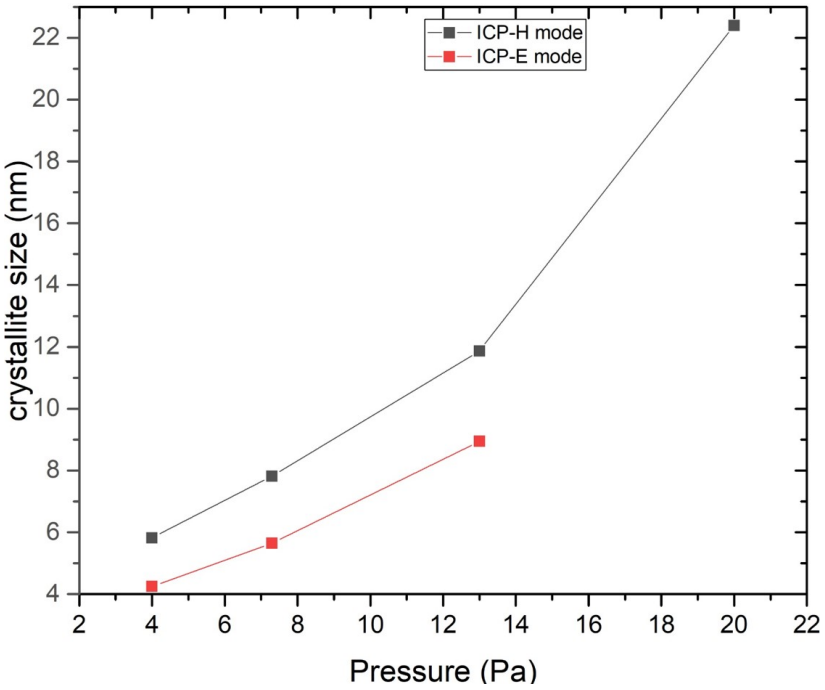

Figure 8.10: Crystal size calculation using Scherrer formula for Inductively coupled plasma at H-mode and E-mode

From the line broadening in the XRD experiments, the average crystal size can be calculated from the Scherrer equation.

$$\boxed{t = \frac{K\lambda}{\beta_t \ cos\theta_B}} \tag{8.1}$$

where, t is the average crystallite size, λ is the wavelength of X-rays, β_t is the FWHM of the most intense peak for corresponding θ, K is the Scherrer constant which varies between 1.0< K >0.89. Figure (8.10) shows the crystal sizes for the films deposited in the proof-of-concept PE-PLD experiments, i.e. H-mode ICP and synchronised laser and ICP. The crystal size increases with increasing pressure from 5.87 nm at 4 Pa to 22.4 nm at 25 Pa. As will be shown in the next section, the increase in crystal size also affects the electrical resistivity of the films, one of the main figures of merit of these types of films.

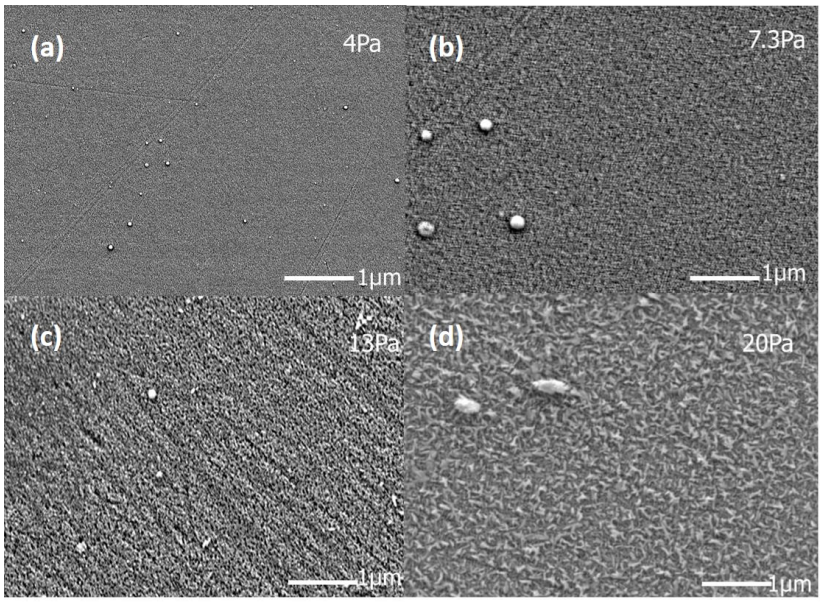

Figure 8.11: SEM image of PE-PLD thin film at different pressure (a) 4Pa (b) 7.3Pa (c) 13Pa (d) 20Pa. Increasing pressure increases the surface roughness

The calculated crystal sizes for the films deposited in E-mode at 4, 7.3 and 13 Pas are 4.25, 5.65 and 8.94 nm respectively. This is less than the crystal sizes obtained with the H-mode experiments. Whereas, the crystal sizes calculated from films in the gas background at 13Pa and 20Pa are 15nm and 20nm which is bigger than crystal sizes calculated from

both E-mode and H-mode.

The surface morphology of the films is studied using a SEM (JEOL JSM7800F FE). Figure (8.11) shows the SEM images for the H-mode PE-PLD films at different pressures. It clearly shows that an increase in pressure decreases the surface smoothness. A possible reason for the increased roughness could be the increased exposure to bombarding ions from the ICP (with increasing pressure). To test this hypothesis, a film deposited with standard PLD from a CuO target at 7.3Pa was subjected to a post-treatment with an ICP plasma at varying powers from 200W to 800W, i.e. varying levels of ion bombardment. The results of these experiments are shown in figure 8.12.

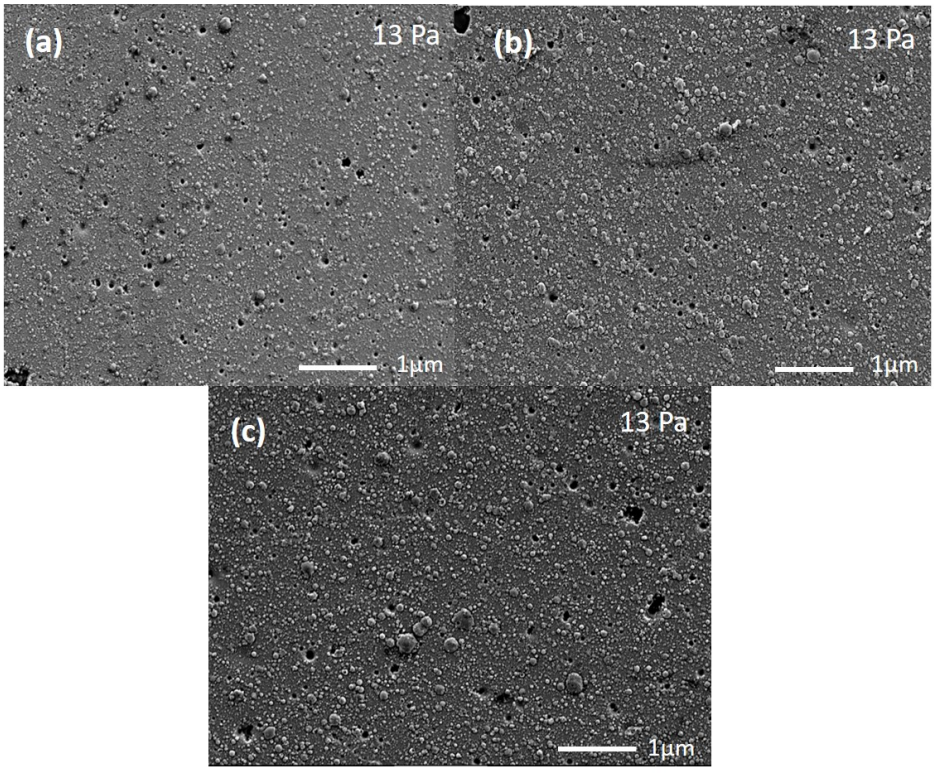

Figure 8.12: Thin film deposited using CuO target at 13Pa and post treatment of film at (a) 200W, (b) 500W and (c) 800W

The results in fig (8.12) show only a minor increase in the surface roughness of the films with increasing ICP post-treatment power, i.e. increasing ion bombardment. Regardless, all

the post-treated films have a very different morphology than the standard PE-PLD films (fig (8.4)). This leads to the conclusion that the increased roughness observed in the PE-PLD films is not due to the ion bombardment from the ICP.

8.6 Deposition rate and electrical resistivity measurement

As well as the quality of the deposited thin film, another important parameter for practical applications is the deposition rate of the film. In order to calculate the deposition rate, thin films were deposited for 90min and then analysed with an AFM (Bruker). For these experiments, part of the deposited film was removed using ethanol and the step between the film and the cleaned surface was measured. Running the AFM in tapping mode, the cantilever is scanned along the sample surface and the depth difference between the deposited film and the cleaned surface gives the thickness of the film. Film thicknesses were calculated for both the standard H-mode ICP and the low-power E-mode for different pressures. The results are shown in figure (8.13). It shows deposition rates ranging from 1.3 nm/min to 3.3 nm/min. Overall, these deposition rate are in line with what has been observed typically for standard PLD [119]. Interestingly, figure (8.13) also shows that the deposition rate of E-mode is always greater than H-mode.

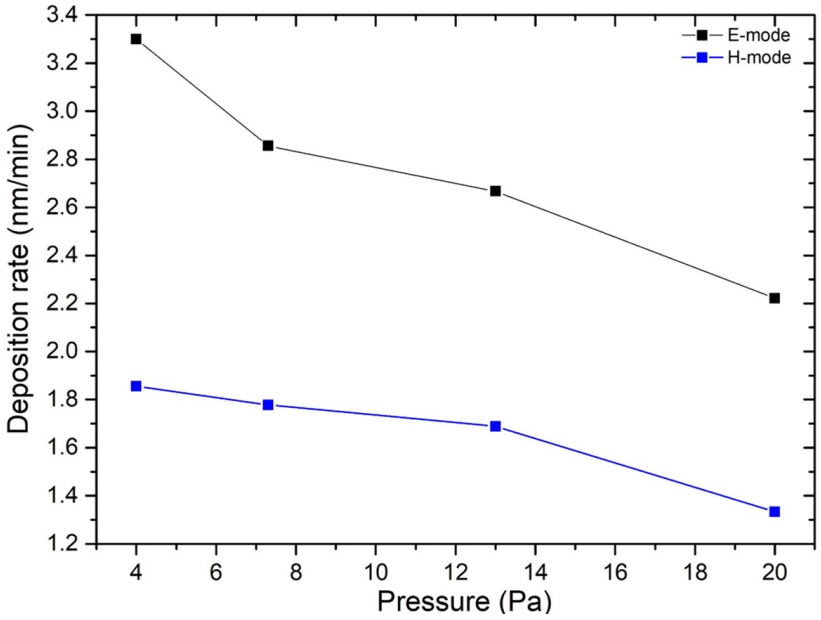

Figure 8.13: Thin film deposition rate at E-mode and H-mode

A possible explanation for this is that in H-mode the density of both ions and reactive neutral species is much higher than in E-mode, increasing the interactions between the plume and the background, slowing down the expanding plume and reducing the amount of material that will reach the substrate. This explanation is further strengthened by the observation that the deposition rate goes down with increasing pressure for both E-mode and H-mode. In other words, increasing pressure leads to higher plasma densities, increased interaction with the plume and a reduction in material deposited. Of course, it should be noted that despite a higher deposition rate in E-mode, the quality of these films, i.e. stoichiometry and crystal structure, is not very good, limiting the practical applications for E-mode deposited films.

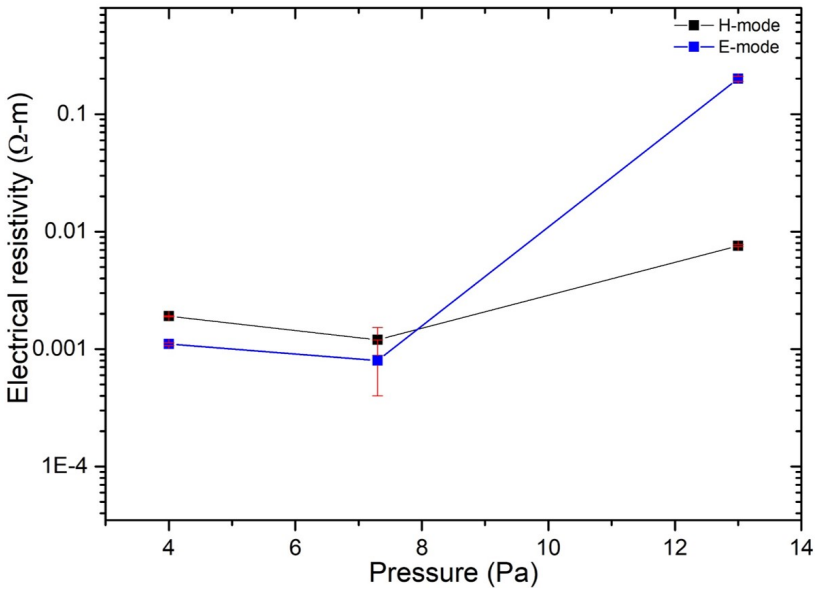

Figure 8.14: Electrical resistivity of thin film calculated using four point probe at H-mode and E-mode

Finally, the electrical properties of the films were studied using a four point probe technique Jandel RM3 AR instrument. Together with the film thickness (from AFM measurements), the electrical resistivity of the films can be calculated as follows:

$$\boxed{\textit{Electrical resistivity } (Q) = R_s \times d} \tag{8.2}$$

Where R_s is the sheet resistance and d is the thickness of the film.

Fig (8.14) shows the electrical resistivity of films deposited at E-mode and H-mode. At 4Pa and 7.3Pa, for both E-mode and H-mode the resistivity of the film are nearly the same and at 13Pa there is a sudden variation in the electrical resistivity of the film for E-mode and H-mode. The resistivity of the film at H-mode is 7.6 x 10^{-3} Ω-m whereas, at E-mode it is 0.2 Ω-m. Electrical resistivity calculated calculated for 20Pa plasma background (E-mode, H-mode), plasma non-synchronised, gas environment for Cu and CuO target are highly resistive and it is out of range.

In conclusion, the PE-PLD proof-of-concept experiments have shown the potential of the PE-PLD technique to produce high-quality, i.e. stoichiometric and polycrystalline films from a Cu target without substrate heating or post-annealing. The deposition rates are comparable to standard PLD and the measured electrical resistivity is also good compared to PLD films. Interestingly, it is possible to tune the composition of the film from CuO to Cu_2O (both stoichiometric) using just the pressure in the ICP. The additional experiments have shown that there is indeed a clear interaction between the expanding Cu plume and the background ICP plasma. I.e. oxidation of the Cu happens in the travelling plume, not after the Cu is deposited. Furthermore, it is shown that the density of reactive oxygen in the ICP is critical for achieving a high quality film, i.e. a high-density H-mode is needed.

Chapter 9

Conclusion

The main focus of this thesis is an introduction and feasibility study of a novel thin film deposition technique: Plasma-Enhanced Pulsed Laser Deposition. The main idea is to incorporate an inductively coupled oxygen RF plasma in a standard PLD set-up for the deposition of metal-oxide thin films. Advantages of this novel technique include the use of simple pure metal targets instead of metal-oxide composite targets and the lack of the necessity for substrate heating and post-annealing to obtain high-quality films.

First, the feasibility of the PE-PLD technique is investigated using numerical simulations (chapter 5). Two different numerical models were used for understanding the laser ablation process and the inductively coupled oxygen plasma, respectively. Modelling of laser ablation of copper at 13Pa and 20Pa were used to estimate the electron temperature and the axial velocity of the expanding copper plume. At 13Pa, the peak velocity of the Cu plume is around 1.5×10^6 m/s for all times between 20 and 100ns. Further, increasing the background pressure to 20Pa leads to the decrease in the peak velocity to around 1.4×10^6 m/s. In both cases, the highest peak velocities are found near the front of the expanding plume.

On the other hand, the estimated electron temperature for 13Pa slowly decreases from 1.41eV to 1.29eV between 20ns to 100ns and at 20Pa, the temperature decreases from 1.49eV

to 1.3eV. This change in electron temperature and axial velocity shows that the small variation in the background pressure has an influence on the plume properties and plume dynamics, meaning that background pressure cannot be used as in independent control parameter for stoichiometry. The electron densities found in the laser ablation of Cu for 13Pa and 20Pa were around 9×10^{17} cm^{-3} near the front of the expanding plume and the densities on the order of 2-6 $\times$ 10^{17} cm^{-3} are found behind the front. Based on the modelling results, the density of Cu at the substrate surface (4 cm from target) can be estimated to be in the order of 10^{14} cm^{-3}.

Second, different numerical simulations of (only) the inductively coupled oxygen plasma showed that electrons and O_2^+ ions were the main charged species at densities around 10^{11} cm^{-3}. However, reactive neutral species, in particular O and O_2^*, were found to have densities 2-5 orders of magnitude higher than the charged species. It is known from the PLD studies that the neutral reactive species O and O_2^* plays a major role in interacting with the expanding plume during thin film growth. Therefore, it is likely that the interaction of the Cu plume with the background plasma will involve reactive neutral species and not ionic species. Also, the densities of these reactive species are on the order of 10^{14} cm^{-3}, i.e. similar as the Cu plume in front of the substrate, obtaining conditions that allow a effective interactions between the two plasmas. Moreover, the modelling shows that the ratio of the two reactive oxygen species can be controlled with the pressure, enabling a further, independent control over the oxidation process in PE-PLD.

The first experimental results, presented in chapter 6, involve the use of time-resolved optical emission spectroscopy to measure the electron temperature and electron densities. A laser produced Cu plasma in vacuum, background oxygen gas and oxygen ICP plasma. It was found that plasma emission from the Cu plume expands faster in the vacuum compared to the background gas environment, because the gas initiates shock waves, slowing down the expansion. Overall, there was a good agreement between the POLLUX simulations and these experimental results. I.e. temperatures calculated from the experiments for 13Pa for

the first 100ns are 1.51eV-1.20eV and 1.53eV-1.25eV for 20Pa. Whereas, from POLLUX simulation, the temperature varies between 1.41eV-1.2eV for 13Pa and 1.49eV-1.38eV for 20Pa. In addition, line broadening studies were done to calculate the electron densities from the measured Stark broadening. Densities in the order of 10^{18} cm^{-3} were measured for times 30-50 ns, which subsequently decrease rapidly to $\sim 10^{15}$ - 10^{16} cm^{-3} for times greater than 100 ns. The same general trend was found for all scenarios, i.e. vacuum, gas or ICP plasma background. Furthermore, since both the temperature and density diagnostic relies on an assumption of LTE for the plasma under study, some effort was made to verify the accuracy of this assumption. In particular, the McWhirter criterion (equation (7.5)) was used to determine whether the measured electron density was indeed high enough to assume LTE. It was found that the plasma was not in full LTE for most of the ablation process, i.e. $>\sim 70$ ns. However, the more relaxed concept of pLTE was met for almost all of the measurements. This highlights an important point about the LTE assumption in that even though pLTE is observed (e.g. via a Boltzmann plot), this does not necessarily mean the plasma is in full LTE which means that further investigations are needed to verify the accuracy of these widely used techniques in these types of experiments.

Finally, in chapter 8, the full PE-PLD proof-of-concept experiments were presented. The thin films we deposited in 4Pa, 7.3Pa, 13Pa and 20Pa H-mode ICP backgrounds. Within this narrow pressure range we can observe a transition between CuO and Cu_2O films, both in stoichiometry and crystal structure. In addition, the CuO films have a highly active (020) structure compared to the normal (002) structure. These experiments show that high-quality copper oxide films can be grown from pure copper targets with the PE-PLD technique without the need for substrate heating or post-annealing. The exact composition can be tuned with the pressure of the ICP.

In order to gain a better understanding of the underlying processes of the PE-PLD deposition, experiments were performed with the ICP in a low-power E-mode and experiments where the laser and ICP were de-synchronised. These experiments show that there is a

definite interaction between the Cu plume and the oxygen ICP, i.e. Cu deposition with subsequent oxygen plasma exposure does not give good films. Also, high densities are needed in the ICP; the low-power E-mode characterised by lower plasma densities and higher ion bombardment energies, again results in poor quality, non-stoichiometric films.

In conclusion, this work has introduced the novel PE-PLD technique and shown its potential in a proof-of-concept study on copper oxide. I found that using this technique I can deposit high-quality copper oxide films from a pure Cu target and without substrate heating or post-annealing. In addition, the ICP can be used to tune the composition and crystal structure of the films, going from stoichiometric CuO to stoichiometric Cu_2O.

List of References

[1] S. Rajendiran, A. K. Rossall, A. Gibson, and E. Wagenaars. Modelling of laser ablation and reactive oxygen plasmas for pulsed laser deposition of zinc oxide. *Surf. Coatings Technol.*, 260:417, 2014.

[2] B. P. Rai. Cu2O Solar Cells: A review. *Sol. Ceils*, 25:8, 1988.

[3] S. M. Pawar, J. Kim, A. I. Inamdar, H. Woo, Y. Jo, B. S. Pawar, S. Cho, H. Kim, and H. Im. Multi-functional reactively-sputtered copper oxide electrodes for supercapacitor and electro-catalyst in direct methanol fuel cell applications. *Sci. Rep.*, 6(October 2015):21310, 2016.

[4] Z. Kang, et al. Electronic structure engineering of Cu2O film/ZnO nanorods array all-oxide p-n heterostructure for enhanced photoelectrochemical property and self-powered biosensing application. *Sci. Rep.*, 5:7882, 2015.

[5] G. J.Greek and O.Meyer. Epitaxial Growth and Properties of YBaCuO thin films. *Mater. Sci. reports*, 4(June):193, 1989.

[6] J. P. Locquet. In-situ MBE growth of epitaxial CuO films with a source of activated oxygen. *J. Less-Common Met.*, 164-165(PART 1):300, 1990.

[7] V. F. Drobny and L. Pulfrey. Properties of reactively-sputtered copper oxide thin films. *Thin Solid Films*, 61(1):89, 1979.

[8] S. B. Ogale, P. G. Bilurkar, N. Mate, S. M. Kanetkar, N. Parikh, and B. Patnaik. Deposition of copper oxide thin films on different substrates by pulsed excimer laser ablation. *J. Appl. Phys.*, 72(8):3765, 1992.

[9] R. Leuchtner and L. Hristakos. A study of copper oxide films fabricated by pulsed laser deposition. *Mater. Res. Soc. Symp. Proc.*, 401:551, 1996.

[10] M. F. Al Kuhaili. Characterization of copper oxide thin films deposited by the thermal evaporation of cuprous oxide (cu2o). *Vacuum*, 82:623–629, 2008.

[11] N. Nafarizal. Precise control of metal oxide thin films deposition in magnetron sputtering plasmas for high performance sensing devices fabrication. *procedia chemistry*, 20:93, 2016.

[12] M. Thirumoorthia and J. Thomas Joseph Prakash. Structure, optical and electrical properties of indium tin oxide ultra thin films prepared by jet nebulizer spray pyrolysis technique. *Journal of Asian Ceramic Societies*, 4:124, 2016.

[13] D. Dijkkamp, T. Venkatesan, X. Wu, S. Shaheen, N. Jisrawi, Y. Min-Lee, W. McLean, and M. Croft. Preparation of y-ba-cu oxide superconductor thin films using pulsed laser evaporation from high-7;. bulk material. *Appl. Phys. Lett*, 51, 1987.

[14] P. Morgan, D. Partin, B. Chamberland, and M. O'Keeffe. Synthesis of paramelaconite: Cu4o3. *Journal of solid state chemistry*, 121:33, 1996.

[15] J. A.Thobor. Properties and air annealing of paramelaconite thin films. *Materials Letters*, 57:3676, 2003.

[16] K. Amikura, T. Kimura, M. Hamada, N. Yokoyama, JunMiyazaki, and Y. Yamada. Copper oxide particles produced by laser ablation in water. *Applied Surface Science*, 254:6976, 2008.

[17] J. Piersona, A. Thobor-Kecka, and A. Billardb. Cuprite, paramelaconite and tenorite films deposited by reactive magnetron sputtering. *Applied Surface Science*, 210:359, 2003.

[18] B. K. Meyer, et al. Binary copper oxide semiconductors: From materials towards devices. *Phys. Status Solidi B*, 249:1487, 2012.

[19] B. Balamurugan and B. Mehta. Optical and structural properties of nanocrystalline copper oxide thin films prepared by activated reactive evaporation. *Thin Solid Films*, 396(1-2):90, 2001.

[20] P. A. Korzhavyi and B. Johansson. Literature review on the properties of cuprous oxide cu2o and the process of copper oxidation. Technical Report TR-11-08, 2011.

[21] Terence, K. S. Wong, S. Zhuk, S. Masudy-Panah, and G. K. Dalapati. Current status and future prospects of copper oxide heterojunction solar cells. *Materials review*, 9, 2016.

[22] H.A.Al-Jawhari. A review of recent advances in transparent p-type cu2o-based thin film transistors. *Materials Science in Semiconductor Processing*, 40:241, 2015.

[23] S. R. Jian, G. J. Chen, and W. M. Hsu. Mechanical properties of Cu2O thin films by nanoindentation. *Materials (Basel).*, 6(10):4505, 2013.

[24] Y.-F. Lim, C. S. Chua, C. J. J. Lee, and D. Chi. Sol–gel deposited cu2o and cuo thin films for photocatalytic water splitting. *Phys. Chem. Chem. Phys*, 16:25928, 2014.

[25] A. Ogwu. Electrical resistivity of copper oxide thin films prepared by reactive magnetron sputtering. *Manuf. Eng.*, 24(1):172, 2007.

[26] L. D. L. S. Valladares, D. H. Salinas, A. B. Dominguez, D. A. Najarro, S. Khondaker, T. Mitrelias, C. Barnes, J. A. Aguiar, and Y. Majima. Crystallization and electrical resistivity of cu2o and CuO obtained by thermal oxidation of cu thin films on SiO2/si substrates. *Thin Solid Films*, 520(20):6368, 2012.

[27] M. F. Jawad, R. A. Ismail, and K. Z. Yahea. Preparation of nanocrystalline cu2o thin film by pulsed laser deposition. *J Mater Sci: Mater Electron*, 22:1244, 2011.

[28] J. B. Forsyth and S. Hull. The effect of hydrostatic pressure on the ambient temperature structure of cuo. *J. Phys.: Condens. Matter*, 3:5257, 1991.

[29] Y. Yil-hwan, Bae, Seung-muk, Y.-h. Kim, and J. Hwang. Deposition Optimization and Property Characterization of Copper-Oxide Thin Films Prepared by Reactive Sputtering. *J. Microelectron. Packag. Soc.*, 20(1):27, 2013.

[30] M. Awad and N. Hadia. Copper oxide nanocrystallites fabricated by thermal oxidation of pre-sputtered copper films at different temperatures and under oxygen and argon flows. *Optik - International Journal for Light and Electron Optics*, 142:334, 2017.

[31] A. Umaa, A. Alshahrani, H. Algarni, and R. Kumar. Cuo nanosheets as potential scaffolds for gas sensing applications. *Sensors and Actuators B: Chemical*, 250:24, 2017.

[32] S. B. krishnamoorthy, editor. *Thin Film Structures in Energy Applications*. Springer-Verlag GmbH, 2015.

[33] Y.H.Navalea., S.T.Navaleb, F.J.Stadlerb, N.S.Ramgirc, A.K.Debnathc, S.C.Gadkaric, S.K.Guptac, D.K.Aswald, and V.B.Patil. Thermally evaporated copper oxide films: A view of annealing effect on physical and gas sensing properties. *Ceramics International*, 43:7057, 2017.

[34] Z. Ren, N. Meng, K. Shehzad, Y. Xu, S. Qu, B. Yu, and J. K. Luo. Mechanical properties of nickel-graphene composites synthesized by electrochemical deposition. *Nanotechnology*, 26:065706, 2015.

[35] R. Pandiyan, Z. O. Elhmaidi, Z. Sekkat, M. Abd-lefdil, and M. A. E. Khakani. Reconstructing the energy band electronic structure of pulsed laser deposited CZTS thin

films intended for solar cell absorber applications. *Applied Surface Science*, 396:1562, 2017.

[36] Y. Liang, Y. Yao, X. Zhang, W.-L. Hsu, Y. Gong, J. Shin, E. D. Wachsman, M. Dagenais, and I. Takeuchi. Fabrication of organic-inorganic perovskite thin films for planar solar cells via pulsed laser deposition. *AIP Advances*, 6:015001, 2016.

[37] J. Chenga, G. Caoa, H. Zonga, C. Kanga, E. Jiaa, B. Zhangb, and M. Lia. Highly transparent conductive azo/zr50cu50/azo films in wide range of visible and near infrared wavelength grown by pulsed laser deposition. *Results in Physics*, 7:910, 2017.

[38] P. Peyre and R. Fabbro. Laser shock processing: a review of the physics and applications. *Optical and Quantum Electronics*, 27:1213, 1995.

[39] K. Song, Y.-I. Lee, and J. Sneddon. Recent developments in instrumentation for laser induced breakdown spectroscopy. *Applied Spectroscopy Reviews*, 37(1):89, 2002.

[40] M. Hanif, M. Salik, and M. A. Baig. Laser based optical emission studies of zinc oxide (zno) plasma. *Plasma Chemistry and Plasma Processing*, 33:1167, 2013.

[41] E. Tognoni, V. Palleschi, M. Corsi, and G. Cristoforetti. Quantitative micro-analysis by laser-induced breakdown spectroscopy: a review of the experimental approaches. *Spectrochimica Acta Part B: Atomic Spectroscopy*, 57(7):1115, 2002.

[42] A. W. Miziolek, V. Pallesch, and I. Schechter, editors. *Laser-induced breakdown spectroscopy (libs)*. Cambridge university press, 2006.

[43] K. Sugioka, M. Meunier, and A. Piqué, editors. *Laser Precision Microfabrication*. Springer Berlin Heidelberg, 2010.

[44] Harilal. *optical emission diagnostics of laser produced plasma from graphite and YBa2Cu2O7*. Ph.D. thesis, International school of photonics, cochin, 1997.

[45] J. reece roth. *Industrial plasma engineering*, volume 1. IOP publishing Ltd, 1995.

[46] J. P. singh and S. N. thakur, editors. *Laser-Induced Breakdown spectroscopy*. Elsevier, 2007.

[47] X. Zeng, X. Mao, R. Greif, and R. Russo. Experimental investigation of ablation efficiency and plasma expansion during femtosecond and nanosecond laser ablation of silicon. *Applied Physics A*, 80(2):237, 2005.

[48] A. V. Arefiev and B. N. Breizman. Experimental studies on ion acceleration and stream line detachment in a diverging magnetic field. *Phys. Plasmas*, 17(7):072106, 2010.

[49] D. Bennaceur-Doumaz, D. Bara, E. Benkhelifa, and M. Djebli. Effects of nonthermal electrons on plasma expansion into vacuum. *Journal of Applied Physics*, 117(4):043303, 2015.

[50] S. Schaaf, Peter. *Laser Processing of Materials: Fundamentals, Applications and Developments*. 2010.

[51] D. B.Chris and G. K. Huber. *Pulsed Laser Deposition of Thin Films*. Wiley-Interscience, 1994.

[52] H. Heo, J. H. Sung, J.-H. Ahn, F. Ghahari, T. Taniguchi, K. Watanabe, P. Kim, and M.-H. Jo. Frank-van der merwe growth versus volmer-weber growth in successive stacking of a few-layer bi2 te3 /sb2 te3 by van der waals heteroepitaxy: The critical roles of finite lattice-mismatch with seed substrates. *Advanced Electronic Materials*, 3(2):1600375, 2017.

[53] M. A. Fusella, F. Schreiber, K. Abbasi, J. J. Kim, A. L. Briseno, and B. P. Rand. Homoepitaxy of crystalline rubrene thin films. *Nano Letters*, 17(5):3040, 2017.

[54] Y. N. Mitsuhisa KAWAKAMI, Agung Budi HARTANTO and T. OKADA. Synthesis of zno nanorods by nanoparticle assisted pulsed-laser deposition. *Jpn. J. Appl. Phys*, 42(Part 2, No.1A/B):L 33–L 35, 2003.

[55] A. O. Dikovska, M. E. Koleva, G. B. Atanasova, T. R. Stoyanchov, N. N. Nedyalkov, and P. A. Atanasov. PLD fabrication of ZnO nanostructures on metal-coated substrates. *Journal of Physics: Conference Series*, 514:012032, 2014.

[56] C. G. Subhash Chandra Singh, Haibo Zeng and W. Cai, editors. *Nanomaterials: Processing and Characterization with Lasers*. Wiley VCH Verlag GmbH, 2012.

[57] V. J. Rico, R. Lahoz, F. Rey-García, F. Yubero, J. P. Espinós, G. F. de la Fuente, and A. R. González-Elipe. Laser treatment of nanoparticulated metal thin films for ceramic tile decoration. *ACS Applied Materials & Interfaces*, 8(37):24880, 2016.

[58] J. Perrière, E. Millon, W. Seiler, C. Boulmer-Leborgne, V. Craciun, O. Albert, J. C. Loulergue, and J. Etchepare. Comparison between ZnO films grown by femtosecond and nanosecond laser ablation. *Journal of Applied Physics*, 91(2):690, 2002.

[59] H. M. Smith and A. F. Turner. Vacuum deposited thin films using a ruby laser. *Applied optics*, 4, 1965.

[60] K. Takamura, T. Fujiwara, A. Yokota, M. Nakamura, and K. Yoshimoto. Growth and annealing effect of srtio3 thin films grown by pulsed laser deposition using fourth harmonic nd:yag pulsed laser. *physica status solidi (c)*, 14, 2017.

[61] D. Chrisey, J. Horwitz, J. Pond, R. Auyeung, P. Dorsey, S. Qadri, L. Knauss, C. Mueller, and R. Yandrofsk. "active microwave device applications of ferroelectric thin films. *SPIE*, 2403, 1996.

[62] Z. Li, C.-K. Dong, J. Yang, S.-Z. Qiao, and X.-W. Du. Laser synthesis of clean mesocrystal of cupric oxide for efficient gas sensing. *Journal of Materials Chemistry A*, 4, 2016.

[63] Craciun, V. S. Amirhaghi, D. Craciun, J. Eldars, J. Gardeniers, and I. Boyd. Effects of laser wavelength and fluence on the growth of zn0 thin films by pulsed laser deposition. *Appl. Surf. Sc*, 86:122, 1995.

[64] J. C.Miller and R. F. Haglund, editors. *Laser ablation and desorption*, volume 30 of *Experimental Methods in the Physical Sciences*. Academic press, 1998.

[65] P. A. Miller and G. A. Hebner. An inductively coupled plasma source for the gaseous electronics conference rf reference cell. *Journal of Research of the National Institute of Standards and Technology*, 100:427, 1995.

[66] E. C. Lin. Radiation risk from medical imaging. *Mayo Clinic Proceedings*, 85(12):1142, 2010.

[67] M. Beye, S. Schreck, F. Sorgenfrei, C. Trabant, N. Pontius, C. Schüßler-Langeheine, W. Wurth, and A. Föhlisch. Stimulated x-ray emission for materials science. *Nature*, 501(7466):191, 2013.

[68] B. D. Cullity. *Elements of X-ray diffraction*. ADDISON-WESLEY PUBLISHING COMPANY INC, 2nd edition, 1978.

[69] L. Reimer. *Scanning Electron Microscopy*. Springer, 2010.

[70] F. Wenner. A method of measuring earth resistivity. *Bulletin of the Bureau of Standards*, 12:469, 1915.

[71] D. K. SCHRODER. *Semiconductor material and device characterization*. John Wiley & Sons, Inc., Hoboken, New Jersey, 2006.

[72] L. Valdes. Resistivity measurements on germanium for transistors. *Proceedings of IRE*, 42:420, 1954.

[73] J. Albers. An alternative approach to the calculation of four-probe resistances on nonuniform structures. *Journal of The Electrochemical Society*, 132(10):2453, 1985.

[74] M. Hooper, editor. *Laser-Plasma interactions 4*. Scottish universities summer school in physics, 1988.

[75] M. Kushner. Hybrid modelling of low temperature plasmas for fundamental investigations and equipment design. *Journal of Physics D: Applied Physics*, 42(19):194013, 2009.

[76] M. Qaisar and G. Pert. Laser ablation of mg, cu and pb using infrared and ultraviolet low-fluence lasers. *Journal of applied physics*, 94:1468, 2003.

[77] J. P. Boris and D. L. Book. Flux-corrected transport. i. shasta, a fluid transport algorithm that works. *Journal of Computational Physics*, 11, 1973.

[78] S. Thomson and H. Lauson. Improvements in the chart d: Radiation-hydrodynamic code i analytic equation of states. techreport SC-RR-710714, Sandia Labs Report, 1972.

[79] G. J. Pert. Approximations for the rapid evaluation of the thomas-fermi equation. *Journal of physics B*, 32:249, 1999.

[80] S. Tinck and A. Bogaerts. computer simulations of an oxygen inductively coupled plasma used for plasma - assisted atomic layer deposition. *plasma sourcecs Sci. Tech*, 20:015008, 2011.

[81] A. R. Gibson, M. Foucher, D. Marinov, P. Chabert, T. Gans, M. J. Kushner, and J.-P. Booth. The role of thermal energy accommodation and atomic recombination probabilities in low pressure oxygen plasmas. *Plasma physics and controlled fusion*, 59(024004), 2017.

[82] S. A. Lawton and A. V. Phelps. Excitation of the ($b^1\ \Sigma_g^+$) state of o_2 by low energy electrons. *Journal of chemical physics*, 69:1055, 1978.

[83] Phelps and database. www.lxcat.net. Technical report, 2010.

[84] M. K. Tashiro M and T. J. R-matrix calculation of electron collisions with electronically excited o2 molecules. *Physical review A*, 73:052707, 2006.

[85] Y. Itikawa and A. Ichimura. Cross sections for collisions of electrons and photons with atomic oxygen. *Journal of physical chemistry Reference data*, 19:637, 1990.

[86] R. I. Hall and S. Trajmar. Scattering of 4.5 ev electrons by ground state and metastable oxygen molecules. *Journal of physics B: Atomic and molecular physics*, 8:L293, 1975.

[87] P. D. Burrow. Dissociative attachment from the o2 state. *Journal chemical physics*, 59:4922, 1973.

[88] R. R. Laher and F. R. Gilmore. Updated excitation and ionization cross sections for electron impact on atomic oxygen. *Journal of physical chemistry reference data*, 19:277, 1990.

[89] H. Deutsch, P. Scheier, K. Becker, and T. D. Mark. Calculated cross-sections for electron-impact detachment from negative ions using the deutsch-mark formalism. *Chemical physical letters*, 382:26, 2003.

[90] S. Peverall. Dissociative recombination and excitation of o2+: cross sections, product yields and implications for studies of ionospheric airglows. *Journal chemical physics letters*, 114:6679, 2001.

[91] A. I. Florescu-Mitchell and J. B. A. Mitchell. Dissociative recomination. *Physics reports*, 430:277, 2006.

[92] J. T. Gudmundsson, A. M. Marakhtanov, K.K.Patel, V. P. Gopinath, and M. A. Lieberman. A reply to a comment on: 'on the plasma parameters of a planar inductive oxygen discharge. *J. Phys. D: Appl. Phys*, 33:3010, 2000.

[93] S. G. Ard, J. J. Melko, B. Jiang, Y. Li, N. S. Shuman, H. Guo, and A. A. Viggiano. Temperature dependences for the reactions of o2- and o- with n and o atoms in a selected-ion flow tube instrument. *Journal of chemical physics*, 139:144302, 2013.

[94] A. Midey, I. Dotan, S. Lee, W. T. Rawlins, M. A. Johnson, and A. Viggiano. Kinetics for the reactions of o- and o2- with o2 measured in a selected ion flow tube at 30. *journal of physical chemistry A*, 111:5218, 2007.

[95] N. L. Aleksandrov. *soviet physics*, 23:806, 1978.

[96] M. Ziolkowski, G. C. Schatz, A. A. Viggiano, A. Midey, and I. Dotan. O2 charge exchange with simple ions. *journal of chemical physics*, 140:214307, 2014.

[97] I. Dotan. Rate constants and branching ratios for the reations of o ions at relative kinetic energies 0.04-2 ev. *chemical physics letters*, 75:509, 1980.

[98] R. Atkinson, D. L. Baulch, R. A. Cox, J. N. Crowley, and J. Troe. Evaluated kinetic and photochemical data for atomospheric chemistry: Volume i gas phase reaction. *Atmoshperic chemical physics*, 4:1461, 2004.

[99] G. E. Streit, C. J. Howard, A. L. Schmeltekopf, J. A. Davidson, and H. I. Schriff. Temperature dependence of o(1d) rate constants for reactions with o2, n2, co2, o3 and h2o. *Journal of chemical physics*, 65:4761, 1976.

[100] L. C. Lee and T. G. Slanger. Observations on o(1d-3p) and o2 following o2 photodissociation. *Journal chemical physics*, 69:4053, 1978.

[101] I. D. Clark and R. P. Wayne. The reaction of o2 with atomic nitrogen and with atomic oxygen. *chemical physics letters*, 3:405, 1969.

[102] J. B. Burkholder, S. P. Sander, J. P. D. Abbat, J. R. Barker, R. E. Huie, C. E. Kolb, M. J. Kurylo, V. L. Orkin, D. M. Wilmouth, and P. H. Wine. Chemical kinetics and photochemical data for use in atmospheric studies, evaluation no.18. *JPL publication*, 15-10, 2015.

[103] R. F. I. Heidner, C. E. Gardner, T. M. El-Sayed, G. I. Segal, and K. J. VV. Temperature dependance of o2 and energy pooling. *Journal chemical physics*, 74:5618, 1981.

[104] A. Hussain, X. Gao, Q. LI, Z. Hao, and J. Lin. combined effects of ambient gas pressures and magnetic field on laser plasma expansion dynamics. *Plasma science and technology*, 19:015505, 2017.

[105] S. Blackwell, R. Smith, S. Kenny, J. Walls, and C. Sanz-Navarro. Modelling the growth of zno thin films by pvd methods and the effects of post-annealing. *J. Phys. Condens. Matter*, 25(135002), 2013.

[106] S. Nguyen-Kuok. *Theory of Low-Temperature Plasma Physics*. Springer-Verlag GmbH, 2016.

[107] M. I. Boulos, P. Fauchais, and E. Pfender. *Thermal Plasmas*. Springer, 2013.

[108] I.H.Hutchinson. *Principles of plasma diagnostics Second edition*. cambridge university press, 2002.

[109] M. Whirter and A. Hearn. A calculation of the instantaneous population densities of the excited levels of hydrogenlike ions in a plasma. *Proceedings of the Physical Society*, 82:641, 1963.

[110] R. H. Huddlestone and S. L.Leonard, editors. *Plasma diagnostic techniques*, volume 21. Academic press new york london, 1965.

[111] H. K. Chung, R. W. Lee, M. H. Chen, and Y. Ralchenko. *FLYCHK @NIST*, 2008.

[112] V. K. Unnikrishnan, K. alti, V. B. Kartha, C. Santhosh, G. P. Gupta, and B. M. Suri. Measurements of plasma temperature and electron density in laser-induced copper plasma by time-resolved spectroscopy of neutral atom and ion emissions. *Pramana-journal of physics*, 74(6):983, 2010.

[113] H. R. Griem. *Principles of Plasma Spectroscopy*. Cambridge univ press, 2004.

[114] N. M. Shaikh, B. Rashid, S. Hafeez, Y. Jamil, and M. A. Baig. Measurement of electron density and temperature of a laser-induced zinc plasma. *Journal of physics d: applied physics*, 39:1384, 2006.

[115] M. G. Arup Kumar Kunti, Shailendra Kumar Sharma. A comparative study on structural growth of copper oxide deposited by dc-ms and hipims. *ECS Journal of Solid State Science and Technology*, 5:P627, 2016.

[116] Z. H. Gan, G. Q. Yu, B. K. Tay, C. M. Tan, Z. W. Zhao, and Y. Q. Fu. Preparation and characterization of copper oxide thin films deposited by filtered cathodic vacuum arc. *Journal of physics d: applied physics*, 37:81, 2004.

[117] O. Daoudi, Y. Qachaou, A. Raidou, K. Nouneh, M. Lharch, and MounirFahoume. Study of the physical properties of cuo thin films grown by modified silar method for solar cells applications. *Superlattices and Microstructures*, 1-7, 2018.

[118] K. Muthe, J. Vyas, S. N. Narang, D. Aswal, S. Gupta, D. Bhattacharya, R. Pinto, G. Kothiyal, and S. Sabharwal. A study of the cuo phase formation during thin film deposition by molecular beam epitaxy. *Thin Solid Films*, 324:37, 1998.

[119] M. Strikovski, J. H.Miller, and J. Wosik. Deposition rate as the key parameter in pulsed laser deposition of oxide films: a practical model and experiment. *Physica C: Superconductivity*, 341-348:2349, 2000.